



UNIVERSITÀ
DI PAVIA



UNIVERSITY OF PAVIA
FACULTY OF ENGINEERING

UNIVERSITY SCHOOL OF ADVANCED
STUDIES - IUSS PAVIA

**A Performance-Based Assessment of a Case Study Bridge and
Impact of Retrofitting Interventions**

A Thesis Submitted in Partial Fulfilment of the Requirements
for the Degree of Master of Science (Laurea Magistrale) in

Civil Engineering for the Mitigation of Risk from Natural Hazards

by

Savvinos Aristeidou

Supervisors:

Prof. Gian Michele Calvi, University School for Advanced Studies - IUSS Pavia

Dr. Gerard J. O'Reilly, University School for Advanced Studies - IUSS Pavia

PhD Candidate Volkan Özsaraç, University School for Advanced Studies - IUSS Pavia

September, 2020

ABSTRACT

With the rapidly increasing technological advancements and the minimization of computational effort, large sets of nonlinear time history analyses (NTHA) – 2D or 3D - are gaining more and more ground in seismic assessment and design verification of new structures. In this study, a probabilistic framework has been used to analyse and assess an existing case study bridge utilizing the concepts of performance-based earthquake engineering (PBEE).

In particular, two different methodologies were followed to calculate the structural losses: a rather simplified approach (HAZUS), and a more comprehensive one (FEMA P-58). The damageable components of the case study bridge that were examined, were principally the bridge piers in this study.

The eventual, and one of the most important, parameters extracted from this procedure was the expected annual loss (EAL) ratio, which is widely used for decision making during the seismic assessment or design of structures.

Furthermore, the case study bridge was retrofitted with several interventions which were also evaluated via the same framework and compared with the as-built bridge.

The main findings of the study were the relatively low monetary direct losses of the bridge, compared to buildings, even though the underlying seismic hazard was relatively high. The retrofitting interventions had the effect of reducing the structural demands and thus the direct losses, which have been already low. Additionally, the loss estimation between the simplified and comprehensive approach was seen to match very well in this study for both the pre- and post-retrofit structure, highlighting the adequacy of more simplified and direct approaches in the loss assessment of bridge structures.

Keywords: bridges; seismic assessment; retrofit; EAL; decision making.

ACKNOWLEDGEMENTS

I would like to thank my supervisor, Prof. Gian Michele Calvi, for his trust in me to conduct this work and his conceptual visions of the final outcomes. I am also thankful to my co-supervisor, Dr. Gerard J. O'Reilly, for his valuable contributions (with several tools and sharing his technical expertise) and suggestions regarding this research.

Special thanks go to PhD candidate Volkan Özsaraç, who developed many useful tools used in this research and was always available to answer my nonstop questions.

I would like to also thank Prof. Ricardo Monteiro¹ for his technical and organizational inputs.

Surely, all these wouldn't be possible without the inexhaustible support from my family and friends, spending quality time together and maintaining a healthy balance.

¹ University School for Advanced Studies - IUSS Pavia

TABLE OF CONTENTS

ABSTRACT	iii
ACKNOWLEDGEMENTS.....	v
TABLE OF CONTENTS.....	vii
LIST OF FIGURES	xi
LIST OF TABLES.....	xvii
1. Introduction.....	1
2. Literature Review	3
2.1 DAMAGE MECHANISMS IN REINFORCED CONCRETE BRIDGE PIERS.....	3
2.2 TYPES OF PERFORMANCE ASSESSMENT [FEMA P-58-1, 2018].....	6
2.2.1 Intensity-Based Assessments.....	6
2.2.2 Scenario-Based Assessments.....	7
2.2.3 Time-Based Assessments.....	7
2.3 MULTIPLE-STRIPE ANALYSIS METHOD.....	8
2.4 UNCERTAINTY [FEMA P-58-1, 2018]	9
2.4.1 Modelling Uncertainty.....	9
2.4.2 Record-to-Record Variability	11
2.5 STRUCTURE LEVEL DIRECT SEISMIC LOSS ASSESSMENT APPROACH.....	11
2.6 COMPONENT LEVEL DIRECT SEISMIC LOSS ASSESSMENT APPROACH.....	13
3. Description of the Case Study bridge.....	17
3.1 MEAN BRIDGE CONSTRUCTION AND REPLACEMENT COSTS	22
3.2 REPAIR ACTIONS AND MEAN REPAIR COSTS IN DAMAGEABLE COMPONENTS.....	25
4. Numerical Modelling of the As-Built Bridge Structure	27
4.1 MATERIALS	27
4.2 PIERS.....	29
4.3 PIER CAP	31

4.4 BEARINGS	31
4.5 DECK CHARACTERISTICS	37
4.6 DECK-BENT CAP-PIER CONNECTIVITY	39
4.7 ABUTMENT MODEL	40
4.8 LOADS AND MASSES	41
4.9 PUSHOVER ANALYSIS OF PIERS.....	41
4.10 SHEAR STRENGTH OF PIERS.....	43
5. Description of the interventions performed in the bridge.....	49
5.1 REPLACEMENT OF BEARING DEVICES WITH FRICTION PENDULUM ISOLATORS	50
5.2 STEEL JACKETING	51
5.3 CONCRETE JACKETING	52
5.4 COMPOSITE-MATERIALS JACKETING	54
6. Numerical Modelling of the Retrofitted Bridge Structure	56
6.1 FRICTION PENDULUM ISOLATORS.....	56
6.2 PIER STRENGTHENING INTERVENTIONS.....	58
6.2.1 Steel jackets	58
6.2.2 Concrete Jackets	60
6.2.3 Composite-Material Jackets	61
6.3 MOMENT-CURVATURE ANALYSES	62
6.4 PUSHOVER ANALYSIS OF PIERS.....	63
6.5 SHEAR STRENGTH OF PIERS	65
7. Direct Seismic Loss Assessment of the As-Built Bridge.....	69
7.1 SEISMIC HAZARD CHARACTERIZATION AND DISAGGREGATION.....	69
7.1.1 Choice of Intensity Measure.....	69
7.1.2 Geotechnical Information.....	70
7.1.3 Seismic Hazard & Disaggregation.....	72
7.2 GROUND MOTION RECORD SELECTION	78
7.3 STRUCTURAL ANALYSIS – MSA RESULTS	82
7.3.1 Piers.....	82
7.3.2 Bearings	83
7.4 DAMAGE MODELS	85

7.4.1 Abutments	85
7.4.2 Piers	87
7.5 FRAGILITY CURVES GENERATION	90
7.6 STRUCTURE LEVEL DIRECT SEISMIC LOSS ASSESSMENT	92
7.7 COMPONENT LEVEL DIRECT SEISMIC LOSS ASSESSMENT.....	92
7.8 COMPARISON OF SIMPLIFIED AND COMPREHENSIVE LOSS ASSESSMENT APPROACHES	96
8. Direct Seismic Loss Assessment of the Retrofitted Bridge.....	97
8.1 STRUCTURAL ANALYSIS – MSA RESULTS.....	98
8.2 DAMAGE MODELS.....	100
8.3 FRAGILITY CURVES.....	100
8.4 STRUCTURE LEVEL SEISMIC LOSS ASSESSMENT (DIRECT LOSSES)	102
8.5 COMPONENT LEVEL SEISMIC LOSS ASSESSMENT (DIRECT LOSSES)	102
8.6 COMPARISON OF SIMPLIFIED AND COMPREHENSIVE LOSS ASSESSMENT APPROACHES	106
9. Comparison between as-built and retrofitted model.....	107
10. Discussion and Conclusions.....	110
11. Possible Future Developments	112
REFERENCES	113
APPENDIX A. Miscellaneous bridge characteristics	117
APPENDIX B. Direct Loss Assessment and Structural Analysis Results of the As-Built Bridge	121
APPENDIX C. Direct Loss Assessment and Structural Analysis Results of the Retrofitted Bridge	
	143

LIST OF FIGURES

Figure 2.1. Typical Column Failure Modes: (a) Progressive Shear Failure, I-10 Santa Monica Freeway, Northridge Earthquake 1994; (b) Flexural Plastic Hinge Failures, I-10 La Cienega and Venice, Northridge Earthquake, 1994. [Seible, Priestley, Hegemier, & Innamorato, 1997].....	3
Figure 2.2. San Fernando Road Overhead damage in the 1971 San Fernando earthquake	4
Figure 2.3. Failure of columns of the Route 5/210 interchange during the 1971 San Fernando earthquake	4
Figure 2.4. Hanshin Expressway, Pier 46, damage in the 1995 Hyogo-Ken Nanbu earthquake ...	4
Figure 2.5. Failure of column with longitudinal reinforcement cut-offs near midheight in the 1995 Hyogo-Ken Nanbu earthquake	4
Figure 2.6. Failure of a two-column bent in the 1995 Hyogo-Ken Nanbu earthquake.....	5
Figure 2.7. Failure at the base of a column supported on a single cast-in-place pile in the 1971 San Fernando earthquake.	5
Figure 2.8. Flowchart of a general performance assessment procedure.	6
Figure 2.9. Flowchart of the procedure followed for the structure level approach for loss assessment.....	13
Figure 2.10. Flowchart of the procedure followed for the component level approach for loss assessment.....	16
Figure 3.1. Aerial view of the Bridge [Google Maps]	17
Figure 3.2. 3D drawing model of the Cingoli bridge.....	18
Figure 3.3. Three-Dimensional (3D) Simulation.....	18
Figure 3.4. Photograph of the Viaduct (March 2011)	19
Figure 3.5. Longitudinal view of the bridge.....	19
Figure 3.6. Plan view of the bridge	19
Figure 3.7. Elevation view of Pier 10, Pier Cap and plan view of bearings, as designed.....	20
Figure 3.8. Shear keys and bearings	21
Figure 3.9. Shear keys and bearings	21
Figure 4.1. Schematic representation of the concrete constitutive model.....	27

Figure 4.2. Steel02 Material – Material Parameters of Monotonic Envelope [OpenSees, 2006] ..	28
Figure 4.3. Pier cross sections and reinforcement information.....	29
Figure 4.4. Fibre section discretization scheme used in the numerical model	30
Figure 4.5. M- φ analysis of the two sections used in the numerical model.....	31
Figure 4.6. Schematic representation of bearing fixities. The arrows indicate free movement in that direction and the dots indicate a fixed condition.	32
Figure 4.7. Bearing UniT (P10).....	33
Figure 4.8.Bearing UniL (P10)	33
Figure 4.9. Typical arrangement of constraints in most spans	34
Figure 4.10. Hysteretic behaviour of the device in Transversal direction. Locking of the device upon expend of gap. Superimposition of the hysteretic curve provided by the manufacturer [FIP Industriale].....	36
Figure 4.11. Hysteretic behaviour of the device in Longitudinal direction. Locking of the device upon expend of gap.....	36
Figure 4.12. Bearing behaviour in the released direction	37
Figure 4.13. Geometrical configuration of the U Girder section.....	38
Figure 4.14. Deck geometrical configuration.....	38
Figure 4.15. Schematic representation of the Deck-Column frame model.	39
Figure 4.16. Abutment geometrical configuration from technical drawings	40
Figure 4.17. SDC 2010-2019 abutment model [Caltrans, 2019].....	40
Figure 4.18. Pushover curve of the Piers measuring the top displacement	42
Figure 4.19. Pushover curve of the Piers measuring the Pier Drift ratio.....	42
Figure 4.20. Pushover curve of the Piers, but depicted are the base shears and drifts of each individual column element comprising the Piers.....	43
Figure 4.21. γ factor as a function of curvature ductility – revised UCSD assessment model.....	45
Figure 4.22. Comparison of the Shear Strength degradation with the Pushover Curves, using the modified UCSD model [Kowalsky & Priestley, 2000].....	48
Figure 5.1. Schematic representation of the strengthening interventions in the piers of the bridge. (from technical drawings)	50
Figure 5.2. Schematic representation of the isolator design in undeformed configuration (left) and at maximum displacement (right)	50
Figure 5.3. Details of deck lifting.....	51
Figure 5.4. Cross section of a column retrofitted with steel jacketing (from technical drawings).52	52
Figure 5.5. Confinement of columns by concrete jacketing. [Priestley, Seible, & Calvi, 1996]....	53

Figure 5.6. Cross section of a column retrofitted with concrete jacketing. Reinforcement information.....	53
Figure 5.7. Retrofitting with composite-materials jackets. (a) High-strength fiberglass and epoxy: Hand-layup; (b) Carbon fibre and epoxy: machine winding. [Priestley, Seible, & Calvi, 1996].....	54
Figure 6.1. Properties of single Friction Pendulum (FP) bearing element [OpenSees, 2006].....	57
Figure 6.2. Confinement of concrete by circular and square hoops [Seismic Design and Retrofit of Bridges, Priestley, Seible, Calvi]	58
Figure 6.3. Enhancement of concrete compression strength by confinement [Seismic Design and Retrofit of Bridges, Priestley, Seible, Calvi]	60
Figure 6.4. Moment-Curvature analysis of the different retrofit strategies of the small section of the piers. Compared also with the as-built section.	62
Figure 6.5. Comparison between OpenSeesPy and SeismoStruct of the section retrofitted with steel jacket and the section retrofitted with FRP jacket.	63
Figure 6.6. Pushover curves of the retrofitted Piers	64
Figure 6.7. Pushover curves of the retrofitted Piers	64
Figure 6.8. Monitoring of the response of the individual columns comprising the retrofitted piers, during the pushover of the Piers	65
Figure 6.9. Shear strength degradation and Pushover curves of the retrofitted Piers, compared with the corresponding as-built Piers	68
Figure 7.1. Cumulative modal mass of the bridge versus vibration period	70
Figure 7.2. Location of the Cingoli site on the Italian hazard map of median PGA with 475 years return period on rock soil conditions. [European Facilities for Earthquake Hazard and Risk (EFEHR), 2017]	73
Figure 7.3. Hazard Curve for Cingoli site	73
Figure 7.4. Seismic Hazard Disaggregation – Cingoli site.	75
Figure 7.5. Location of the L'Aquila site on the Italian hazard map of median PGA with 475 years return period on rock soil conditions. [European Facilities for Earthquake Hazard and Risk (EFEHR), 2017]	76
Figure 7.6. Hazard Curves for L'Aquila site	76
Figure 7.7. Seismic Hazard Disaggregation – L'Aquila site.	78
Figure 7.8. Target Conditional Spectra, Geomean Spectra of Selected Ground Motion Pairs and their corresponding dispersion for each intensity.	82
Figure 7.9. MSA Results for Drift Ratio of Pier elements 7&13	83
Figure 7.10. Maximum displacement observed in the bearings during each record in each local direction.....	84

Figure 7.11. Indicative damage models for abutments.....	86
Figure 7.12. Damage Models of pier elements 7 & 12	90
Figure 7.13. Fragility curves of pier components for different damage limits	91
Figure 7.14. Structure fragility curves for different damage limits.....	91
Figure 7.15. Resultant loss curve using simplified approach (HAZUS).....	92
Figure 7.16. Sample loss distribution (a) Collapse cases (b) No Collapse Cases (c) All cases (for $T_r = 4975$ years events).....	93
Figure 7.17. Mean loss per component given no collapse (for $T_r = 4975$ years events).	94
Figure 7.18. Cost CDF and CCDF (for $T_r = 4975$ years events).	94
Figure 7.19. Loss curves per IM level and mean loss curve.....	95
Figure 7.20. Expected intensity-based and time-based losses using the comprehensive approach (FEMA-P58-1, 2018). (a) Loss vs IM level (b) loss curve.....	95
Figure 7.21. Comparison of simplified and comprehensive loss assessment approaches through the intensity-based and time-based loss curves.....	96
Figure 8.1. Cumulative modal mass of the bridge versus vibration period.....	97
Figure 8.2. MSA Results for Drift Ratio of Pier elements 7&13 of retrofitted model.....	98
Figure 8.3. Maximum displacement observed in the Inverted Friction Pendulum isolators (bearings) during each record in each local direction.....	99
Figure 8.4. Fragility curves of pier components for different damage limits.....	101
Figure 8.5. Structure fragility curves for different damage limits	101
Figure 8.6. Resultant loss curve using simplified approach (HAZUS).....	102
Figure 8.7. Sample loss distribution (a) Collapse cases (b) No Collapse Cases (c) All cases (for $T_r = 4975$ years events).....	103
Figure 8.8. Mean loss per component given no collapse (for $T_r = 4975$ years events)	104
Figure 8.9. Cost CDF and CCDF (for $T_r = 4975$ years events).....	104
Figure 8.10. Loss curves per IM level and mean loss curve.....	105
Figure 8.11. Expected intensity-based and time-based losses using the comprehensive approach (FEMA-P58-1, 2018). (a) Loss vs IM level (b) loss curve.....	105
Figure 8.12. Comparison of simplified and comprehensive loss assessment approaches through the intensity-based and time-based loss curves.....	106
Figure 9.1. Comparison of Pier element 15 peak drift ratios between the as-built and retrofitted model.....	107
Figure 9.2 Comparison of the median drift ratios of each pier between the retrofitted and as-built structure for an IM level.	108

Figure 9.3 Loss curves from comprehensive and simplified approach crossed with the as-built and retrofitted model..... 109

LIST OF TABLES

Table 2.1 Recommended values of dispersion associated with the level of building definition and construction quality assurance, and the quality and completeness of the nonlinear analysis model [FEMA P-58].....	10
Table 2.2. Damage ratios per Damage State.....	11
Table 3.1. Adopted unit prices from A.N.A.S. S.p.A. 2018-unit price list.....	22
Table 3.2. Adopted over-price factors.....	23
Table 3.3. Unit replacement costs implemented in previous studies.....	24
Table 3.4. Repair activities for abutments at each damage state	25
Table 3.5. Repair activities for pier at each damage state.....	26
Table 3.6. Adopted over-price factors on material costs to account for labour and machinery costs in repair actions by component at each damage state	26
Table 4.1. Material Parameters used for the unconfined and confined concrete. Recommended parameters from [OpenSees, 2006].....	27
Table 4.2. Additional Concrete Mechanical Properties used in the calculations	28
Table 4.3. Material Parameters used for the reinforcement steel.....	29
Table 4.4.Wholistic fixities at the ends of spans (0: DOF is released, 1: DOF is fixed).....	33
Table 4.5. Specifications of each type of bearing device.....	35
Table 4.6. Unit and distributed weights in the structure.....	41
Table 7.1. Selected period range for AvgSa	70
Table 7.2. Soil Profile - Constant profile is assumed along the bridge length.....	70
Table 7.3. Ground types distinguished by Eurocode 8 and some of their corresponding parameters [EN 1998-1 2004].....	71
Table 7.4. Nine chosen intensity levels. Probability of exceedance in 50 years and corresponding Intensity Measure level. Cingoli site.....	74
Table 7.5. Nine chosen intensity levels. Probability of exceedance in 50 years and corresponding Intensity Measure level. L'Aquila site	77
Table 7.6. Damage limits for abutments found in literature.....	85

Table 7.7. Assigned damage model values for abutments in the transverse direction	86
Table 7.8. Column parameters used to generate the database. [Perdomo & Monteiro, 2020].....	87
Table 7.9. Pier parameters of Cingoli Bridge	88
Table 8.1. Predominant period range of retrofitted structure.....	98
Table 9.1. Comparison of Expected Annual Loss Ratio between the As-Built and Retrofitted model.....	107
Table A.1. Modal Periods, Damping and Modal Mass Participating Factors.....	117
Table A.2. Mean repair cost of pier components at each damage state	120

1. Introduction

Bridges play a critical role in the infrastructure, well-being and development of a country, and their functionality after a major disaster, such as an earthquake, is essential. It is, thus, important to estimate their seismic vulnerability and performance in a rational and accurate manner.

Bridges often given the impression of being simple structural systems, however many (even modern) bridges have collapsed or sustained severe damage, when subjected to ground shaking of intensities lower than those stipulated by current codes. In the majority of the developed world, the greater expansion of freeway and highway systems took place before the modern bridge design codes and advanced technical regulations had been developed. Additionally, deterioration, fatigue and previous strong ground motions resisted by these bridges weaken and alternate their structural integrity. Ergo, the assessing and retrofitting of existing bridges has gained a lot of popularity in recent years, with decision-making regarding the budget allocation for the interventions on bridges, with higher priority, becoming more and more relevant.

The risk assessment of structures through state-of-the-art performance-based earthquake engineering (PBEE) approaches is crucial to be performed in a rational and comprehensive manner. Decision makers (i.e. insurance companies, stakeholders, owners etc.) will make decisions based on the outcomes of these assessments, hence it is important to portray the existing risk of the structure with the utmost accuracy.

In this study, an application of site-specific performance-based seismic assessment to a case study bridge was carried out, for both the as-built structure and the retrofitted structure. Even though these probabilistic procedures for seismic assessment have focused mainly on buildings, rather than bridges, in recent studies. The objective of the work was to explore a rational way of quantifying the performance of a real bridge and find some key components that affect the performance the most.

The three main interventions performed and analysed in the case study bridge structure were: (a) deck made continuous (from independent simple spans), (b) the metallic bearings were replaced with friction pendulum isolators, and (c) the piers were strengthened with

concrete, steel and carbon-fibre jacketing. The effect of these interventions on the structure's performance was explored through the methodology described below.

Two different methodologies were followed to calculate the structural losses: a simplified approach (presented in HAZUS [FEMA, 2003]) and a more comprehensive one [FEMA P-58, 2018]. The first one is a structure level approach and the second a component level approach. The purpose of this work was to apply these methodologies to a real existing bridge in Italy, which was modelled with great detail, to understand both the effect of different particularities on the bridge's seismic risk and the level of practicability of these methodologies in reality. Furthermore, the retrofitted structure was analysed through the same framework so that the impact of the typical retrofitting strategies adopted in practice for this bridge typology could be explored.

A 3D model of the structure was built and, performing an eigenvalue analysis, the structural periods with the highest mass participation factors were found. Using those periods, with the average spectral acceleration (AvgSa) as the seismic intensity measure (IM), the hazard curve and hazard disaggregation for the site under study was calculated, through probabilistic seismic hazard analysis (PSHA), described further on. Nine different intensity levels with their corresponding probabilities of exceedance (PoE) were chosen as adequate to depict a suitable range of rates of exceedance of ground motions. Based on the seismic hazard disaggregation, the dominating pairs of magnitude and distance for each PoE were found and 40 pairs of ground motions for each PoE were selected for the numerical analyses. The record selection was carried out utilizing the conditional spectrum (CS) approach and selecting records with similar magnitude and distance pair as the dominating one. The records were then scaled so that their mean AvgSa and dispersion were matched to the corresponding target mean conditional spectrum and its dispersion.

The bridge was subsequently analysed under the action of those ground motion pairs, applied in the two horizontal directions, without the inclusion of the vertical component, to characterize the chosen engineering demand parameters (EDPs) (in this case the maximum pier drifts). From these EDPs, utilizing adequate damage models, the damage in the piers was quantified in a probabilistic manner. These damage states were then translated into direct monetary losses, through the use of corresponding consequence functions for such bridge typologies. This procedure mentioned above sums up to a standard component-based loss assessment.

2. Literature Review

2.1 DAMAGE MECHANISMS IN REINFORCED CONCRETE BRIDGE PIERS

In seismic design and assessment of bridges, piers are the components that attract the lion's share of the attention. Some damage mechanisms observed in reinforced concrete piers during past earthquakes are described below.

Bridges are designed so that their lateral-load carrying capacity is limited by the flexural strength of columns. All other elements (e.g. footings, joints, bearings/isolators, beams etc.) are capacity designed and yielding is first anticipated in the piers. Therefore, piers should be able to withstand large inelastic demands during the strong ground motion, without exhibiting premature failure.

Oftentimes, collapse in bridges is caused from pier failures, attributed to inadequate detailing, which limits the ability of the pier to undertake inelastic deformations. The failure mechanism can be flexural, shear, splice or anchorage failure, or even a combination of those. Piers are a particularly vulnerable component, especially the ones in bridges designed before 1971, where the transverse reinforcement was light and rarely bent towards the core of the piers and thus the provided confinement to the concrete was very limited. Observed column shear failure and flexural plastic hinge failure, during the Northridge Earthquake 1994, are shown in Figure 2.1. The insufficient design and detailing of transversal and longitudinal reinforcement are evident in both columns.

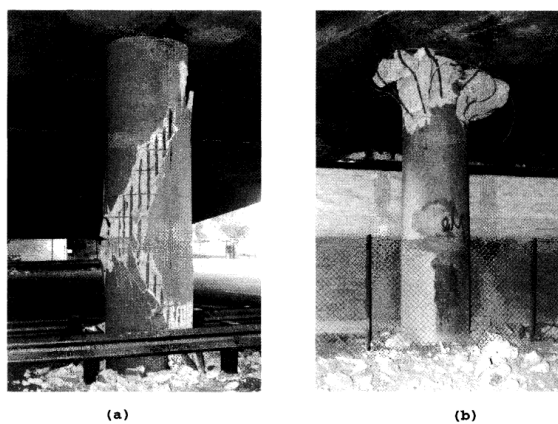


Figure 2.1. Typical Column Failure Modes: (a) *Progressive Shear Failure, I-10 Santa Monica Freeway, Northridge Earthquake 1994;* (b) *Flexural Plastic Hinge Failures, I-10 La Cienega and Venice, Northridge Earthquake, 1994.* [Seible, Priestley, Hegemier, & Innamorato, 1997]

Damages to the columns, due to insufficient flexural ductility, during the 1971 San Fernando earthquake can be seen in Figure 2.2. Under several horizontal deformation cycles, with acting gravity loads, a column can degrade so much, that it can lose its gravity load-carrying capacity, which appears to have happened in the columns of Figure 2.3.



Figure 2.2. San Fernando Road Overhead damage in the 1971 San Fernando earthquake.



Figure 2.3. Failure of columns of the Route 5/210 interchange during the 1971 San Fernando earthquake.

Similar flexural damage in the base hinge of the column is shown in Figure 2.4, product of the 1995 Hyogo-Ken Nanbu earthquake. Figure 2.5 depicts the failure of a column with its longitudinal bars terminated near mid-height.



Figure 2.4. Hanshin Expressway, Pier 46, damage in the 1995 Hyogo-Ken Nanbu earthquake.



Figure 2.5. Failure of column with longitudinal reinforcement cut-offs near midheight in the 1995 Hyogo-Ken Nanbu earthquake.

Overly strong and non-ductile bents (columns, bent caps and joints) are not capable of limiting the damages in bridges, as indicated in Figure 2.6. This failure shattered several parts of the bent.



Figure 2.6. Failure of a two-column bent in the 1995 Hyogo-Ken Nanbu earthquake.

Another failure mechanism that has been observed in bridge piers is the failure due to inadequate anchorage of the longitudinal reinforcement. Figure 2.7 shows a column that failed at its base, due to insufficient anchorage length driven inside the foundation, that was cast-in-place piles. Single-column bents are more prone to a collapse due to anchorage failure, since they depend on the column developing its flexural strength at the base for the development of lateral-force resistance.



Figure 2.7. Failure at the base of a column supported on a single cast-in-place pile in the 1971 San Fernando earthquake.

2.2 TYPES OF PERFORMANCE ASSESSMENT [FEMA P-58-1, 2018]

The performance of a structure can be assessed through three types of performance assessments: intensity-based, scenario-based, and time-based assessments. The procedure of a performance assessment of a structure from a broad perspective is shown in Figure 2.8.

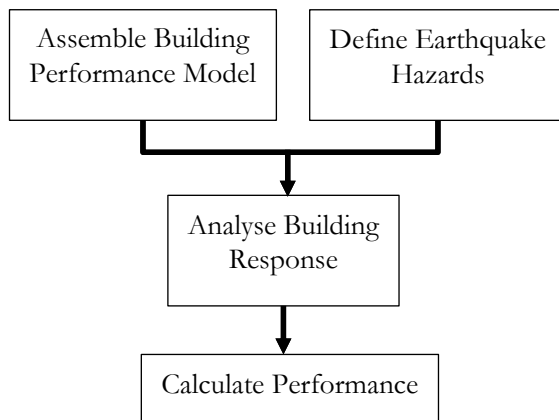


Figure 2.8. Flowchart of a general performance assessment procedure.

2.2.1 Intensity-Based Assessments

Intensity-based assessments evaluate the probable performance of a structure, subjected to a specified earthquake shaking intensity. Shaking intensity is oftentimes defined by a user-selected acceleration response spectrum intended to be representative of the uniform hazard spectrum identified during PSHA. In this study, it is defined by 5% damped, elastic, acceleration conditional response spectra. This type of assessment can also be used to assess the performance of a structure for a design earthquake shaking consistent with a building code response spectrum, for example design earthquake (DE) shaking or maximum considered earthquake (MCE) shaking in the United States [ASCE/SEI 7-10, 2010].

Intensity-based assessments can be used to determine probable maximum loss (PML), or other scenario loss measures^b, and use these measures to evaluate the structure's (bridge in this case) performance and make investment decisions.

2.2.2 Scenario-Based Assessments

Scenario-based assessments evaluate the probable performance of a structure, subjected to a user-selected earthquake scenario consisting of a specific magnitude earthquake occurring at a specific location relative to the structure site. This type of assessment is useful for sites located close to one or more known active faults or can be used to assess the performance of a building in a historic earthquake, or a future projected earthquake.

Scenario-based assessments are similar to intensity-based assessments except that they consider uncertainty in the intensity of earthquake shaking, given that the scenario occurs. Results of scenario-based assessments are performance functions, except that the probable performance is conditioned on the occurrence of the specified earthquake scenario, rather than a specified shaking intensity, as in intensity-based assessment.

2.2.3 Time-Based Assessments

Time-based assessments evaluate the probable performance of a building over a specified period of time (e.g. 1 year, 30 years or 50 years) considering all earthquakes that could occur in that time period, and their corresponding probability of occurrence. Time-based assessments consider uncertainty in the magnitude and location of future earthquakes as well as the ground motion intensity resulting from these earthquakes.

The time period for time-based assessment depends on the interests and needs of the decision-maker. Assessments based on a single year are useful for cost-benefit evaluations used to decide between alternative performance criteria. Assessments over longer periods of time are useful for other decision-making purposes. For example, risk-averse decision-makers might prefer to base their decisions on a loss with specific anticipated probability of occurrence, or return period, such as 10-year, 50-year or 100-year losses.

Time-based assessments provide performance functions that express the frequency that an impact of a certain size (e.g., number of casualties, repair costs, or weeks of construction time) will be exceeded in a period of time.

^b These include: scenario expected loss (SEL), scenario upper loss (SUL), etc.

A decision parameter that could be derived directly from a time-based assessment is the probable loss (PL), which represents the loss having a specific probability of exceedance, over a specified number of years.

The expected (or probable) loss can be evaluated for several discrete hazard levels, and the expected annual loss (EAL) can be computed by numerical integration over the hazard, as indicated in Equation (2.6). This is a rather powerful decision variable, as it permits, for selected design alternatives, direct comparison of expected annual losses over the full range of hazards, rather than committing to specific hazard levels [Krawinkler, Zareian, Medina, & Ibarra, 2006]. This decision variable seems particularly attractive for a structure that has assorted components of significant value, with different ‘relevant’ EDPs (i.e. drift, displacement and acceleration sensitive components), for example in bridges, where there are piers, abutments and bearings etc. and each has its own most ‘relevant’ EDP. Hence, in those cases, an integrated loss measure appears to be much more objective than one associated with a specific hazard level.

Considering all the above, it was decided that a time-based assessment, with EAL as the decision parameter, would most objectively describe the performance of the case study bridge and was used herein. Additionally, intensity-based assessment is also partially implemented and presented during the analysis of the bridge.

2.3 MULTIPLE-STRIPE ANALYSIS METHOD

Multiple-stripe analysis (MSA) is a non-linear dynamic analysis method in which, ‘stripes’ of structural response values are obtained by subjecting a structural model to a suite of ground motion records scaled to multiple levels of intensity measure (e.g. spectral acceleration) level. A single IM is selected and EDP data are obtained for many different ground motion records, providing an one dimensional ‘stripe’ of the response data [Mackie & Stojadinovic, 2005]. Statistics of a ‘stripe’ can be worked out to estimate median and fractional standard deviation at each intensity level.

The incremental dynamic analysis (IDA) or cloud analysis are other examples of wide-range non-linear dynamic analyses that can be used in probabilistic seismic demand modelling. The MSA was selected to be utilized for the current study, because nine different predefined hazard levels (or probabilities of exceedance in 50 years) are going to be examined under the performance-based earthquake engineering framework. Another benefit of a MSA is that the median and dispersion estimates do not include model errors (due to mathematical form) [Mackie & Stojadinovic, 2005].

2.4 UNCERTAINTY [FEMA P-58-1, 2018]

Nonlinear response history analyses can provide estimates of median response, from a reasonable amount of analyses, but a large, impractical amount of analyses, with inherent modelling assumptions, is required to obtain statistically reliable estimates of uncertainties (dispersion) in demand associated with modelling assumptions and the correlations between demand parameters. In order to avoid these excessive analyses, demand parameter dispersions can also be estimated based on judgment regarding the inherent uncertainty in response calculation. Because of probable inaccuracies in dispersion and correlation that would be observed in small suites of analyses, the use of assumed values of uncertainty is considered suitable with all available information.

Three sources of demand parameter uncertainty are generally considered: (1) modelling uncertainty; (2) record-to-record variability; and (3) ground motion variability. However, because scenario-based assessments are not in the current scope of this study, the ground motion variability is omitted. Since procedures such as MSA inherently incorporates the dispersion associated with record-to-record variability, it is augmented to account for modelling uncertainty in the generation of simulated sets for loss computations.

The total dispersion of the fragility curve comes from the contribution of 3 distinct dispersion components, calculated by assuming that the response follows a lognormal distribution as follows:

$$\beta_{tot} = \sqrt{\beta_{mod}^2 + \beta_{res}^2 + \beta_{cap}^2} \quad (2.1)$$

where, β_{tot} is the total uncertainty (dispersion) on the fragility curve, β_{mod} is the modelling uncertainty, β_{res} is the dispersion due to record-to-record variability, computed with the MSA and maximum likelihood estimation (MLE) [Baker, 2015] procedures. Additionally, β_{cap} is the uncertainty in defining the capacity point via the chosen EDP and corresponds to the dispersion values coming from the damage models.

2.4.1 Modelling Uncertainty

Modelling uncertainty, β_{mod} can be directly taken into account through the sampling of statistically significant but nominally identical bridges (paired afterwards with a unique ground motion in a randomized fashion) by assigning statistical distributions to as many bridge parameters as considered necessary (as in e.g. [Nielson & DesRoches, 2007], [Kameshwar & Padgett, 2017]).

Otherwise, best-estimate analytical models can be used for analysis, and calculated dispersions are augmented by judgmentally determined values accounting for modelling

uncertainty. Modelling uncertainty is a product of the inaccuracies in component modelling, damping and mass assumptions. Thus, the modelling uncertainty can be taken into account indirectly according to the following equation:

$$\beta_m = \sqrt{\beta_q^2 + \beta_c^2} \quad (2.2)$$

where β_c corresponds to uncertainty of the construction quality and β_q corresponds to uncertainty due to the analytical model completeness, can be taken as 0.25 and 0.25, respectively, in accordance to the recommendations from FEMA P-58, for average construction quality assurance and average quality of the analytical model. It is noted that these recommendations generally apply to buildings but were assumed to be reasonable estimates in the case of bridge structures for the purposes of this study.

Table 2.1 Recommended values of dispersion associated with the level of building definition and construction quality assurance, and the quality and completeness of the nonlinear analysis model [FEMA P-58].

Table 5-1 Values of Dispersion for Construction Quality Assurance, β_c

Building Definition and Construction Quality Assurance	β_c
Superior Quality, New Buildings: The building is completely designed and will be constructed with rigorous construction quality assurance, including special inspection, materials testing, and structural observation.	0.10
Superior Quality, Existing Buildings: Drawings and specifications are available and field investigation confirms they are representative of the actual construction, or if not, the actual construction is understood. Material properties are confirmed by extensive materials testing.	0.25
Average Quality, New Buildings: The building design is completed to a level typical of design development; construction quality assurance and inspection are anticipated to be of limited quality.	0.25
Average Quality, Existing Buildings: Documents defining the building design are available and are confirmed by visual observation. Material properties are confirmed by limited materials testing.	0.40
Limited Quality, New Buildings: The building design is completed to a level typical of schematic design, or other similar level of detail.	
Limited Quality, Existing Buildings: Construction documents are not available and knowledge of the structure is based on limited field investigation. Material properties are based on default values typical for buildings of the type, location, and age of construction.	

Table 5-2 Values of Dispersion for Quality of the Analytical Model, β_q

Quality and Completeness of the Analytical Model	β_q
Superior Quality: The numerical model is robust over the anticipated range of response. Strength and stiffness deterioration and all likely failure modes are explicitly modeled. Model accuracy is established with data from large-scale component tests through failure.	0.10
Completeness: The mathematical model includes all structural components and nonstructural components in the building that contribute to strength or stiffness.	
Average Quality: The numerical model for each component is robust over the anticipated range of displacement or deformation response. Strength and stiffness deterioration is fairly well represented, though some failure modes are simulated indirectly. Accuracy is established through a combination of judgment and large-scale component tests.	0.25
Completeness: The mathematical model includes most structural components and nonstructural components in the building that contribute significant strength or stiffness.	
Limited Quality: The numerical model for each component is based on idealized cyclic envelope curves from ASCE/SEI 41-13 or comparable guidelines, where strength and stiffness deterioration and failure modes are not directly incorporated in the model.	0.40
Completeness: The mathematical model includes structural components in the seismic-force-resisting system.	

Building definition and construction quality assurance uncertainty, β_c , accounts for the possibility that the actual properties of structural elements might differ in reality, than those prescribed. Quality and completeness of the analytical model, β_q , accounts for possible inaccuracies of the hysteretic models to capture the behaviour of structural components. Regardless of the relative values of β_c and β_q , the total uncertainty computed using Equation (2.2) should not be greater than 0.5.

2.4.2 Record-to-Record Variability

Each record will produce somewhat different prediction of peak response quantities in the structure, resulting in record-to-record variability. Using a large number of ground motion pairs (on the order of 30 or more), the values of dispersion as well as the correlation between response quantities are generally considered to be accurate enough. In any case, this methodology assumes that record-to-record response variability and demand correlation coefficients computed using even small numbers of ground motions are sufficiently accurate for performance assessment, as augmented for other sources of uncertainty.

2.5 STRUCTURE LEVEL DIRECT SEISMIC LOSS ASSESSMENT APPROACH

In structure level approach, the vulnerability of the system is controlled by the most damaged component in the system, at each predefined damage limit threshold. In this study only piers were considered as damageable component, so their vulnerability controls the vulnerability of the system.

Using the damage fragility curves developed with the results from the selected structural analysis approach (as explored in Section 7.5), scenario losses (i.e. for a given IM level) are computed using compound damage ratios, where the damage ratio DR_i is assigned for being in damage state DS_i and $P[DS_i]$ is the probability of being in DS_i .

Damage states (DSs) are sorted from 0 (corresponding to no damage) to 4 (corresponding to collapse). The damage state definitions DS_i and the damage ratios, DR_i , are taken to be the same as in HAZUS [FEMA, 2003] and are presented in Table 2.2.

The expected loss ratio for each intensity level is computed with the Equation (2.3), where the DR_i is multiplied with the probability of being in DS_i , summed over the four damage states considered. The expected loss is calculated from the Equation (2.4), where C_{REP} is the bridges' mean replacement cost. The associated standard deviation accompanying the expected loss can be calculated from the Equation (2.5).

Table 2.2. Damage ratios per Damage State

Damage State	DR
No Damage (DS_0)	0
Slight/Minor (DS_1)	0.03
Moderate (DS_2)	0.08
Extensive (DS_3)	0.25
Complete (DS_4)	1

$$\mu_{D|IM} = \sum_{i=1}^4 DR_i P[DS_i|IM] \text{ where } P[DS_i|IM] = \begin{cases} p[D \geq DL_j|IM] - p[D > DL_{j+1}|IM] & \rightarrow j=1,2,3 \\ p[D \geq DL_j|IM] & \rightarrow j=4 \end{cases} \quad (2.3)$$

$$\mu_{L|IM} = \mu_D \cdot C_{rep} \leq C_{rep} \quad (2.4)$$

$$\sigma_L = \mu_L \sqrt{\sum_{i=1}^4 (DR_i - \mu_D)^2 P[DS_i]} \quad (2.5)$$

Finally, the loss curve can be constructed from the results of each IM level and the EAL ratio can be computed using the Equation (2.6), multiplying the expected loss with the annual rate of exceedance of each intensity measure level and numerically integrating over all intensity measure levels.

$$EAL[\epsilon] = \int_{IM} \mu_{L|IM}[\epsilon] \left| \frac{d\lambda_{IM}}{dIM} \right| dIM \quad (2.6)$$

This approach is usually preferred for large scale/regional assessments.

It can be seen that in this approach the only parameter that is not deterministic is the damage state of the structure for a given IM, which is taken from the structure's fragility curves.

The flowchart in Figure 2.9 illustrates the procedure of the structure level direct loss assessment approach.

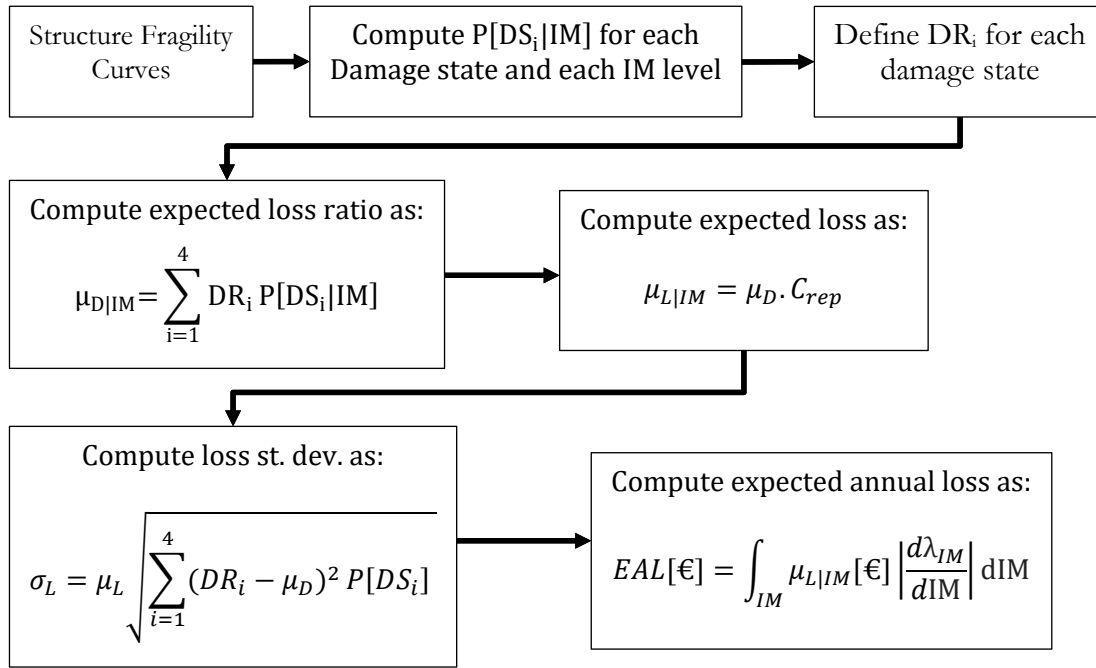


Figure 2.9. Flowchart of the procedure followed for the structure level approach for loss assessment.

2.6 COMPONENT LEVEL DIRECT SEISMIC LOSS ASSESSMENT APPROACH

In the component level approach, the damage state of each individual component is evaluated through their corresponding damage models. Subsequently, damage consequences are then evaluated for each individual component and are finally aggregated to assess the condition of the whole system. Herein, the piers are considered as the only damageable component.

The component level approach adopted follows the general procedure prescribed by the FEMA P-58-1 [2018] guidelines for practical implementation of the PEER-PBEE framework, put into an equation as follows:

$$\lambda(DV) = \iiint G\langle DV | DM \rangle dG\langle DM | EDP \rangle dG\langle EDP | IM \rangle d\lambda(IM) \quad (2.7)$$

where:

- $\lambda(DV)$: Rate of exceedance of the Decision Variable
- DV: Decision Variable
- DM: Damage Measure
- EDP: Engineering Demand Parameter
- IM: Intensity Measure
- G: Conditional Complementary Cumulative Distribution Function

$$\lambda_L = \iiint P[L|DS] P[DS|EDP] P[EDP|IM] \cdot \lambda_{IM} dIM dEDP dDS \quad (2.8)$$

Equation (2.8) was solved numerically in a sequential fashion by working out each one of its components. The term λ_{IM} corresponds to the annual rate of exceedance. In this work the chosen EDPs were the drift ratio of piers, which are obtained from the piers' top displacement divided by their corresponding height.

Following current practice, the limited results from the structural analysis (40 ground motion pairs at each IM level as per the record selection procedure) were used to simulate a larger number of synthetic responses (realizations). The [Yang et al., 2006; Yang et al., 2009] algorithm, contained in Appendix G of FEMA P-58-1 [2018], was implemented to create the simulated demands that represent the conditional distribution of EDPs given the IM level and 25000 realizations per IM level were enough to obtain small discrepancies in expected annual losses between two independent runs of the procedure.

In order to distinguish 'collapse' from 'no-collapse' cases, random sampling on the collapse fragility curve was performed as follows. When a pier is deemed to enter a state of complete damage (DS-4), the structure is deemed to enter a state of collapse and the repair activity considered is the bridge replacement. Here, a collapse fragility curve was created, separately from the structure fragility curve (no-collapse cases) to separate 'collapse' and 'no-collapse' cases. The collapse fragility curve is retrieved from the results of the structure level approach and at a given IM level and realization, the probability of collapse is read. Then, a random number between 0 and 1 is generated. If the generated number is lower than that probability of collapse, the bridge is considered to enter a state of collapse and the repair activity is the bridge replacement; otherwise, with the results from the simulated realization, the loss evaluation in each individual component is carried out. This is essentially the approach adopted in FEMA P-58-1 [2018].

The term $P[DS|EDP]$ represents the conditional distribution of being in a predefined damage state, given a value of EDP response. These relationships are described by the damage models discussed in Section 7.4.2 for the piers. For a given structural response

value (EDP), of a component, the probabilities of exceeding a damage limit ($p[DL-1]$, $p[DL-2]$ and $p[DL-3]$, and $p[DL-4]$) are determined from the damage models. The complementary probabilities (i.e. $1-p[DL-j]$) are then computed. Then, a random number between zero and one (with uniform distribution) is generated, utilizing the Monte Carlo method of repeated random sampling. If the random number is lower than $1-p[DL-1]$ the component is deemed to be in a state of no-damage; if the random number is between $1-p[DL-1]$ and $1-p[DL-2]$ the component is deemed to be in a state of slight damage; if the random number is between $1-p[DL-2]$ and $1-p[DL-3]$ the component is deemed to be in a state of moderate damage; and if the random number is larger than $1-p[DL-3]$ the component is deemed to be in a state of extensive damage. With this approach the loss assessment is performed in all the damageable components (only piers in this study) defined.

The term $P[L|DS]$ represents the conditional probability of the loss value of a component, being in a particular damage state, as described in Section 3.2. When a component (pier) is deemed to enter in a particular damage state, its final repair cost is randomly generated by sampling a value from the statistical distribution of the repair cost of that component in that damage state.

After the same procedure was conducted for all IM levels, a loss curve was defined and EALs were computed using Equation (2.6) , with the same manner as for the structure level approach. Finally, Equation (2.8) can be solved numerically, using the CCDFs computed, for each IM level by implementing equation (2.9) [FEMA P58-1, 2018].

$$\lambda(L > l) = \int_{\lambda} P(L > l | IM = im) d\lambda(im) \quad (2.9)$$

Where, $\lambda(L > l)$ is the annual rate of exceedance of a given value of loss (λ_L in equation (2.8)), $P(L > l | IM = im)$ is the loss CCDF for a given IM level, from an intensity-based assessment, and $d\lambda_{IM}$ is the annual rate of exceedance of an infinitesimal range of IMs. The resulting losses, is a parameter obtained from the overall time-based assessment.

A brief flowchart of the procedure described above, is presented in Figure 2.10.

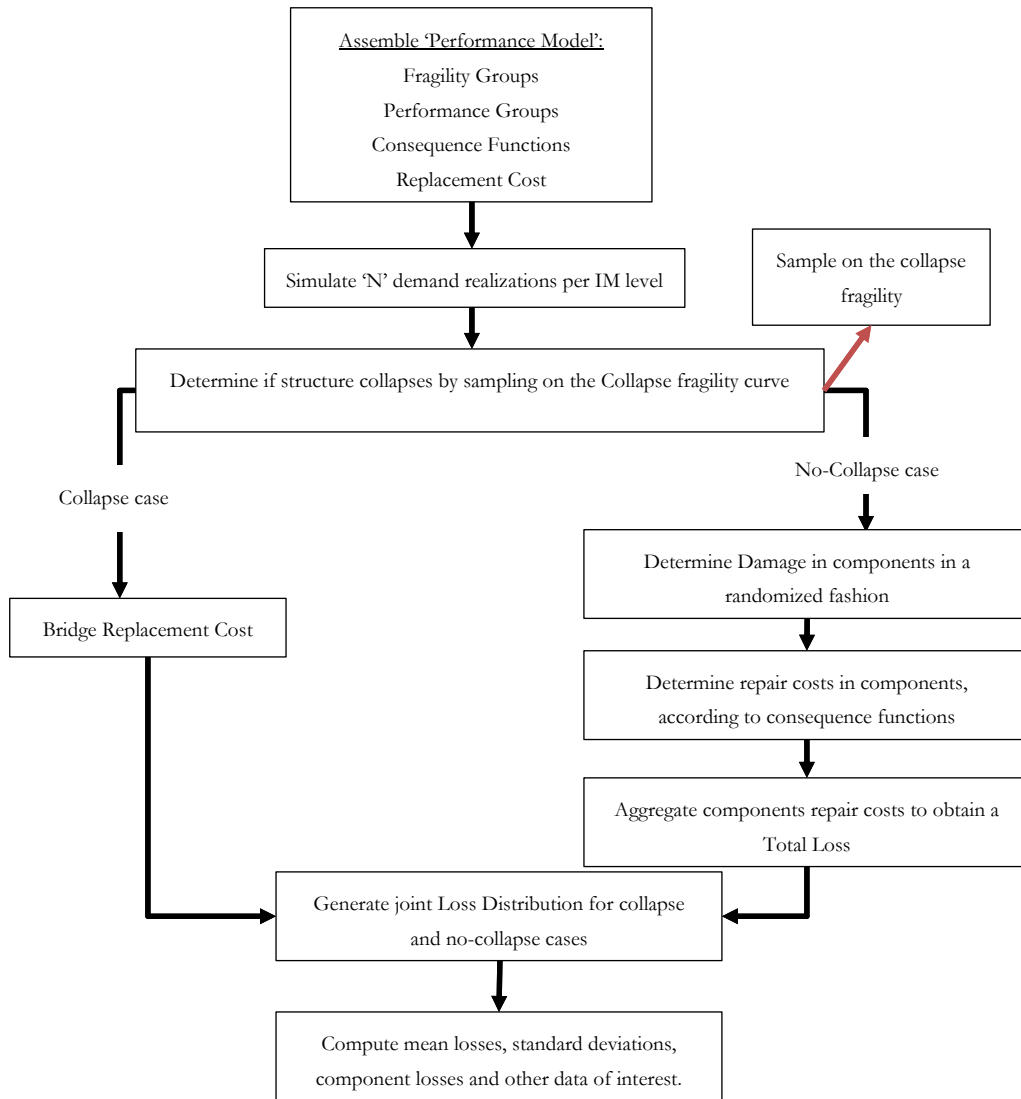


Figure 2.10. Flowchart of the procedure followed for the component level approach for loss assessment.

3. Description of the Case Study bridge

The bridge under consideration is located in the Marche region in Italy and more specifically in the Province of Cingoli and therefore termed the ‘Cingoli Bridge’ herein. It belongs to a local transport infrastructure complex and it traverses the Castreccioni dam, which stores drinkable water. This bridge is considered a very important structure for the community, as it falls into the provisions for emergency management in case of any disaster (natural or not) and it is crucial for the functionality of the dam.

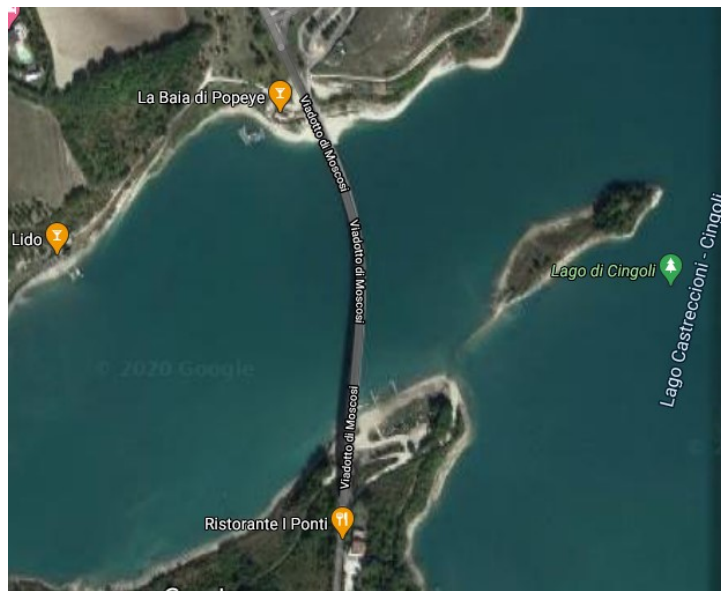


Figure 3.1. Aerial view of the Bridge [Google Maps]

The bridge is composed of 14 spans with a centerline length between piers of 31.60m, except the first and last span, which both have a length of 30.60m. The spacing between the central supports of each span is 29.60m and the width of the deck is 10.7m, of which 8.6m is the carriageway. Three box-shaped girders support the deck, placed at a spacing of 3.60m from each other, joined together with diaphragm beam at each support. Each deck span is simply supported to the pier cap and disconnected to the adjacent deck span, except from a simple expansion joint, which ideally doesn't transmit any forces.

The bridge is also partially curved in both plan and elevation. The three-dimensional drawing and simulation of the bridge is shown in Figure 3.2 and Figure 3.3.

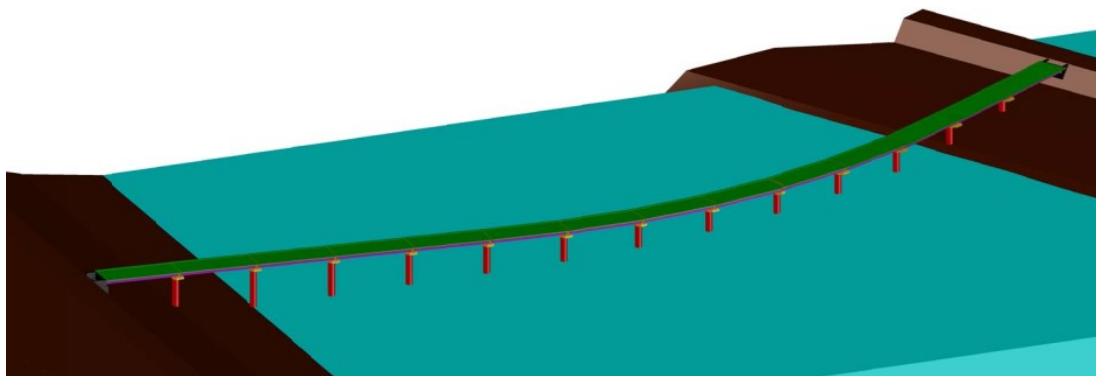


Figure 3.2. 3D drawing model of the Cingoli bridge.



Figure 3.3. Three-Dimensional (3D) Simulation

The pier caps have rectangular section with varying height (e.g. from 1.55m in the middle to 0.8m at the ends) and are integrated with the circular section piers of varying height. The piers are composed of two portions: the lower portion has a diameter of 4m and the upper portion a diameter of 2.6m. There are 13 piers with height varying from about 7.2m to about 31.5m. Piers are all founded on shallow foundation with square footings, except for pier 7 which also has micropiles.

A close-up photograph of the as-built bridge is shown in Figure 3.4.



Figure 3.4. Photograph of the Viaduct (March 2011)

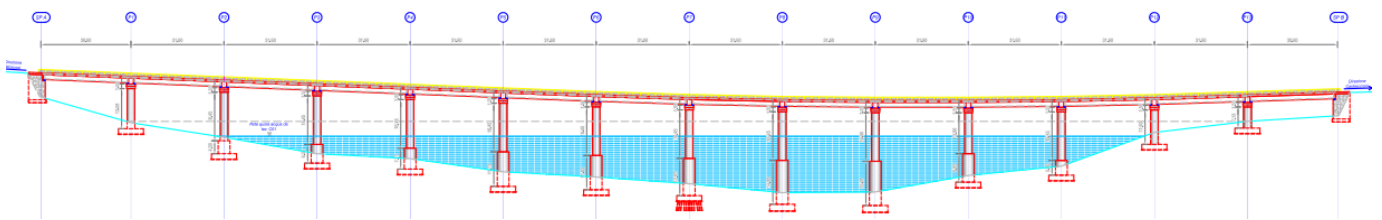


Figure 3.5. Longitudinal view of the bridge

The vertical curve of the bridge deck is visible in the longitudinal profile of the bridge in Figure 3.5.

The configuration of each independent deck element, can be seen from the plan view of Figure 3.6. Additionally, some details of the pier, pier cap and deck cross-section are given in Figure 3.7.

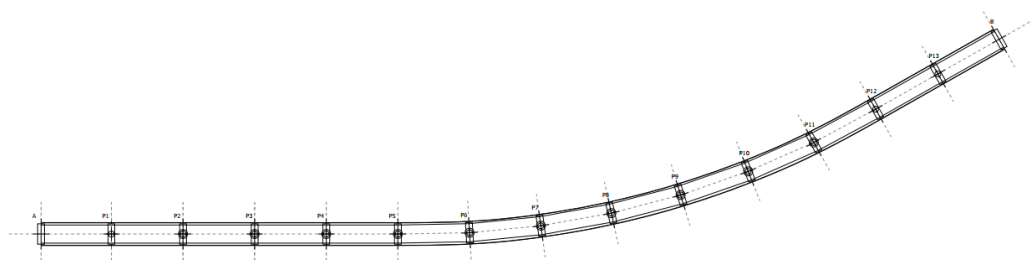


Figure 3.6. Plan view of the bridge

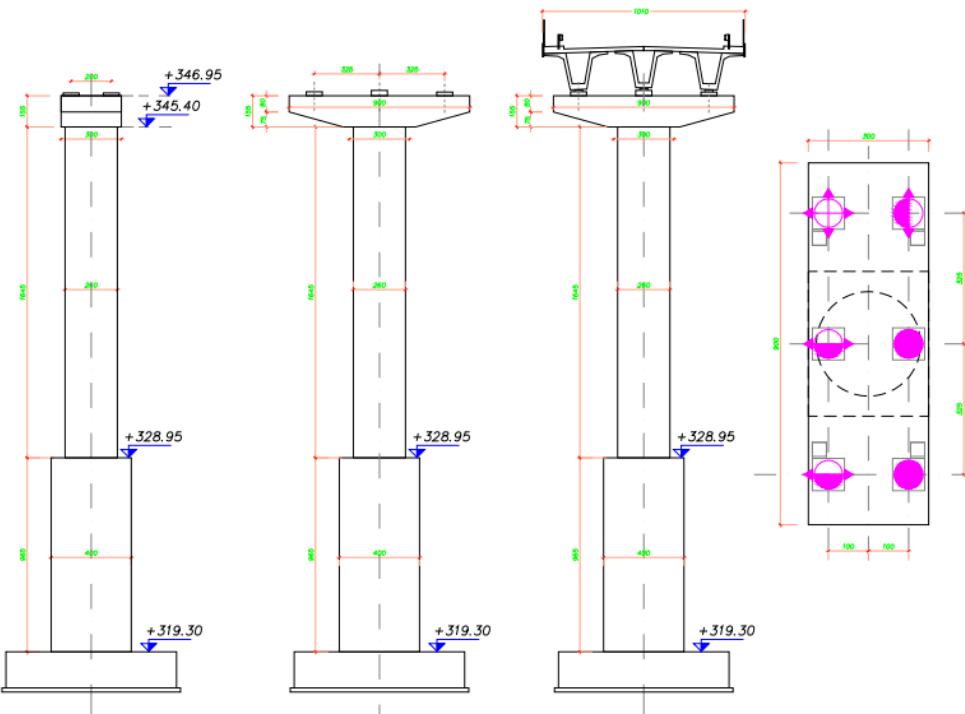


Figure 3.7. Elevation view of Pier 10, Pier Cap and plan view of bearings, as designed

The bearings under the diaphragm beam, and shear keys and generally the condition near the supports can be seen through the photographs given in Figure 3.8 and Figure 3.9. The deterioration is evident in various spots, which gives another cause for the retrofitting interventions.



Figure 3.8. Shear keys and bearings



Figure 3.9. Shear keys and bearings

3.1 MEAN BRIDGE CONSTRUCTION AND REPLACEMENT COSTS

The estimation of mean repair costs and bridge replacement costs are typically calculated separately. Mean repair costs for the piers and replacement cost for Cingoli Bridge was obtained using a typical practitioner approach [Zanini, Faleschini, & Pellegrino, 2016]. Unit prices for material quantities were adopted to estimate costs. Accordingly, unit prices from the Italian governmental agency A.N.A.S. S.p.A. [2018] (see Table 3.1). The demolition cost was computed based on the total concrete volume of all the components. With the following assumptions, the material quantities employed in the construction of the different bridge components were computed and the final costs were resulted, using the unit-price list. Labour costs and machinery were considered indirectly using over-price factors (see Table 3.2), thus increasing the costs of materials.

Table 3.1. Adopted unit prices from A.N.A.S. S.p.A. 2018-unit price list.

Activity or Material	Unit	Price (€)	Code in the reference document
Asphalt	m ³	95	Assumed
Concrete	m ³	169.76	B.03.035 + B.03.040
fc' ≥ 55 MPa		162.78	
50 MPa ≤ fc' < 55 MPa		132.58	
45 MPa ≤ fc' < 50 MPa		126.05	
40 MPa ≤ fc' < 45 MPa		118.22	
35 MPa ≤ fc' < 40 MPa		106.46	
Demolition	m ³	99.68	A.03.008
Superstructure Components		25.3	A.03.019
Substructure Components		180.2	A.03.007
Excavation	m ³	3.25	A.01.001
Fill material complying with Proctor compaction tests	m ³	70	Assumed
Formwork	m ²	37.62	B.04.001
Superstructure		22.19	B.04.003
Substructure		30.76	B.04.004.f
Substructure Repairing		364.64	B.04.012.a
Pile Construction	m	481.76	B.02.035d + B.02.046.d
D = 1.5m		151.73	B.02.035b
D = 1.0m		108.03	B.02.035a
Prestressing Steel	kg	2.59	B.05.057

Railings	kg	2.15	B.05.017c
Reinforcing Steel	kg	1.04	B.05.030
Cleaning and superficial treatment	m ²	21.18	B.09.212
Concrete Patch	m ³	178.76	B.04.003
Crack Sealing in Concrete	m	191	Assumed
Demolition of Cover Concrete	m ³	289.84	A.03.007

Table 3.2. Adopted over-price factors

Component	Over-Price Factor
Superstructure	1.8
Abutments	1.5
Piers	1.6
Cap-Beams	1.6
Footings	1.5
Piles	1.8

Firstly, the bridge was assumed to have a slab-and-beam superstructure with no continuity at the inner supports, but simple independent spans ‘connected’ with expansion joints moving freely. The construction process involves the placement of the girders on top of the bearings and the slab cast on top of the girders. The superstructure is supported over cap-beam and non-sacrificial shear keys are implemented for the transference of shear to the piers and the foundation, after the exceedance of the ultimate displacement of the bearings. Secondly, to keep the calculations practical, some simplified assumptions were made regarding the superstructure characteristics (given the limitations of the technical information), that do not differ a lot from reality: (i) the cross section area of the slabs is considered to be 50% of the total cross section area, (ii) the average thickness of the slabs was considered to be 0.20m, (iii) the average ratio of reinforcing steel weight to concrete volume in slabs is assumed to be 150kg/m³, (iv) the average ratio of reinforcing steel weight to concrete volume in the longitudinal beams is assumed to be 100kg/m³, (v) the average ratio of prestressing steel weight to deck area is assumed to be 17kg/m², (vi) it is assumed that the protection elements at the edges of the deck are railings and each one of them has a weight of 100kg/m, (vii) it is assumed that the average asphalt thickness is 0.05m.

With regards to the piers, the quantification of the materials employed in their construction was possible, with the additional assumption that anchorage lengths for reinforcement were of 1.0m into the foundation footing and cap-beam. The unit reinforcing steel weight was taken as 7800kg/m³. For the cap-beams idealized rectangular section assumed, with the

ratio of steel weight to concrete volume assumed at 140kg/m³. Regarding the abutment structure, all abutments were deemed to be seat-type earth retaining walls with shallow foundation, and the following characteristics were assumed: (i) the average total height was set as 5.0m, the total length in the transverse direction was assumed to be same as the deck width, (iii) the back-wall thickness was set as 0.30m, the back-wall height was set at 1.90m, as the span length is between 20m and 30m (iv) the wing-walls thickness as set as 0.30m, (v) the wing-walls length was set as 4.0m, (vi) the seat-wall thickness was set as 1.50m, (vii) the foundation footing width (length on the longitudinal direction) was set as 2.50m, the foundation footing thickness was set as 1.50m, and, the average reinforcing steel weight to concrete volume in the abutments was set as 90kg/m³. With these assumptions, material quantities for the abutments' construction were computed. When it comes to the piers' foundation, the ratio steel weight to concrete volume in the column's footings was assumed to be 120 kg/m³, in order to account for the micropiles underneath the central pier, the foundation replacement cost was increased by 10%. If the foundation was not defined there would be additional assumptions made for the bridge based on the V_{s30} value of the site.

The unitary cost for Cingoli bridge (€/Deck Area) was obtained as 1304 €/m², and the total replacement cost was estimated roughly at 5,732,046 €. For the sake of comparison, typical values found in the literature are given in the Table 3.3.

Table 3.3. Unit replacement costs implemented in previous studies

Study	Unit Replacement Cost	Sources
Furtado and Alipour [2014]	160 USD/ft ²	Division of Engineering Services, California Department of Transportation [2013]
Dong and Frangopol [2015]	2306 USD/m ²	Decò <i>et al.</i> [2013]
Miano <i>et al.</i> [2016]	851.4 euros/m ² (c.o.v. 0.155 Lognormal dist.) <SCDOT> 2343 euros/m ² (c.o.v. 0.587 Exponential dist.)	*SCDOT [--] South Carolina Department of Transportation *Basöz <i>et al.</i> [1999] *Moehle <i>et al.</i> [1995] *Nilsson [2008] *Padgett <i>et al.</i> [2010a] *Padgett <i>et al.</i> [2010b] *Yasinsky [1997]
Padgett <i>et al.</i> [2010a]	Concrete Girder 67.71 USD/ft ² Concrete Box Girder 67.98 USD/ft ² Steel Girder 94.37 USD/ft ² Slab 60.04 USD/ft ² Other 75.23 USD/ft ² \	SCDOT - South Carolina Department of Transportation [2007]

3.2 REPAIR ACTIONS AND MEAN REPAIR COSTS IN DAMAGEABLE COMPONENTS

In order to define the repair cost at each predefined damage state, a series of repair activities were assigned, for abutments and piers, required to bring the component to its pre-damaged state. These activities are defined in Table 3.4 for abutments and Table 3.5 for piers. When a pier is deemed to enter a state of complete damage (DS-4), then the structure is deemed to enter a state of collapse and the repair activity is considered as the bridge replacement. The costs for the materials required for the repair activities have also been retrieved from Table 3.1 [ANAS S.p.A, 2018], in the same manner as for the replacement cost, over-price factors on material costs were used to account for labour and machinery costs in each one of those activities, and are shown in Table 3.6. Although, the repair actions for the abutments and their associated costs were estimated, these were not included in the loss estimation calculations since the damage models for the abutments have not been perfected yet. The obtained repair costs are given in Table A.2 in appendix A. These costs are the mean values, which were assumed to be lognormally distributed with a dispersion value of 0.4. The mean replacement cost was also assumed to be lognormally distributed but with a dispersion value of 0.5. These high dispersion values reflect the large uncertainties around the estimation of the repair costs for each damage state.

Table 3.4. Repair activities for abutments at each damage state

DS	Description	Activities
DS-1	Slight Damage: Cleaning	Cleaning and superficial treatment
DS-2	Moderate Damage: wing- walls repairing	Concrete patch in affected wing-walls
		Formwork for concrete patch
		Back-fill excavation over the height of the back wall
		Crack sealing in back-fill side
		Back-fill replacement
		Asphalt replacement
DS-3	Extensive Damage: Abutment replacement	Temporal support of superstructure
		Back-fill excavation
		Abutment Demolition
		Abutment Reconstruction
		Back-fill regrading
		Asphalt replacement

Table 3.5. Repair activities for pier at each damage state

DS	Description	Activities
DS-1	Slight Damage: Crack Sealing	Sealing of cracks with epoxy injection
DS-2	Moderate Damage: Spalled concrete repairing	Demolition of cover concrete over a height of max. 3 times the column diameter
		Cleaning and surface preparing
		Concrete patching
		Formwork for patched concrete
DS-3	Extensive Damage: Pier replacement	Temporal support of superstructure
		Demolition of existing pier and cap-beam
		Intervention in the foundation
		Pier and cap-beam reconstruction
		Pier and cap-beam formwork

**Table 3.6. Adopted over-price factors on material costs to account for labour
and machinery costs in repair actions by component at each damage state**

DS	Component	
	Abutments	Piers
DS-1	1.1	1.15
DS-2	1.2	1.5
DS-3	1.4	1.5

4. Numerical Modelling of the As-Built Bridge Structure

4.1 MATERIALS

The materials used in the bridge and the modelling of those are described as follows.

Concrete:

From the provided technical information, it was found that the concrete used was of the class C25/30. For the modelling of this material, the Modified Kent-Scott-Park (1971) concrete model (Concrete01 in OpenSees) was used for concrete fibres. Residual strength of unconfined concrete fibres was taken as 0. Confinement factor was calculated after Mander confined concrete model [Mander, Priestley, & Park, 1988]. The information provided below describes the material properties:

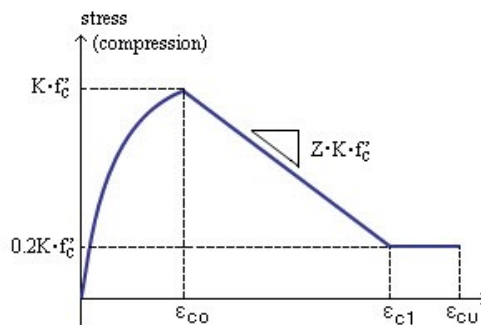


Figure 4.1. Schematic representation of the concrete constitutive model

**Table 4.1. Material Parameters used for the unconfined and confined concrete.
Recommended parameters from [OpenSees, 2006]**

<u>Unconfined concrete</u>	<u>Confined concrete</u>
$f'_c = 25 \text{ MPa}$	$f_{cc}' = K \cdot f'_c$
$\epsilon_{c0} = 0.003$	$\epsilon_{c0} = 2K \cdot f'_c / E_c$
$\epsilon_{c1} = 0.01$	$\epsilon_{c1} = 5\epsilon_{c0}$
$f_{c,\text{Residual}} = 0$	$f_{c,\text{Residual}} = 0.2K \cdot f'_c$

Table 4.2. Additional Concrete Mechanical Properties used in the calculations

Tensile strength	$f_t = 0 \text{ kN/m}^3$
Modulus of Elasticity	$E_c = 5000(f_c')^{0.5} (\text{MPa}) = 25 \text{ GPa}$
Poisson Ratio	$\nu = 0.2$
Shear Modulus	$G_c = E_c / (2*(1+\nu)) = 10.417 \text{ GPa}$
Unit weight of reinforced concrete	$\gamma_c = 25 \text{ kN/m}^3$

Reinforcement Steel:

From the available technical information, it was found that the reinforcing steel used was of the class Feb44k, with its modelled mechanical properties given in Table 4.3. For steel fibres, the Giuffré-Menegotto-Pinto Model with Isotropic Strain Hardening (Steel02 in OpenSees) constitutive model was used. In order to account for steel buckling and fracture, MinMax material was used along with Steel02, to eliminate the stress in the steel when the strain reaches a 0.1 threshold, which was taken as the fracture strain limit of the bars.

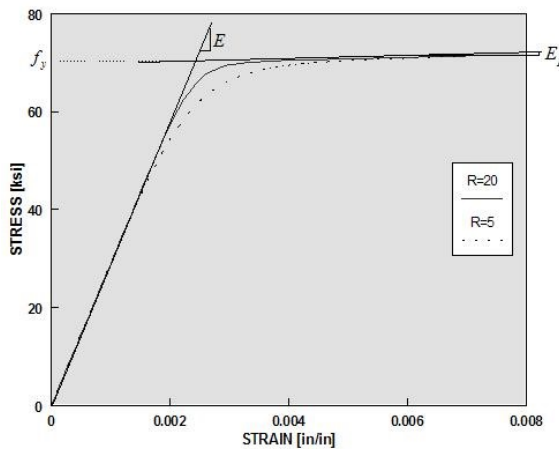
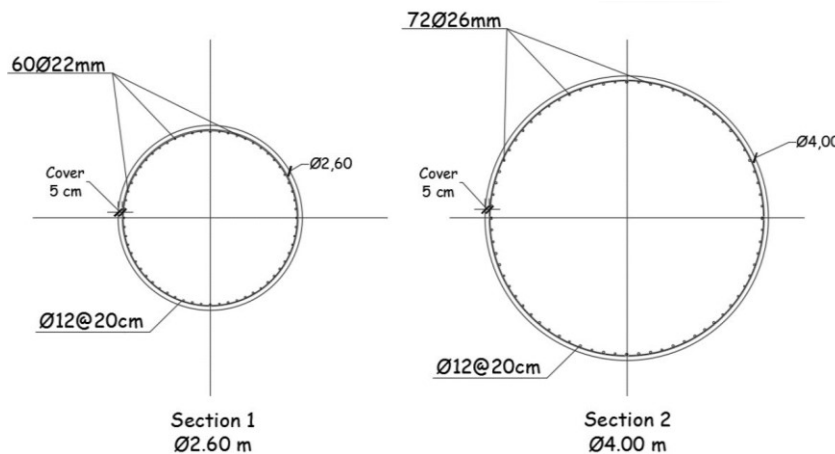
**Figure 4.2. Steel02 Material – Material Parameters of Monotonic Envelope [OpenSees, 2006]**

Table 4.3. Material Parameters used for the reinforcement steel

Yield stress	$F_y = 430 \text{ MPa}$
Modulus of elasticity	$E_s = 200 \text{ GPa}$
Strain-hardening ratio (ratio between post-yield tangent and initial elastic tangent)	$B_s = 0.005$
Parameters to control the transition from elastic to plastic branches	$R_0 = 18 \mid cR1 = 0.925 \mid cR2 = 0.15$
Maximum/minimum strain (Fracture/Buckling strain)	± 0.1

4.2 PIERS

All piers are composed from 2 sections varying over height, except P1, P12 and P13, which have only 1 section. This discontinuity is creating an abrupt setback in the cross-section diameter of the piers. The reinforcement information and cross section geometry is given in Figure 4.3.

**Figure 4.3. Pier cross sections and reinforcement information**

It should be noted that the piers, as built, had $\Phi 12\text{mm}/20\text{cm}$ stirrups with open hooks (not closed at 135degrees, or spiral stirrups) therefore not very effective in the event of an earthquake. However, In the numerical modelling and the confinement calculations, they were assumed to be effectively closed.

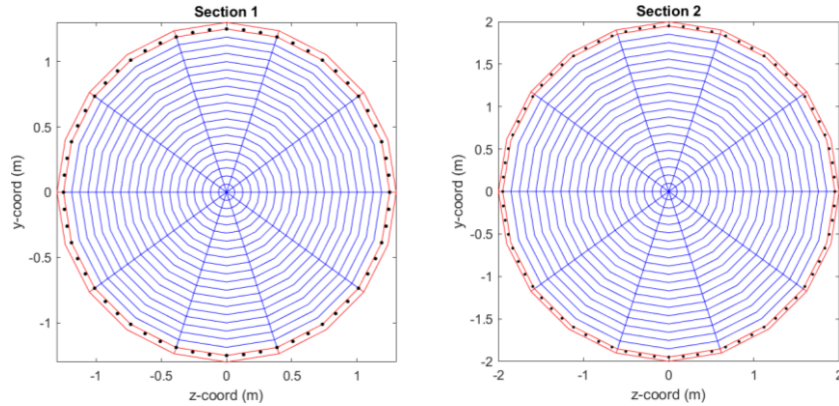


Figure 4.4. Fibre section discretization scheme used in the numerical model

Force-based beam-column elements, having distributed plasticity, with 5 integration points along their length were used to model the piers.

From the details of the transversal reinforcement, extracted from the technical drawings, the confinement factor was calculated. It was found to be **1.0327** for the 4m diameter section and **1.0494** for the 2.6m diameter section. The confinement factors are very low for the as-build section, indicating that there is an inadequate amount of transversal reinforcement for seismic and ductility considerations.

Below are the moment-curvature analysis results obtained for the sections, where the axial load applied corresponds to just an average load acting in the lowest section of the piers, used just for comparative purposes:

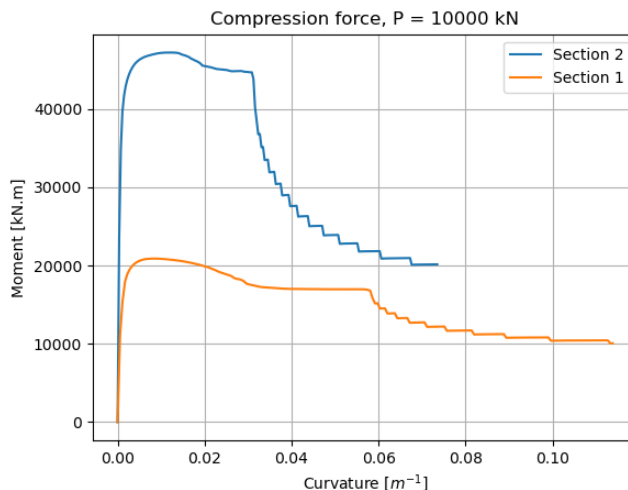


Figure 4.5. M- ϕ analysis of the two sections used in the numerical model.

From Figure 4.5 it can be seen that section 2 (larger section) has a higher ultimate moment capacity, but less curvature ductility, than section 1 (smaller section). This is due to the higher section diameter, the more longitudinal bars and the larger diameter of those bars.

4.3 PIER CAP

The pier (or bent) caps are modelled using elastic beam-column elements since no inelastic behaviour was anticipated. In the existing structure, the bent caps have varying section, but they are modelled as a constant equivalent rectangular cross section, as it was considered to be adequately accurate for the purposes of this study. The geometrical properties assigned to the pier cap elements were 3m x 1.5m for the height and width of the cross-section, respectively, and 9m for the length of the element.

4.4 BEARINGS

The bearing devices used in this bridge is of a particular type of metallic bearings, dubbed as CEP bearings, which are no longer used in modern practice. The configuration of the bearing fixities is provided in Figure 4.6. Four different typologies are present in the bridge and listed as follows:

- 1) Free in both directions
- 2) Transversally restrained
- 3) Longitudinally restrained
- 4) Both directions are restrained

All bearings lock when they expend the available gap space. The fixities of degrees of freedom (DOF) at the joint, between deck and bent cap, in case the bearings were to modelled as one lumped bearing at each support are given in Table 4.4. However, the modelling approach followed was to model each bearing at its position in the bridge, connected with rigid links to the deck above and to the bent cap below.

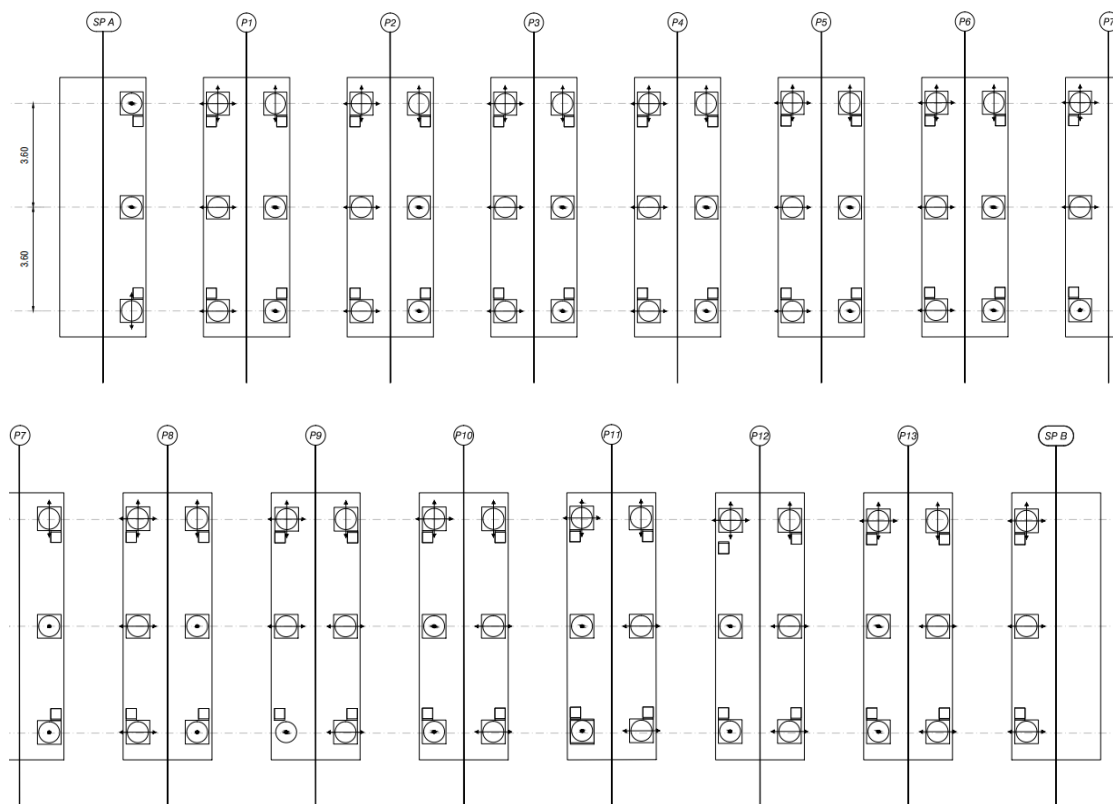


Figure 4.6. Schematic representation of bearing fixities. The arrows indicate free movement in that direction and the dots indicate a fixed condition.

Table 4.4. Wholistic fixities at the ends of spans (0: DOF is released, 1: DOF is fixed)

FIXITY AT THE START OF SPANS														
Span No	1	2	3	4	5	6	7	8	9	10	11	12	13	14
DOF X	1	1	1	1	1	1	1	1	1	1	1	1	1	1
DOF Y	1	1	1	1	1	1	1	1	1	1	1	1	1	1
DOF Z	1	1	1	1	1	1	1	1	1	1	1	1	1	1
DOF rX	1	1	1	1	1	1	1	1	1	1	1	1	1	1
DOF rY	0	0	0	0	0	0	0	0	0	0	0	0	0	0
DOF rZ	1	1	1	1	1	1	1	1	1	1	1	1	1	1
FIXITY AT THE END OF SPANS														
Span No	1	2	3	4	5	6	7	8	9	10	11	12	13	14
DOF X	0	0	0	0	0	0	1	0	1	1	1	1	1	0
DOF Y	1	1	1	1	1	1	1	1	1	1	1	1	1	1
DOF Z	1	1	1	1	1	1	1	1	1	1	1	1	1	1
DOF rX	1	1	1	1	1	1	1	1	1	1	1	1	1	1
DOF rY	0	0	0	0	0	0	0	0	0	0	0	0	0	0
DOF rZ	1	1	1	1	1	1	1	1	1	1	1	1	1	1

Photographs of the bearings from the site were extracted from the technical reports and presented in Figure 4.7 and Figure 4.8, for the transversally free and longitudinally free bearing, respectively.



Figure 4.7. Bearing UniT (P10)



Figure 4.8. Bearing UniL (P10)



Figure 4.9. Typical arrangement of constraints in most spans

There are guides in the bearings that allow the relative displacement between the deck and the pier cap along their parallel direction. Additionally, the guides resist the movement in their perpendicular direction, through small rods (pins) that work as hysteretic dissipators.

The diameter of the pin head is 40mm + a slack of 6mm in the holes to obtain a total available diameter of 46mm. The slots are arranged in such a way that peg works perpendicularly to them. None of the hysteretic dissipating peg should hit the longitudinal end of the slot, otherwise a greater force than the design force would take place (locking).

For example, the fixed CEP comprises 4 circular holes in the corners with 46mm diameter and 2 central slotted holes with 146mm length, so that they can allow the free displacement of $\pm 50\text{mm}$ to the 2 central rungs in the transversal direction. Hence, it can be perceived that 6 pins work in the longitudinal direction and 4 in the transverse direction.

In the unidirectional transversal (UniT) bearing, the slots are all 146mm in length in the transverse direction. In the unidirectional longitudinal (UniL) bearing, the slots have a length of 176mm to allow $\pm 65\text{mm}$ sliding in addition to the head dimension (40mm) and 6mm slack.

These free movements are allocated as: $\pm 50\text{mm}$ of seismic deformation and additionally $\pm 15\text{mm}$ thermal + shrinkage deformation only in the longitudinal direction.

Table 4.5. Specifications of each type of bearing device

Type	H _L (kN)	H _T (kN)	Long. holes	Trans. holes	d _L (mm)	d _T (mm)
Fixed	170	120	6 non-slotted	6, from which 2 are slotted	±65	±50
Transversally restrained	0	120	4 slotted	4 non-slotted	±65	±50
Longitudinally restrained	170	0	6 non-slotted	6 slotted	±65	±50
Released in both directions	0	0	0	0	±65	±50

where,

- H_L = Longitudinal resistance
- H_T = Transversal resistance
- d_L = Longitudinal displacement prior to the activation of the internal locking
- d_T = Transversal displacement prior to the activation of the internal locking

If a bearing is released in a direction, there is only a gap and the hysteretic energy dissipating pins do not work. In general, the four types of bearings can be summed up to:

1. ‘Fixed’ case: The pins are working, dissipating hysteretic energy in both directions, as shown in Figure 4.10 and Figure 4.11. The gap is ±50mm in the transversal and ±65mm in the longitudinal direction. Upon reaching this displacement capacities, an internal shear key is activated. In order to simulate this behavior, gap elements were used, in parallel with a bilinear elasto-plastic material (Steel02 in OpenSeesPy).
2. UniT device: The gap length in the two directions is the same as in the ‘fixed’ case. The pins are transmitting force, within the gap space, only in the longitudinal direction, whereas in the transversal direction is free to move.
3. UniL device: The gap length in the two directions is the same as in the ‘fixed’ case. The pins are transmitting force, within the gap space, only in the transversal direction, whereas in the longitudinal direction is free to move.
4. ‘Free’ case in both directions: There is no transmission of force inside the bearing. It is free to move in both directions, until the gap margin is used. The gap lengths are the same as in the ‘fixed’ case.

The validation of the modelled bearing hysteresis curve with the one provided by the manufacturer is given in Figure 4.10. The behaviour of the bearing in the longitudinal

direction is given in Figure 4.11 and the behaviour along the ‘released’ direction in Figure 4.12.

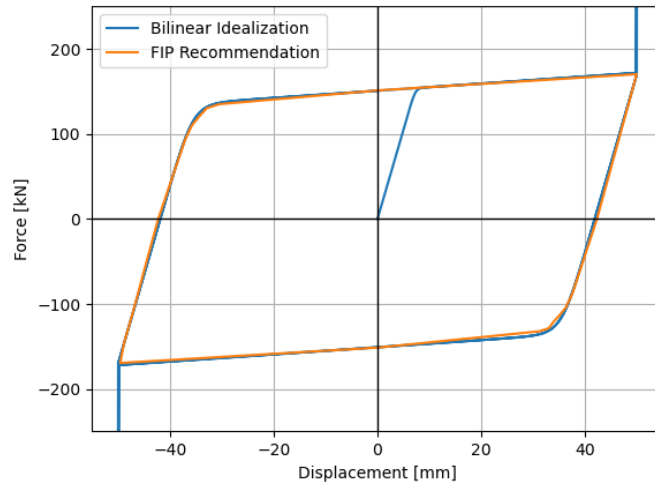


Figure 4.10. Hysteretic behaviour of the device in Transversal direction. Locking of the device upon expend of gap. Superimposition of the hysteretic curve provided by the manufacturer [FIP Industriale].

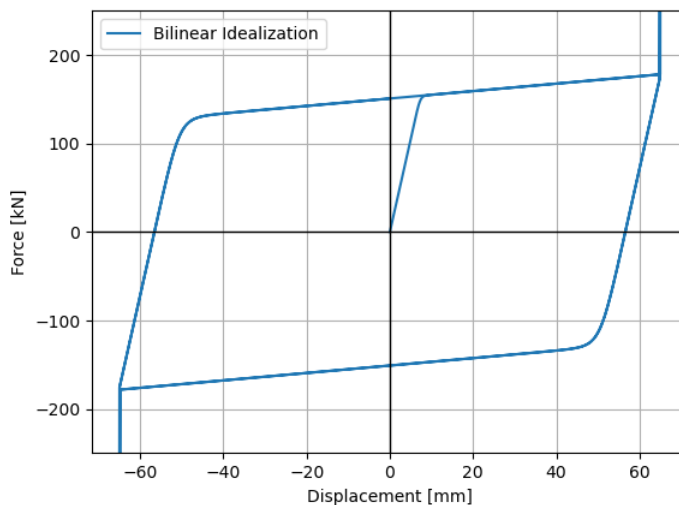


Figure 4.11. Hysteretic behaviour of the device in Longitudinal direction. Locking of the device upon expend of gap

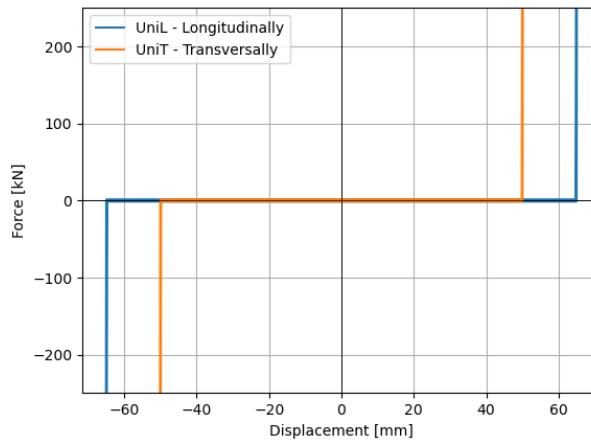


Figure 4.12. Bearing behaviour in the released direction

4.5 DECK CHARACTERISTICS

Some of the cross-sectional properties of the whole deck cross-section (slab integrated with girders) are listed as follows:

- Cross-section (axial) area = 4.922 m^2
- Moment of Inertia about the horizontal axis = 2.028 m^4
- Moment of Inertia about the vertical axis = 46.068 m^4
- Torsional constant = 1.653 m^4

The geometrical configurations of the girder and deck cross-section are indicated in Figure 4.13 and Figure 4.14, respectively.

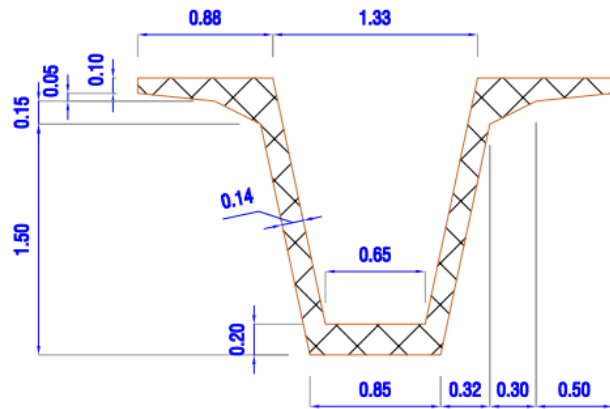


Figure 4.13. Geometrical configuration of the U Girder section

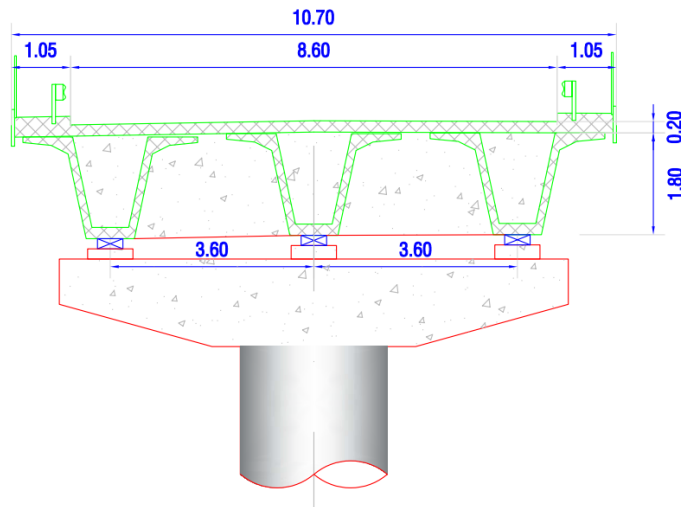


Figure 4.14. Deck geometrical configuration

The composite deck-girder section was modelled with three linear elastic beam/column elements, with the mechanical properties of the concrete, as discussed above. The rigid diaphragm constrained was properly assigned to mimic the restraining effect of the slab. At the ends the girders are connected together with a diaphragm beam.

The girders and the diaphragm beam subsequently rest on metallic bearings, placed on top of the pier cap. There are also some shear keys attached to the pier cap to restrain the deck from falling off, in case of failure of a bearing or exceedance of their maximum displacement capacity.

The total superimposed dead load on the deck was assigned to be 39.8 kN/m of span length. This static load also represents the additional mass considered in the seismic response of the structure.

4.6 DECK-BENT CAP-PIER CONNECTIVITY

The bearings, which are placed on top of the bent cap, are modelled as zero-length elements, whose nodes are rigidly connected with the deck elements and bent caps. In Figure 4.15, the frame elements of the numerical model are depicted. The approach that was used to model the bridge, was to model the three girders, with their corresponding portion of deck slab on top (with properly assigning in-plane diaphragm) and the bearings distributed along the bent cap, according to their actual position.

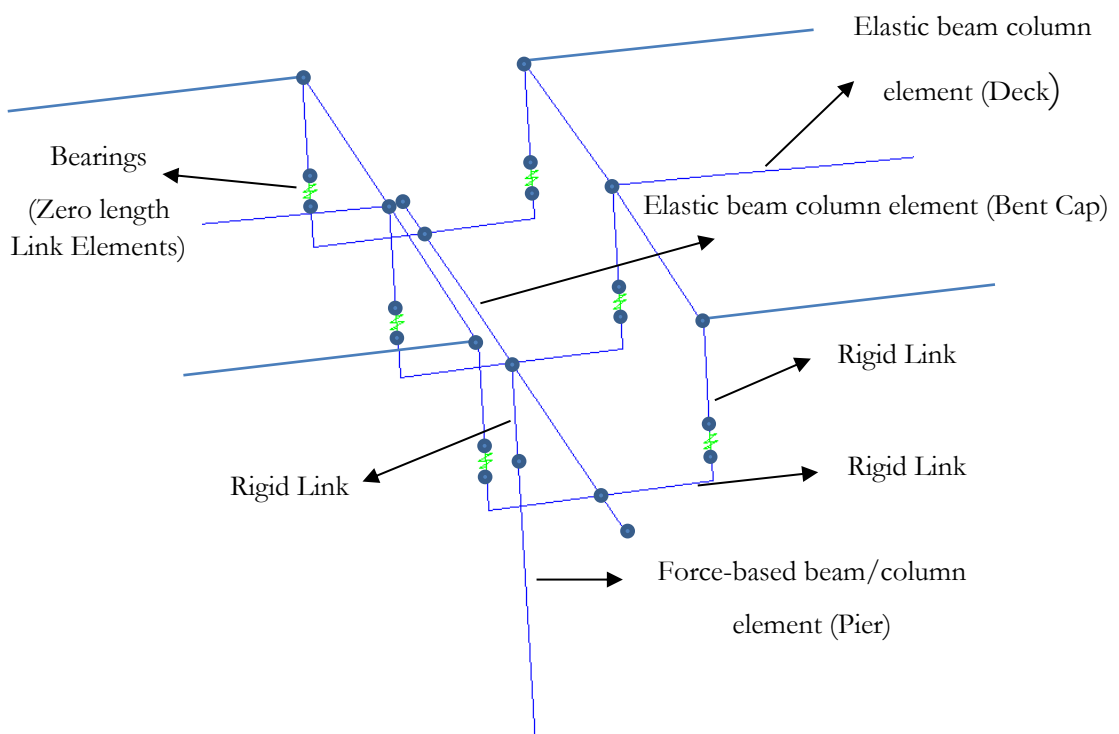


Figure 4.15. Schematic representation of the Deck-Column frame model.

4.7 ABUTMENT MODEL

A common type of abutments for this type of bridges has been implemented in the bridge under study. That is the inverted T-shaped abutment, in elevation and U-shaped, in plan, which also works as a retaining wall, with shallow foundation and orthogonal wing walls. The geometrical configurations of the abutment are given in Figure 4.16.

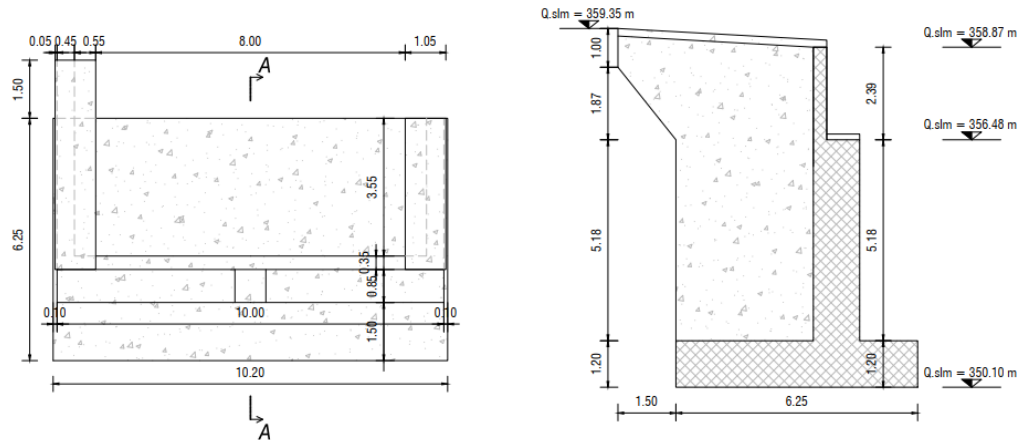


Figure 4.16. Abutment geometrical configuration from technical drawings

Abutment wall and its interaction with backfill soil can be modelled in accordance with SDC 2010 – 2019 (CALTRANS), depicted schematically in Figure 4.17. This proposed numerical modelling approach can be adopted in both longitudinal and transversal direction. However, the abutment in the numerical modelling of the structure was modelled with just an elastic beam/column frame element, using some approximate cross-section dimensions (1m x 9m) and a height of 6.55m, without including the backfill soil response.

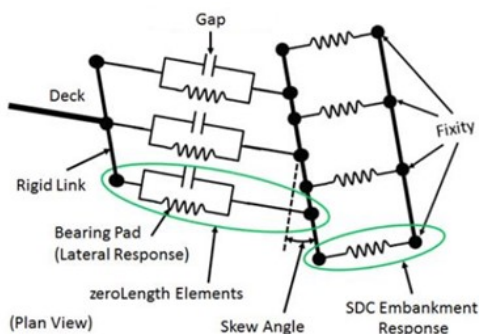


Figure 4.17. SDC 2010-2019 abutment model [Caltrans, 2019].

4.8 LOADS AND MASSES

The dead and superimposed dead loads can be applied on elements as uniformly distributed loads or point loads. Likewise, the seismic mass can be applied in the same manner as uniformly distributed or point mass. The masses in the numerical model were lumped at the end nodes of the elements, so that it would be possible to obtain the modal participation factors in the code. Similarly, the loads were applied as point loads. Note that results differ insignificantly when uniformly distributed loading is used. Following are the weights of the most relevant elements of the bridge.

Table 4.6. Unit and distributed weights in the structure.

Reinforced Concrete Unit Weight	25 kN/m ³
Concrete Unit Weight	24 kN/m ³
Weight of Asphalt	3.6kN/m ² → 31 kN/m
Weight of Side Walks	3.75 kN/m ² → 7.8 kN/m
Weight of Barriers	1 kN/m
Total Superimposed Dead Load	39.8 kN/m
Weight of Diaphragm Beams	164 kN

4.9 PUSHOVER ANALYSIS OF PIERS

Pushover analysis was carried out for each pier individually. It was observed that most of the piers fail globally at about 3% drift. Since the piers consist of two sections, also the pushover curve for each individual column element of the pier are presented. As expected, the partial column elements comprising the piers exhibit a higher drift capacity (Figure 4.20).

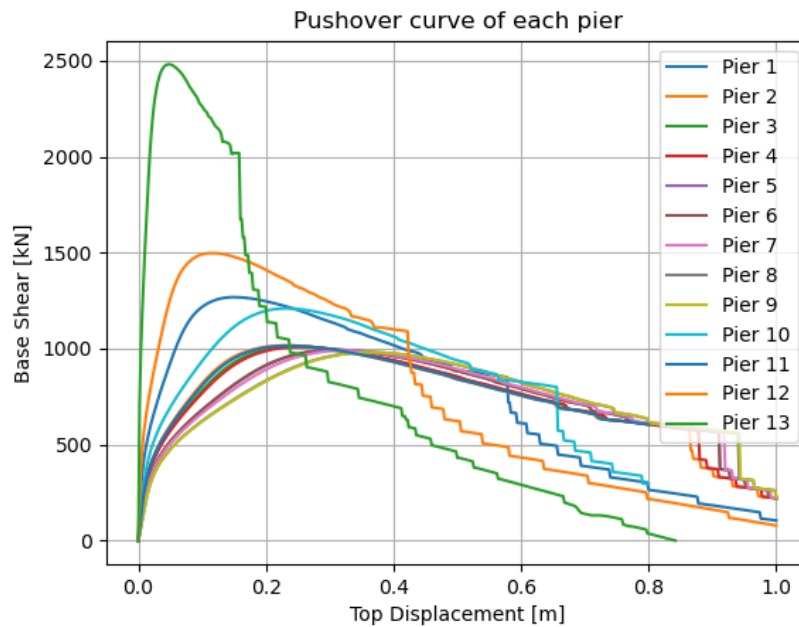


Figure 4.18. Pushover curve of the Piers measuring the top displacement

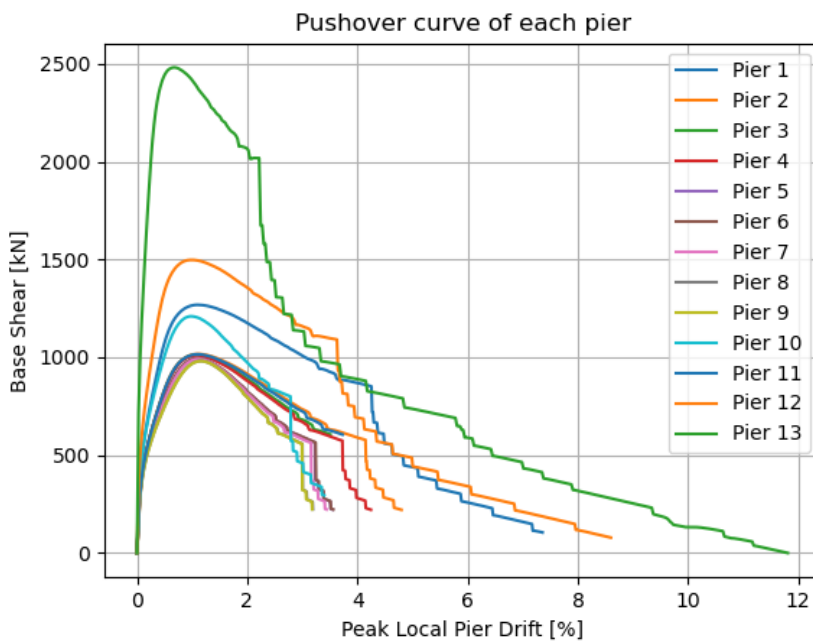


Figure 4.19. Pushover curve of the Piers measuring the Pier Drift ratio

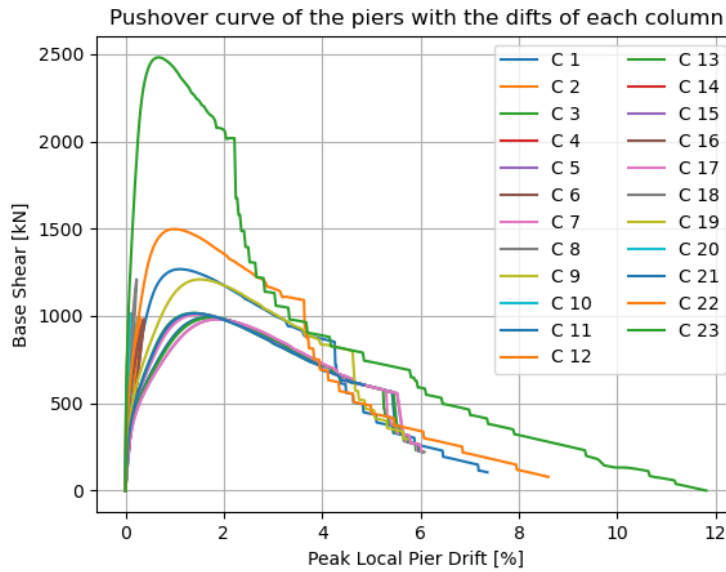


Figure 4.20. Pushover curve of the Piers, but depicted are the base shears and drifts of each individual column element comprising the Piers

The numbering order in Figure 4.20 goes from the lower column of the leftmost pier to the upper column of the rightmost pier, when looking at the longitudinal profile of the bridge shown in Figure 3.5.

4.10 SHEAR STRENGTH OF PIERS

The shear strength of the piers was calculated in each step of the pushover analysis, taking into account its interaction with flexural degradation, using the modified UCSD model [Kowalsky & Priestley, 2000]. These calculations were performed, in order check if there is a possible shear failure in the piers before the flexural one, because in the models (since fibre elements were used) only the flexural behaviour of the piers was considered.

The shear capacity of a column is given from the contribution of three separate components:

$$V_A = V_s + V_p + V_c \quad (4.1)$$

where, V_s : represents the shear capacity attributed to the steel truss mechanism

V_p : represents the shear capacity attributed to the axial load

V_c : represents the shear capacity attributed to the concrete shear resisting mechanism

Truss Mechanism

A revised truss component of the shear resistance, provided by the spiral or hoop reinforcement in a circular section is given as:

$$V_{sga} = \frac{\pi}{2} A_{sp} f_y \frac{D - c - cov}{s} \cot(\theta) \quad (4.2)$$

A typical value can be assumed for neutral axis depth, $c = 0.3D$ where D is the diameter of the column or $c=0.2 + 0.65P/(f_c' \cdot A_g)$. Otherwise, the neutral axis depth can be calculated as follows at each analysis step, since it cannot be obtained directly from OpenSeesPy:

$$c = D \frac{\varepsilon_c}{\varepsilon_c + \varepsilon_t} \quad (4.3)$$

where, ε_c is the strain of upper most compression fibre, and ε_t is the strain at lower most tension fibre. The angle of inclination between the shear cracks and the vertical column axis (θ) was assumed to be 30° .

Concrete Mechanism

The concrete mechanism strength of the revised model is given as:

$$V_c = \alpha \beta \gamma \sqrt{f'_c} (0.8A_g) \quad (4.4)$$

The α factor accounts essentially for the aspect ratio and is given as:

$$1 \leq \alpha = 3 - \frac{M}{V \cdot D} \leq 1.5 \quad (4.5)$$

The factor β is a modifier that accounts for the longitudinal steel ratio and is given as:

$$\beta = 0.5 + 20\rho_l \leq 1 \quad (4.6)$$

The γ factor represents the reduction in strength of the concrete shear resisting mechanism with increasing ductility and is given in the figure and equation below.

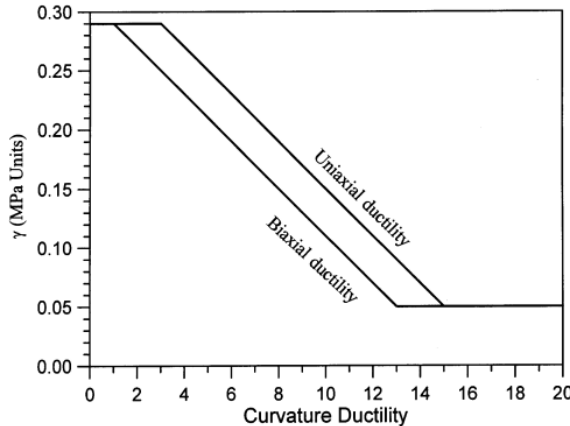


Figure 4.21. γ factor as a function of curvature ductility – revised UCSD assessment model

The case of uniaxial ductility was assumed for the pushover analysis, hence:

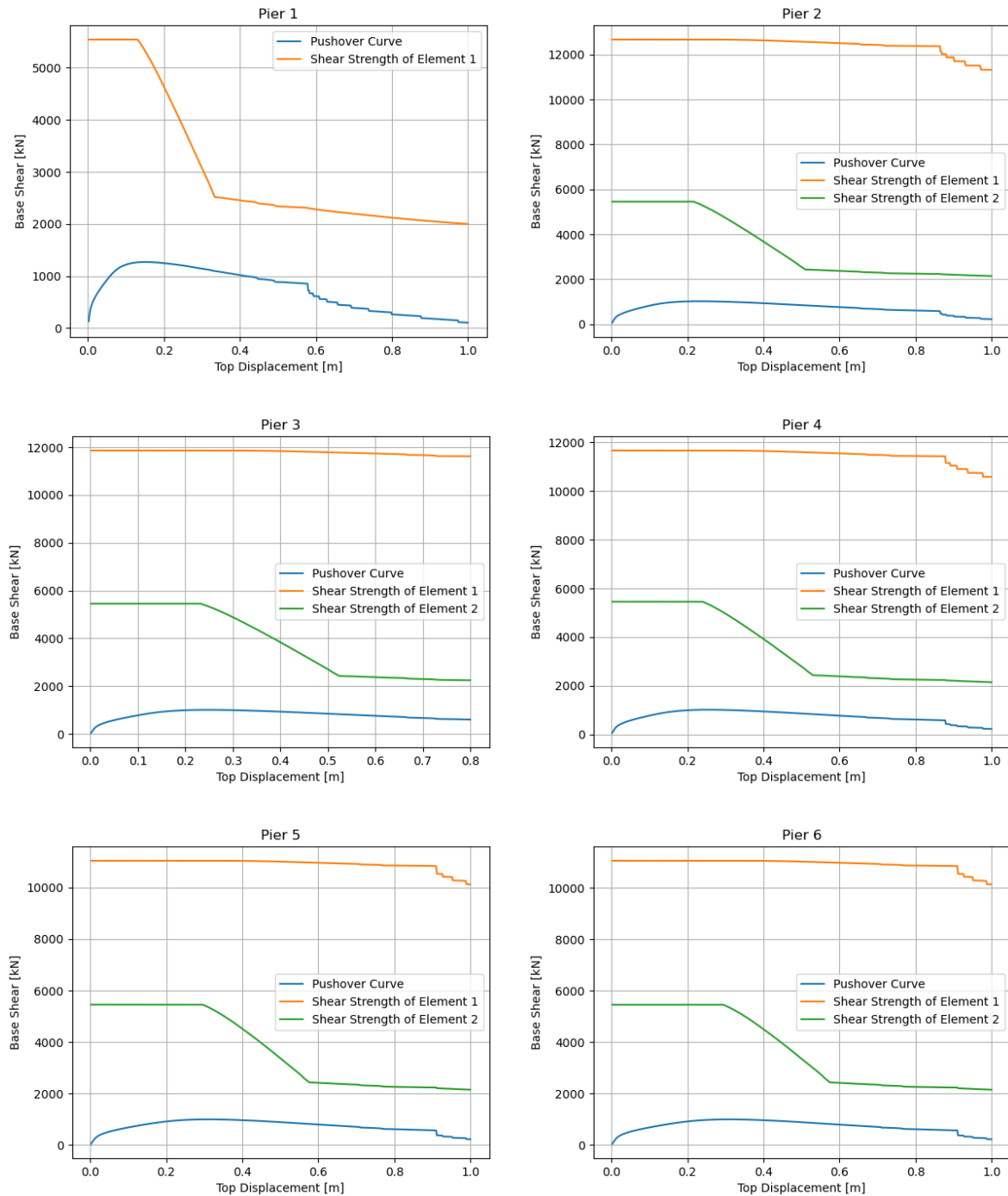
$$0.05 \leq \gamma = -0.02 \cdot \mu_\varphi + 0.35 \leq 0.29 \quad (4.7)$$

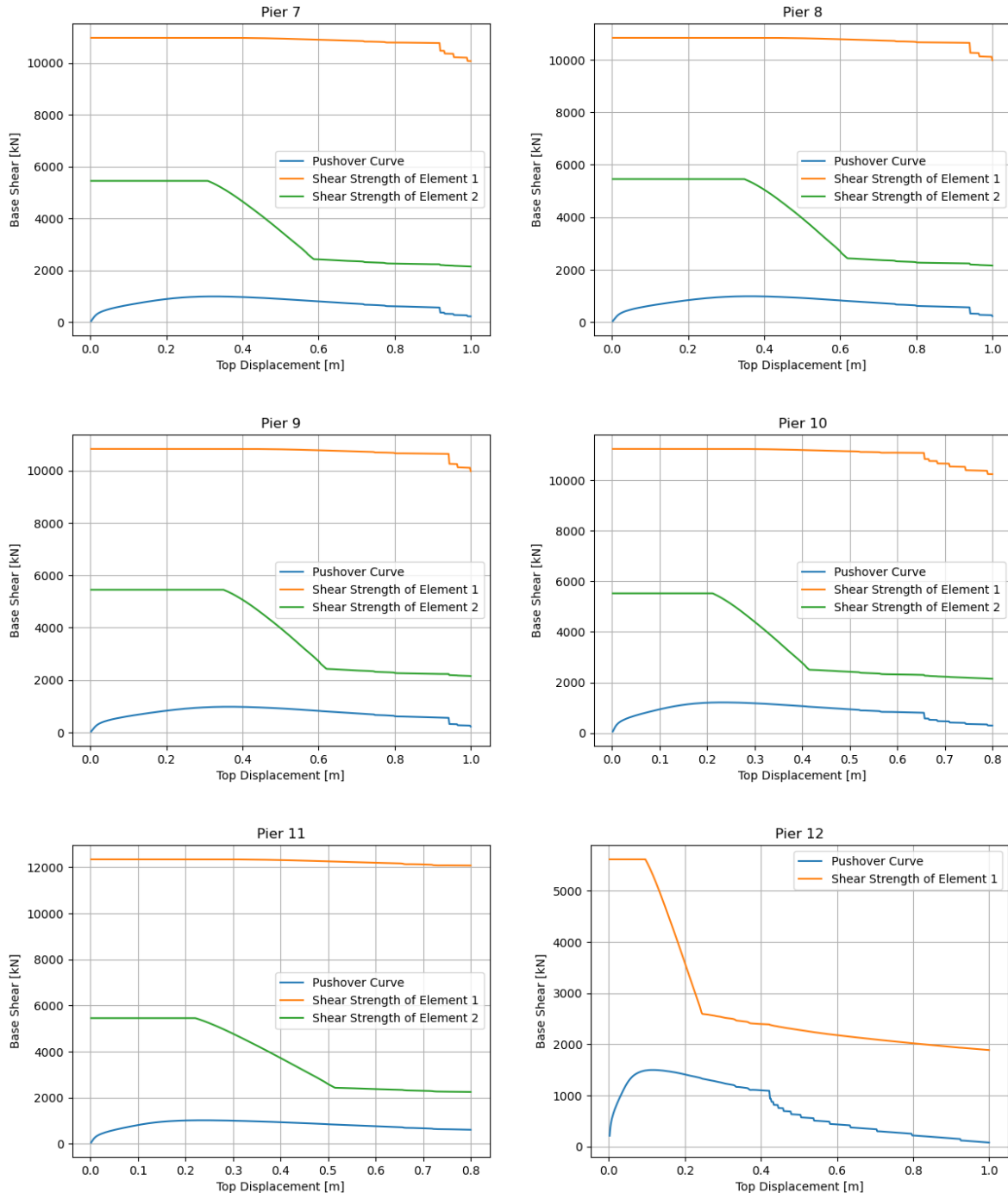
Axial Load Component

The shear strength enhancement provided by the axial load is given as:

$$V_p = \begin{cases} P \frac{(D - c)}{2L}, & P > 0 \\ 0, & P < 0 \end{cases} \quad (4.8)$$

Following are the results of the shear degradation of each pier superimposed by its pushover curve.





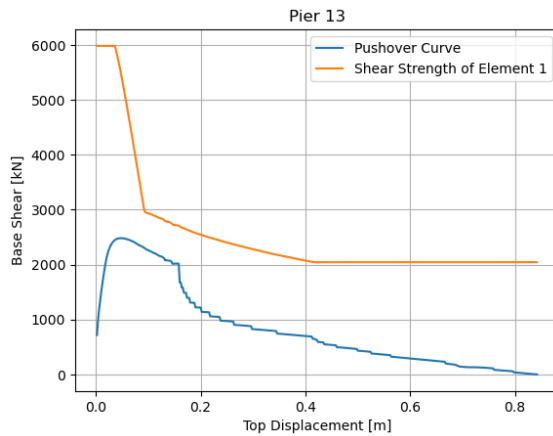


Figure 4.22. Comparison of the Shear Strength degradation with the Pushover Curves, using the modified UCSD model [Kowalsky & Priestley, 2000].

The evaluation showed that shear strength always exceeds the shear action in the critical sections of pier, hence there is no need for explicit modelling of shear degradation in the numerical model of the bridge. In order to capture strain and stress localizations due to the abrupt change in pier section, more advanced numerical modelling approaches are required. Likewise, modified compression field theory (MCFT) can be used to estimate the shear strength even more accurately.

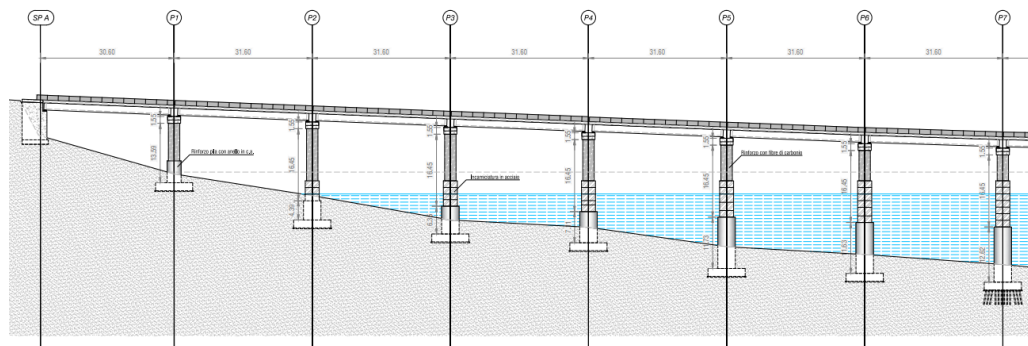
5. Description of the interventions performed in the bridge

The main reasons for the retrofit were the cracks found in various areas of the bridge (i.e. abutments, deck near the support, piers) and particularly in pier 10. Moreover, the deterioration in the metallic bearing was evident. These problems were due to time-dependent effects and to minor earthquakes suffered by the bridge. Finite element analyses found problems also due to torsion-shear-flexure interaction.

The fact that the bridge is located above a dam with drinkable water limited the intervention options and their corresponding construction process, as it was crucial to avoid any contamination of the water during and after the works.

Various intervention operations were performed in the bridge structure, but the main ones considered were the following: (a) the deck was made continuous, meaning that all the internal forces can be transferred from one deck to another (full connection), (b) the metallic bearings were replaced with friction pendulum isolators and (c) the piers were strengthened with concrete, steel and carbon-fibre jacketing.

Concrete jacketing was introduced in the base of the first and last pier, while steel jacketing was inserted in the base of the upper portion of the remaining piers. Above the aforementioned jackets, the remaining part of the piers was wrapped with carbon-fibre jackets. All the pier jackets and their position are depicted in Figure 5.1.



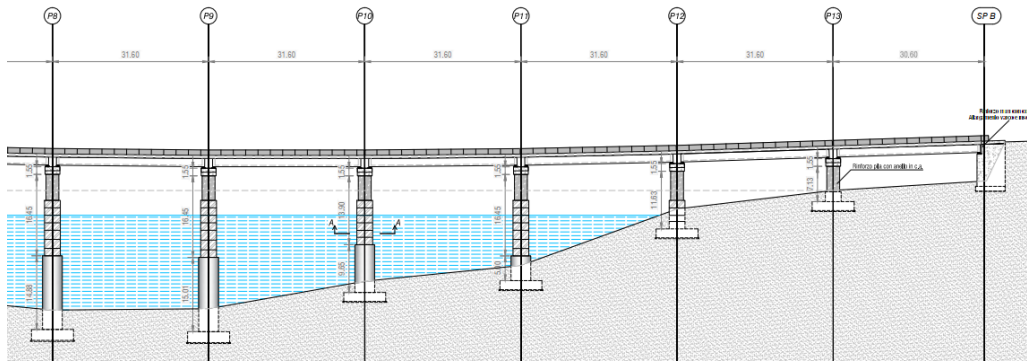


Figure 5.1. Schematic representation of the strengthening interventions in the piers of the bridge. (from technical drawings)

5.1 REPLACEMENT OF BEARING DEVICES WITH FRICTION PENDULUM ISOLATORS

The bridge under study includes 84 support devices, 6 corresponding to each pile and 3 corresponding to each deck support. These devices have different constraint properties in the longitudinal and transversal directions, as shown previously in Table 4.5. One of the interventions on the bridge was the replacement of these 84 bearings, with friction pendulum (FP) isolation devices with a single surface of curvature.

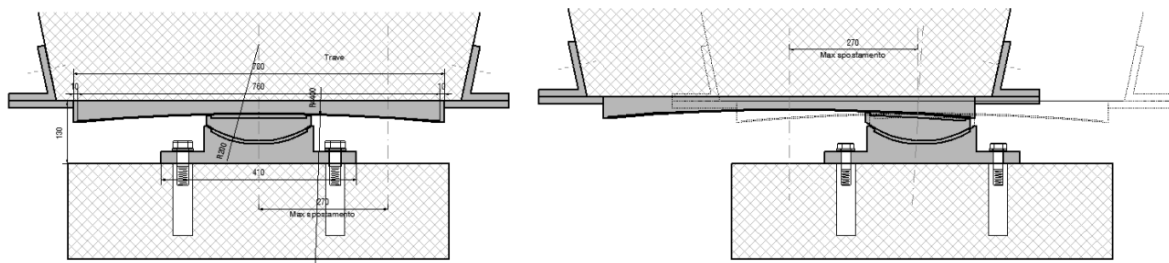


Figure 5.2. Schematic representation of the isolator design in undeformed configuration (left) and at maximum displacement (right)

This intervention required the deck to be lifted, the demolition and extraction of the existing bearings, the reconstruction and installation of the new devices according to the project specifications.

The lifting operations of the deck were carried out by positioning the jacks below the reinforced concrete diaphragm beam. The jacks were connected to three independent

hydraulic routes, so that they would be able to carry out a uniform lifting of the deck without introducing distortions. Each deck was lifted off of both end supports simultaneously, in order to avoid possible distortion and subsequently damage in the deck structure.

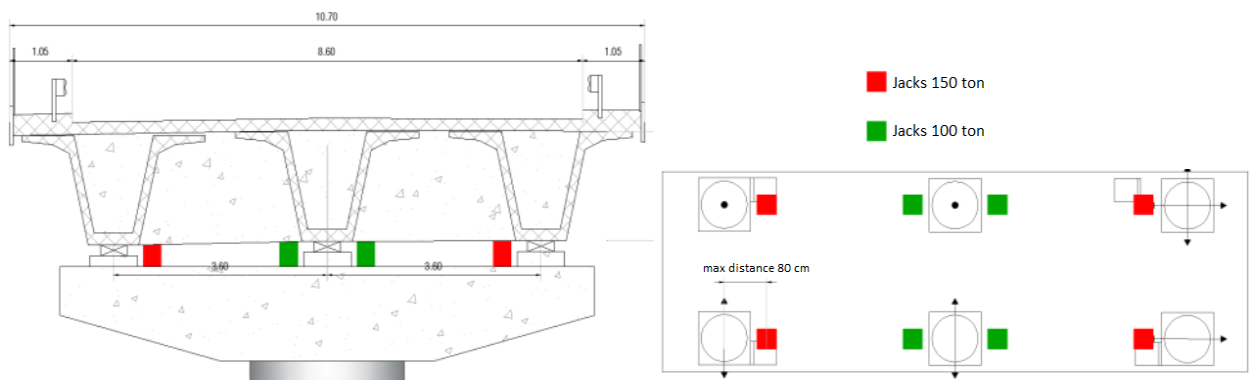


Figure 5.3. Details of deck lifting

The new support devices were then put in place and built into the structure.

5.2 STEEL JACKETING

Steel jacketing has been widely used in California as the major retrofit technique for bridge columns, with several hundred bridges retrofitted by 1994. During the 1994 Northridge earthquake, some 50 bridges with steel-jacketed columns were subjected to peak ground acceleration of 0.3g or higher, with none of them suffering damage to columns that required subsequent remedial work [Priestley, Seible, & Calvi, 1996].

This column retrofitting technique was originally developed for circular columns. Two half shells of steel plate are usually, rolled to a radius 12.5 to 25mm larger than the column radius, are positioned over the area to be retrofitted and are site-welded (or bolted in this case) up the vertical and horizontal seams to provide a continuous tube with a small annular gap around the column. This gap is grouted with cement grout, after flushing with water. Special rebar connectors are put in place, connecting the existing pier with the cement grout, in order to ensure a better connection. Typically, a space of about 50 mm is provided between the steel jacket and any supporting element in the ends (footing or cap beam), to avoid the possibility of the jacket acting as compression longitudinal reinforcement by bearing against the supporting member at large drift angles. This is to avoid excessive flexural strength enhancement of the plastic hinge region, which could result in increases in moments and shears in footings/cap beams under seismic response. In this case, below the jacket is the lower enlarged pier section.

The jackets main effect is the passive confinement of concrete, by inducing lateral confining stress in the concrete, as a flexible restraint, as the compressed concrete attempts to expand laterally as a function of high axial compression strains, or as the tensed concrete attempts to expand laterally as a function of dilatation of lap splices under incipient splice failure. The hoops together with the steel jackets contribute to the final level of confinement induced to the section.

Jacketing can also effectively resist to the lateral column dilatation associated with the development of diagonal shear cracks. In both cases (confinement of flexural hinges or potential shear failures) the jacket can be considered equivalent to continuous hoop reinforcement. Figure 5.4 shows some of the details of the jacket.

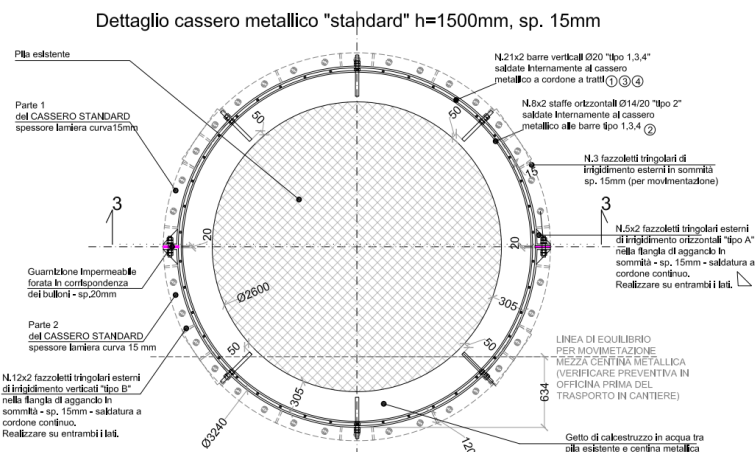


Figure 5.4. Cross section of a column retrofitted with steel jacketing (from technical drawings).

5.3 CONCRETE JACKETING

Concrete jacketing is the addition of a relatively thick layer of reinforced in the form of jacket around the column, which can be used to enhance flexural strength, ductility and shear strength of columns. This technique has been used more frequently for building columns, rather than for bridge columns. By inserting the longitudinal reinforcement of the jacket into the footing with sufficient anchorage length to develop its strength, the column flexural strength can be enhanced, although this must generally be accompanied by footing (or supporting member) retrofit measures to enhance footing flexural and shear

strength sufficiently to ensure that plastic hinge develops in the column, following the capacity design principles.

Enhanced confinement of circular columns is easy to achieve, through the use of closely-spaced hoops or spirals of small pitch. Circular or elliptical jacket, results in a much more effective confinement, than a rectangular one. Some details of the concrete jacket implementation in a rectangular column are shown in Figure 5.5.

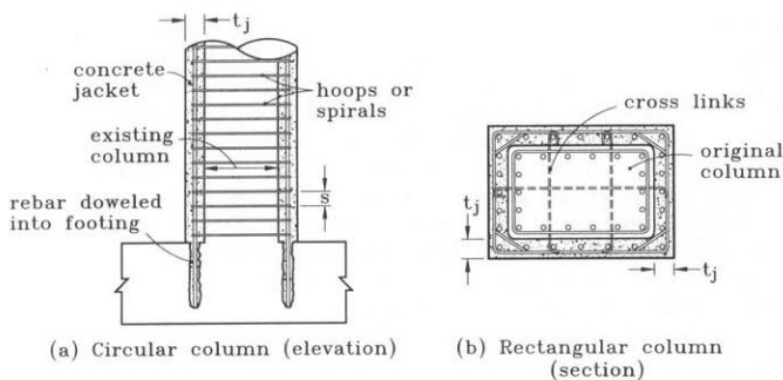


Figure 5.5. Confinement of columns by concrete jacketing. [Priestley, Seible, & Calvi, 1996]

The cross section of the concrete jacketing introduced in the bridge under study is depicted in Figure 5.6.

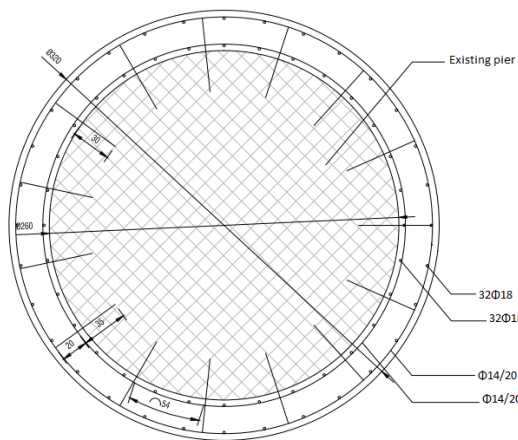


Figure 5.6. Cross section of a column retrofitted with concrete jacketing. Reinforcement information.

5.4 COMPOSITE-MATERIALS JACKETING

The effectiveness of column retrofit using jackets of composite materials such as fiberglass, carbon fibre and kevlar, generally bonded together and to the column with epoxy, occupies a significant number of researchers.

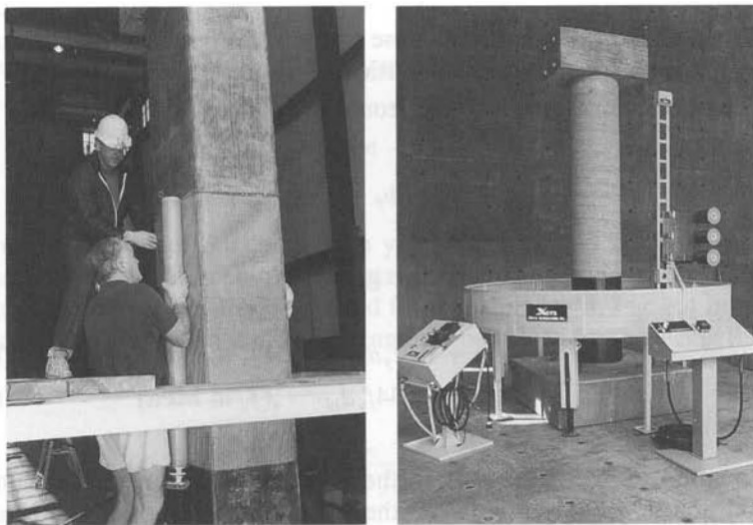


Figure 5.7. Retrofitting with composite-materials jackets. (a) High-strength fiberglass and epoxy: Hand-layup; (b) Carbon fibre and epoxy: machine winding. [Priestley, Seible, & Calvi, 1996]

Comparing carbon fibres with fiberglass, carbon fibres usually have lesser thickness than the cheaper but more flexible and weaker fiberglass jacket, because of their greater strength and stiffness. Fiberglass jacketing found more applications in building columns than in bridges.

In both cases, the techniques are most suitable for circular columns, where the jacket is utmost effective. However, a reasonable enhancement of ductility can be achieved with rectangular carbon fibre or fiberglass-epoxy jackets on rectangular columns, if applied properly.

Retrofits with composite-material jackets to improve ductility exhibit a more efficient confinement effectiveness than those with steel jackets, as indicated from tests on circular columns. It is thought that this is a result of the elastic nature of the jacket material. With

a steel jacket, yield under hoop tension may occur early in seismic response. On unloading and, in extend, on cyclic loading, residual plastic strains remain in the jacket, reducing its effectiveness in each successive cycle of response, and requiring increased hoop strains per cycle. With materials such as fibre glass and carbon fibre, which have essentially linear stress-strain characteristics up to failure, there is no cumulative damage, and successive cycles to the same displacement result in constant rather increasing hoop strain. Thus, the experimentally derived expressions for composite-material jackets indicate greater efficiency than for steel jackets.

6. Numerical Modelling of the Retrofitted Bridge Structure

Concrete columns oftentimes suffer from limited flexural ductility, shear strength and flexural strength, due to insufficient amount and/or detailing of longitudinal and/or transversal reinforcement, insufficient lap splices in critical regions or premature termination of longitudinal reinforcement.

There are several of column retrofitting techniques that have been developed and tested, with a large number being implemented in actual retrofit design of bridges and buildings. Some of the column retrofit techniques include steel jacketing, active confinement by wire prestressing, jackets from composite materials (i.e. fiberglass, carbon fibre, or other fibres in an epoxy matrix) and jacketing with reinforced concrete. The most common retrofit technique implemented in practice is steel jacketing, with reinforced concrete jackets and composite material jackets occupying a smaller share of the market. Three of the four stated column retrofit techniques were used in the bridge under study, and are discussed in the following.

Additionally, isolators were inserted in the structure, replacing the metallic bearings, in order to relieve the piers from excessive deformations and to dissipate the input earthquake energy. In this case study, friction pendulum isolators were selected and studied further below.

6.1 FRICTION PENDULUM ISOLATORS

The bearing is characterized by coupled (since the model is 3D) friction properties (with post-yield stiffening due to concave sliding surface) for the shear deformations. Force-deformation behaviours are defined by UniaxialMaterials in the remaining four directions (P , T , M_y , M_z). To capture the uplift behaviour of the bearing, the UniaxialMaterial in the axial direction was assigned in such a way that there is no-tension behaviour.

To avoid the introduction of artificial viscous damping in the isolation system (i.e. ‘damping leakage in the isolation system’), the bearing element did not contribute to the Rayleigh damping by default.

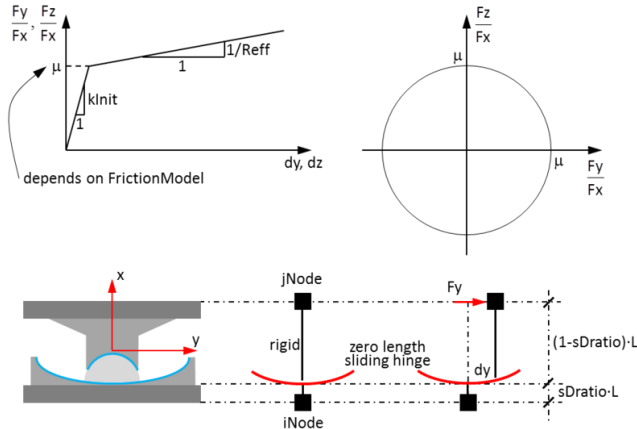


Figure 6.1. Properties of single Friction Pendulum (FP) bearing element
[OpenSees, 2006]

The parameters used as an input to the model the isolator devices are given in the following.

Average axial load imposed on one isolator: $N_{sd} = \frac{5150\text{kN per pier cap}}{6 \text{ isolator per support}} = 858\text{kN}$

Equivalent radius of curvature: $R = 4.6\text{m}$

Friction coefficient: $\mu = 0.07$

Isolator post-activation stiffness: $K_r = \frac{N_{sd}}{R} = 186.59\text{ kN/m}$

Initial (pre-activation) isolator stiffness: $K_{ini} = \frac{N_{sd}}{R} \cdot 100 = 18659\text{ kN/m}$

Isolator post-activation period: $T = 2\pi \sqrt{\frac{R}{g}} = 4.303\text{sec}$

6.2 PIER STRENGTHENING INTERVENTIONS

Columns that are not properly confined (i.e. insufficient amount of transverse reinforcement), will exhibit reduced ductility capacity and reduced bending moment capacity, especially in the plastic hinge zone, and that is of primary concern. This problem can be oftentimes eliminated by introducing jackets around the column, in order to improve the confinement for flexural ductility enhancement.

Essentially, the column jacketing modifies the concrete constitutive law of the section, in that it increases the confinement coefficient, which in turn increases the concrete strength and ultimate strain. Also, it increases the buckling resistance of the longitudinal reinforcement, but that has not been taken into account in the modelling.

6.2.1 Steel jackets

The effective volumetric ratio of confining steel for a circular steel jacket of diameter D (centreline to centreline) is given as:

$$\rho_s = \frac{4t_j}{D} = \frac{4 \cdot 15\text{mm}}{3225\text{mm}} = 0.01860465 \quad (6.1)$$

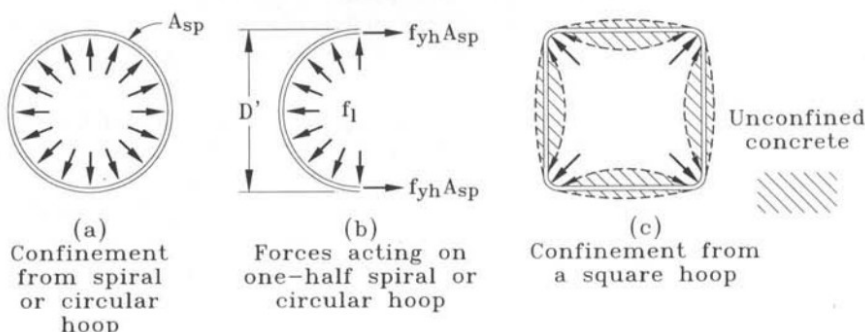


Figure 6.2. Confinement of concrete by circular and square hoops [Seismic Design and Retrofit of Bridges, Priestley, Seible, Calvi]

The maximum effective lateral pressure f_l that can be induced in the concrete occurs when the steel jacket with thickness t_j is stressed to its yield strength f_{yj} . Hence, imposing equilibrium to the free body diagram of Figure 6.2, the resulting expression is:

$$f_l = \frac{2f_{yj}t_j}{D} = \frac{2 \cdot 355\text{MPa} \cdot 15\text{mm}}{3225\text{mm}} = 3.3023\text{MPa} \quad (6.2)$$

The ratio of peak concrete confined stress, f'_{cc} , to the peak concrete unconfined stress, f'_c , is given as follows:

$$\begin{aligned}\frac{f'_{cc}}{f'_c} &= 2.254 \sqrt{1 + \frac{7.94f'_l}{f'_c} - \frac{2f'_l}{f'_c}} - 1.254 \\ &= 2.254 \sqrt{1 + \frac{7.94 \cdot 3.1372MPa}{25MPa} - \frac{2 \cdot 3.1372MPa}{25MPa}} \\ &- 1.254 = 1.67977\end{aligned}\tag{6.3}$$

Note that the ratio indicatively given above, refers to the unconfined concrete in the cover of the unretrofitted section.

The effective lateral confining stress, f'_l , is related, for circular sections to the average confining stress of Equation (6.2) by the following expression:

$$f'_l = K_e f_l = 0.95 \cdot 3.3023MPa = 3.1372MPa\tag{6.4}$$

where, K_e is the confinement effectiveness coefficient, representing the ratio of the minimum area of effectively confined core to the nominal core area bounded by the centreline of the peripheral hoops or jacket. A typical value of K_e for circular sections, which was actually used, is 0.95.

The compression strength of the confined concrete f'_{cc} , given in Equation (6.3), is expressed graphically for convenience in Figure 6.3, as a function of ρ_s and the ratio f_{yj}/f'_c . From the aforementioned graph, the validity of the previous calculations can be checked.

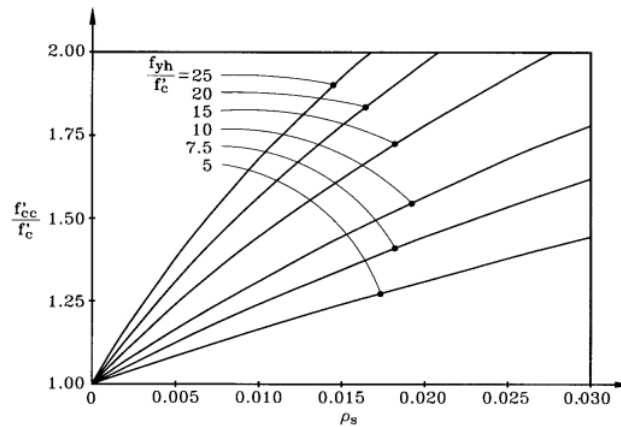


Figure 6.3. Enhancement of concrete compression strength by confinement
[Seismic Design and Retrofit of Bridges, Priestley, Seible, Calvi]

6.2.2 Concrete Jackets

The calculation of the increase of confinement, given by the concrete jacket to the column, follows the same procedure as the corresponding effect given by the transverse reinforcement in new columns. The volumetric ratio of the confining steel is given as follows.

$$\rho_s = \frac{4A_h}{D's} = \frac{4 \cdot 153.94 \text{ mm}^2}{3100 \text{ mm} \cdot 200 \text{ mm}} + \frac{4 \cdot 153.94 \text{ mm}^2}{2700 \text{ mm} \cdot 200 \text{ mm}} = 0.001999 \quad (6.5)$$

where, D' is the diameter of the hoop or spiral provided in the concrete jacket, at vertical spacing s , which has a bar area of A_h .

The maximum effective lateral pressure f_l , due to the inner and outer hoops separately, is given as:

$$f_{l,outer} = \frac{2f_{yh}A_{sp}}{D's} = \frac{2 \cdot 450 \text{ MPa} \cdot 153.94 \text{ mm}^2}{3100 \text{ mm} \cdot 200 \text{ mm}} = 223.46 \text{ kPa} \quad (6.6)$$

$$f_{l,inner} = \frac{2f_{yh}A_{sp}}{D's} = \frac{2 \cdot 450 \text{ MPa} \cdot 153.94 \text{ mm}^2}{2700 \text{ mm} \cdot 200 \text{ mm}} = 256.56 \text{ kPa}$$

The confinement effectiveness (K_e) was calculated from the previously stated Mander confinement model and was found to be $K_{e,outer} = 0.942$ and $K_{e,inner} = 0.934$

$$f'_l = K_{e,outer} f_{l,outer} + K_{e,inner} f_{l,inner} = 450.01 \text{ kPa} \quad (6.7)$$

The ratio of peak concrete confined stress, f'_{cc} , to the peak concrete unconfined stress, f'_c , is given as follows:

$$\frac{f'_{cc}}{f'_c} = 2.254 \sqrt{1 + \frac{7.94 f'_l}{f'_c}} - \frac{2 f'_l}{f'_c} - 1.254 = 1.1197 \quad (6.8)$$

6.2.3 Composite-Material Jackets

One layer of carbon-fibre *MapeWrap C UNI-AX 300* FRP sheet [MAPEI S.p.A., 2019] was used, for the wrapping of the piers.

The volumetric ratio of the confining FRP sheet for a circular column of diameter D is given as:

$$\rho_s = \frac{4t_j}{D} = \frac{4 \cdot 0.5 \text{ mm}}{2600 \text{ mm}} = 0.0002523 \quad (6.9)$$

The maximum effective lateral pressure f_l , is given as follows.

$$f_l = \frac{2f_{uj}t_j}{D} = \frac{2 \cdot 1492 \text{ MPa} \cdot 0.5 \text{ mm}}{2600 \text{ mm}} = 0.5738 \text{ MPa} \quad (6.10)$$

The effective lateral confining stress, f'_l , is given by the follow expression (for full confinement effectiveness, $K_e = 1$)

$$f'_l = K_e f_l = 1 \cdot 0.5738 \text{ MPa} = 0.5738 \text{ MPa}$$

where, t_j and f_{uj} is the thickness and ultimate stress of the jacket material.

The ratio of peak concrete confined stress, f'_{cc} , to the peak concrete unconfined stress, f'_c , is given as follows:

$$\frac{f'_{cc}}{f'_c} = 2.254 \sqrt{1 + \frac{7.94 f'_l}{f'_c}} - \frac{2 f'_l}{f'_c} - 1.254 \quad (6.11)$$

$$\frac{f'_{cc}}{f'_c} = 2.254 \sqrt{1 + \frac{7.94 \cdot 0.5738 \text{ MPa}}{25 \text{ MPa}}} - \frac{2 \cdot 0.5738 \text{ MPa}}{25 \text{ MPa}} - 1.254 = 1.1509$$

6.3 MOMENT-CURVATURE ANALYSES

According to the structural intervention drawings, the retrofit interventions in the piers are concentrated in the small section of the piers. Following is the moment curvature analyses the different retrofitted sections.

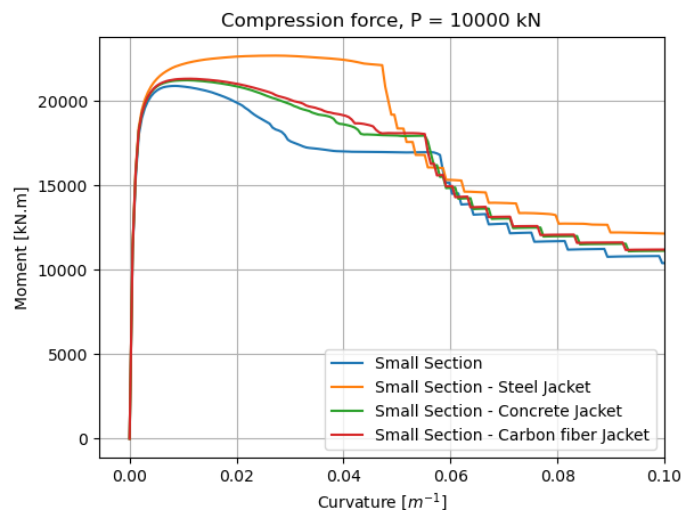


Figure 6.4. Moment-Curvature analysis of the different retrofit strategies of the small section of the piers. Compared also with the as-built section.

It can be perceived from Figure 6.4 that when the jackets were added, and the confinement of the concrete was increasing, the curvature ductility of the section was decreasing. This is happening because it's the steel rupture that controls the ultimate curvature of the section and by adding strength to the concrete, the ultimate curvature decreases. Nevertheless, the

post-peak behavior of the section was improved and there was a slight increase in the peak moment.

In order to check the accuracy of the above results, the M- φ analyses of the retrofitted sections were compared with the corresponding ones computed with SeismoStruct. The section with the reinforced concrete jacket was left out, as it was considered trivial.

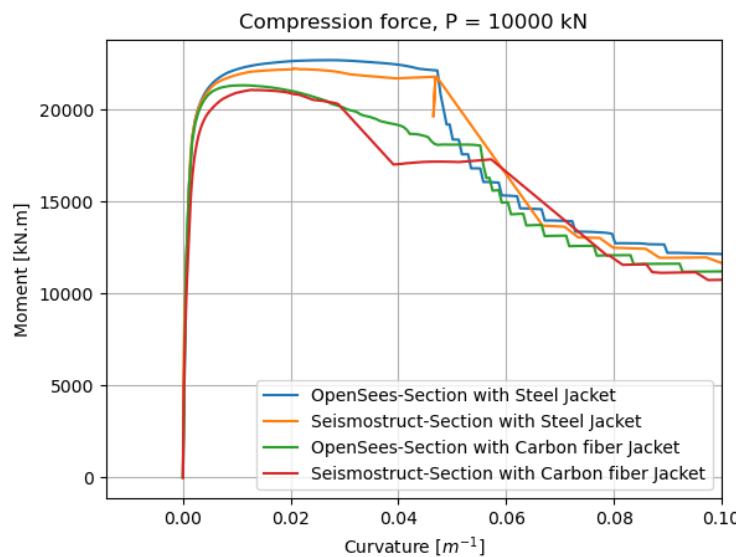


Figure 6.5. Comparison between OpenSeesPy and SeismoStruct of the section retrofitted with steel jacket and the section retrofitted with FRP jacket.

It can be seen that SeismoStruct predicted lower ultimate moments, but the general trend of the curves coincides pretty well. The two softwares yield acceptably close results, hence the modelling approach was deemed valid.

6.4 PUSHOVER ANALYSIS OF PIERS

Pushover analysis was carried out for each pier individually, in the same manner as for the as-built model. It was observed that most of the retrofitted piers fail at about 2.5% global drift. As expected, the column elements comprising the piers exhibit a higher drift capacity.

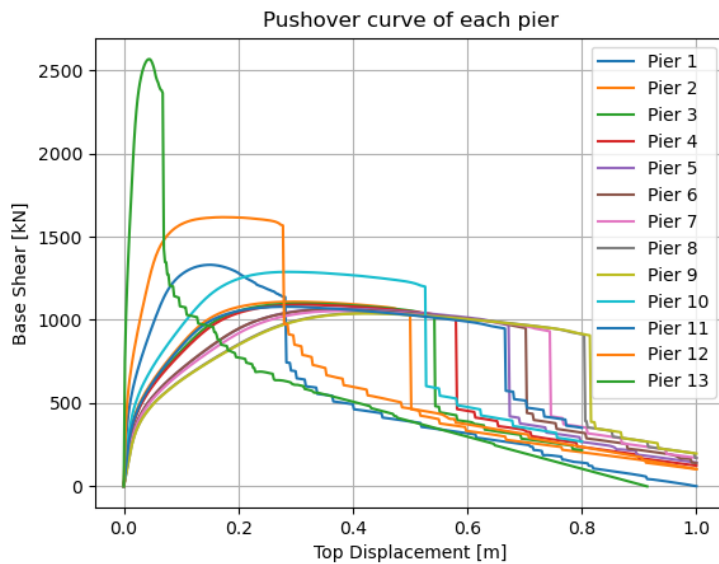


Figure 6.6. Pushover curves of the retrofitted Piers

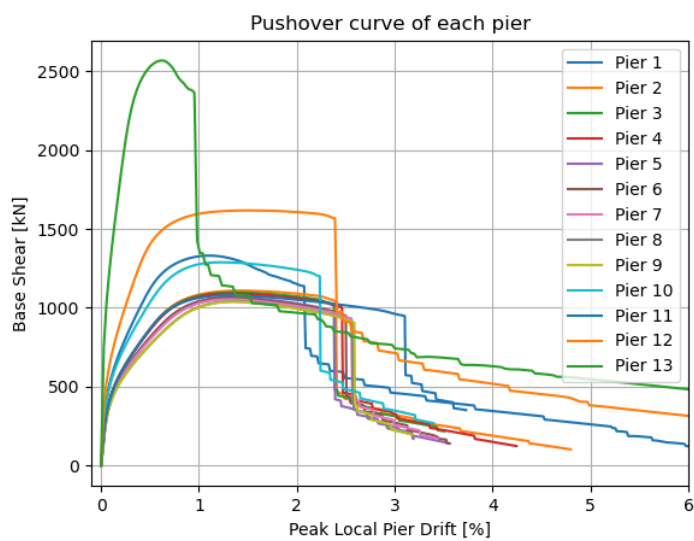


Figure 6.7. Pushover curves of the retrofitted Piers

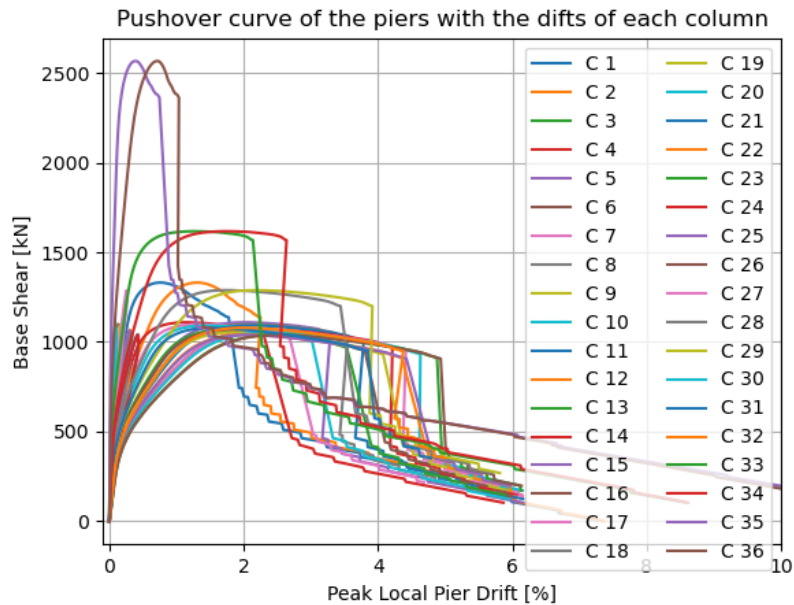
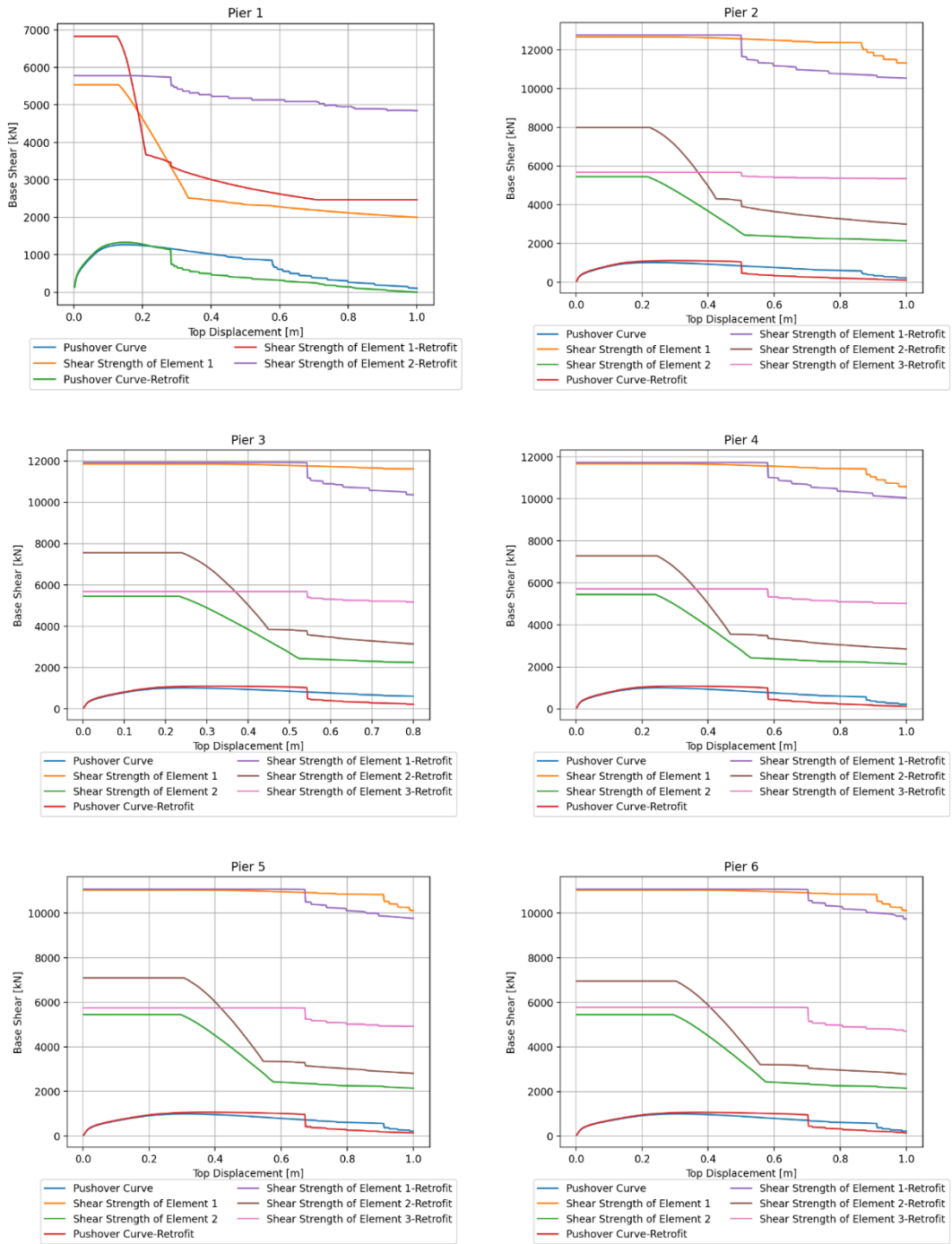
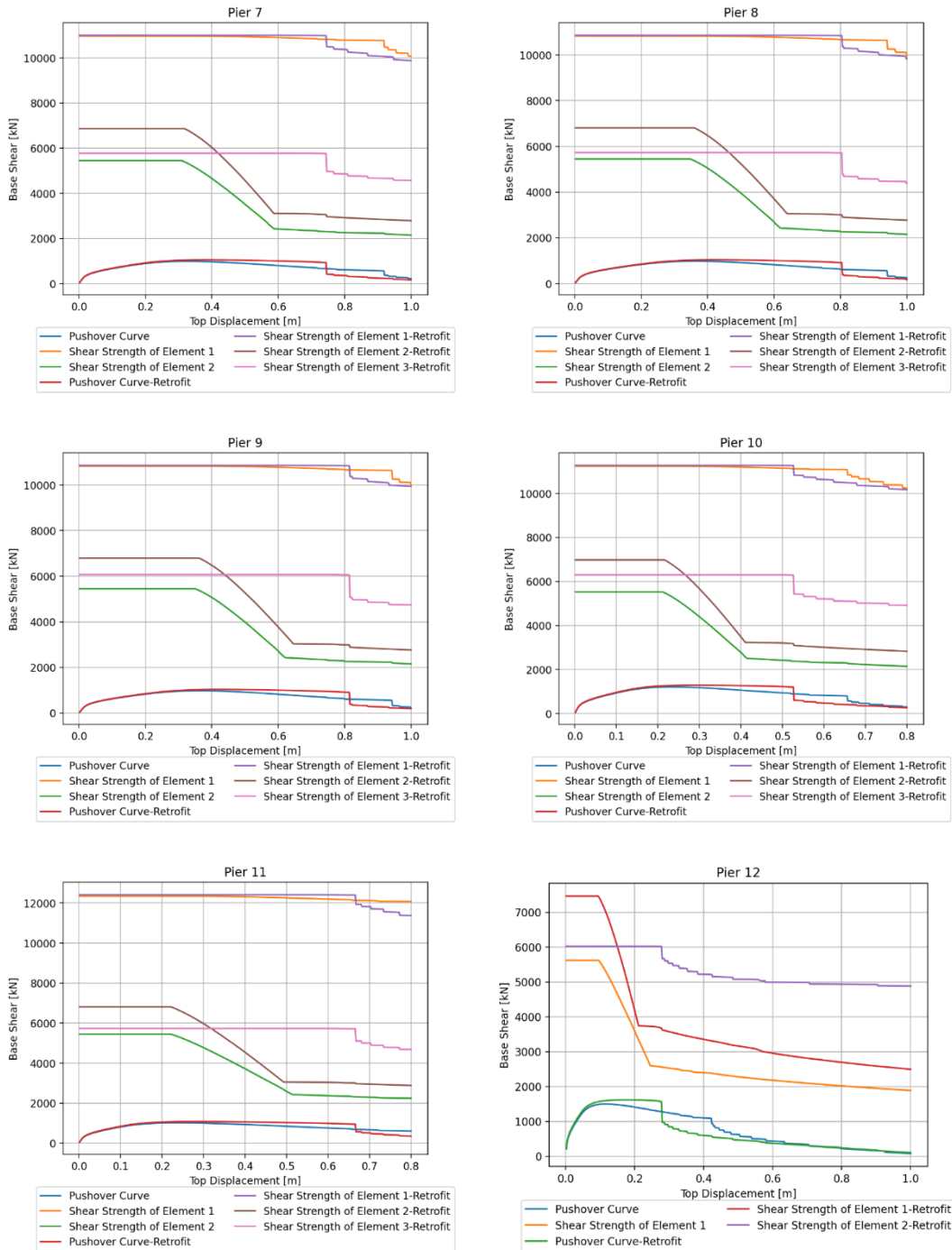


Figure 6.8. Monitoring of the response of the individual columns comprising the retrofitted piers, during the pushover of the Piers

6.5 SHEAR STRENGTH OF PIERS

The shear strength of the retrofitted piers, along with their pushover curves were calculated and compared with the ones of the as-build piers, as shown in the following graphs.





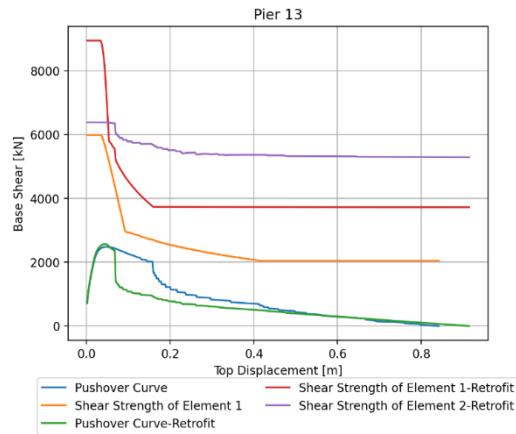


Figure 6.9. Shear strength degradation and Pushover curves of the retrofitted Piers, compared with the corresponding as-built Piers

It can be seen from the plots of Figure 6.9 that the shear strength of the elements after the retrofit was increased, not dramatically but slightly. This was due to the improved concrete mechanism component of shear strength. As mentioned in the M- φ analyses, it can be seen also here that the displacement ductility has decreased after the retrofit.

7. Direct Seismic Loss Assessment of the As-Built Bridge

7.1 SEISMIC HAZARD CHARACTERIZATION AND DISAGGREGATION

7.1.1 Choice of Intensity Measure

Intensity measures (IMs) serve as a connection between the seismic hazard and structural response. It is important to choose an appropriate IM that accurately describes the response of the structure at hand over the different intensity levels to be analyzed.

Average spectral acceleration (AvgSa) over a period range defined in Equation (7.1) was chosen as an appropriate IM for the scope of this study. In order to support this decision of IM used for the analyses, it should be stated that the structure doesn't have clearly dominant periods, in other words, the modal masses are relatively small even at the first periods, and higher mode effects can be very significant [O'Reilly, 2020]. A large number of modes has to be considered in order to achieve a satisfactory modal mass. AvgSa was defined as follows (calculating the geomean of several spectral accelerations):

$$\begin{aligned} \text{AvgSa} &= \left(\prod_{i=1}^N \text{Sa}(T_i) \right)^{1/N} \quad \text{where } T_i \in [T_n \text{ where } \sum MPy,x \approx 85\%} \\ &\quad = 0.16 \text{ sec}, 1.5T_1 \approx 2.34 \text{ sec}] \end{aligned} \quad (7.1)$$

After the model was built in OpenSeesPy (as described above), the modal properties were calculated and shown in Appendix A., in Table A.1.

The fact that modal mass participation factors are distributed through a large range of periods can be also seen in Figure 7.1.

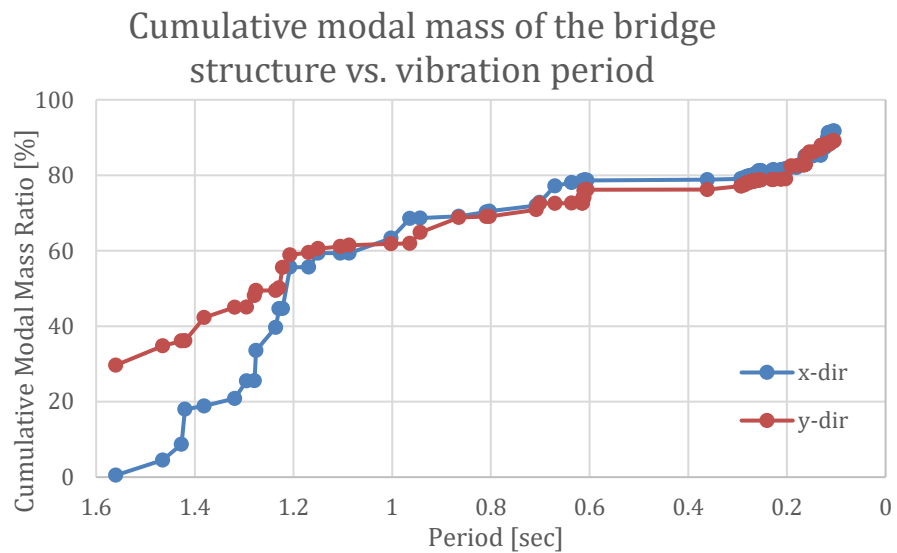


Figure 7.1. Cumulative modal mass of the bridge versus vibration period

Table 7.1. Selected period range for AvgSa^c

$[T_{85\%} - 1.5T_1]$	
T_{lower} [sec]	0.16
T_{upper} [sec]	2.36

7.1.2 Geotechnical Information

Some geotechnical information was available from the technical reports for the Cingoli site, given in Table 7.2.

Table 7.2. Soil Profile - Constant profile is assumed along the bridge length

Depth [m]	Thickness [m]	Vs [m/s]	Unit Weight [kN/m ³]
0.0	1.80	380.00	19.60
1.80	3.10	430.00	19.60
4.90	3.50	600.00	20.60
8.40	7.70	700.00	21.00
16.10	Bedrock Half-Space	900.00	-

^c The period spacing chosen was 0.1sec

The average shear wave velocity in the top 30m from the ground surface was computed in accordance with the following expression:

$$v_{s,30} = \frac{30}{\sum_{i=1,N} \frac{h_i}{v_i}} = 678 \text{ m/s} \quad (7.2)$$

Therefore, the soil can be classified as type B, according with EC8, as shown in Table 7.3.

Table 7.3. Ground types distinguished by Eurocode 8 and some of their corresponding parameters [EN 1998-1 2004].

Ground type	Description of stratigraphic profile	Parameters		
		V _{s,30} (m/s)	N _{SPT} (blows/30cm)	c _u (kPa)
A	Rock or other rock-like geological formation, including at most 5 m of weaker material at the surface.	> 800	-	-
B	Deposits of very dense sand, gravel, or very stiff clay, at least several tens of meters in thickness, characterized by a gradual increase of mechanical properties with depth.	360 – 800	> 50	> 250
C	Deep deposits of dense or medium-dense sand, gravel or stiff clay with thickness from several tens to many hundreds of meters.	180 - 360	15 – 50	70 - 250
D	Deposits of loose-to-medium cohesionless soil (with or without some soft cohesive layers), or of predominantly soft-to-firm cohesive soil.	< 180	< 15	< 70
E	A soil profile consisting of a surface alluvium layer with v _s values of type C or D and thickness varying between about 5 m and 20 m, underlain by stiffer material with v _s > 800 m/s.			
S ₁	Deposits consisting, or containing a layer at least 10 m thick, of soft clays/silts with a high plasticity index (PI > 40) and high water content	< 100 (indicative)	-	10-20

S ₂	Deposits of liquefiable soils, of sensitive clays, or any other soil profile not included in types A – E or S ₁			
----------------	--	--	--	--

However, as discussed in Section 7.1.3, a different site was chosen for the analyses (L'Aquila site). The average shear wave velocity $v_{s,30}$ of that site was chosen to be 300m/s (ground type C), just for academic purposes.

7.1.3 Seismic Hazard & Disaggregation

First, the seismic hazard was calculated for the actual site of the bridge (Cingoli site), but it was observed that the hazard at that site was low and consequently the risk of the bridge was found to be low. Hence, in order to get more interesting results for the purposes of academic exercise, the city of L'Aquila in central Italy was chosen as the site for the analyses, which has a more impactful seismic hazard.

The OpenQuake engine [GEM, 2020] was used to perform PSHA calculations with the SHARE source model (2013). The model includes area, fault and point sources, with uncertainty weights 0.5, 0.2 and 0.3, respectively, in the source model logic tree. A $V_{s,30}$ value of 678m/s for the Cingoli site and 300m/s for the L'Aquila site was assigned.

In order to keep the calculations simple - having in mind the conditional spectrum approach to be followed after - only one Ground Motion Prediction Equation (GMPE) was used in the PSHA logic tree, the one from Boore and Atkinson (2008) [Boore & Atkinson, 2008]. The motivation for selecting that GMPE was that it can give AvgSa at periods between 0.01s and 10s. Additionally it was derived by empirical regression of an extensive strong-motion database compiled by the PEER NGA project [Chiou, Darragh, Gregor, & Silva, 2008].

For the calculations with AvgSa, the correlations between spectral acceleration values at multiple periods were computed according to equations developed empirically from the NGA ground motion database [Baker & Jayaram, 2008]. The correlation function was also fitted over a period range of 0.01s to 10s.

Following is the hazard characterization of the Cingoli site. The hazard maps, hazard curves and the nine intensity levels are given in Figure 7.2, Figure 7.3 and Table 7.4, respectively.

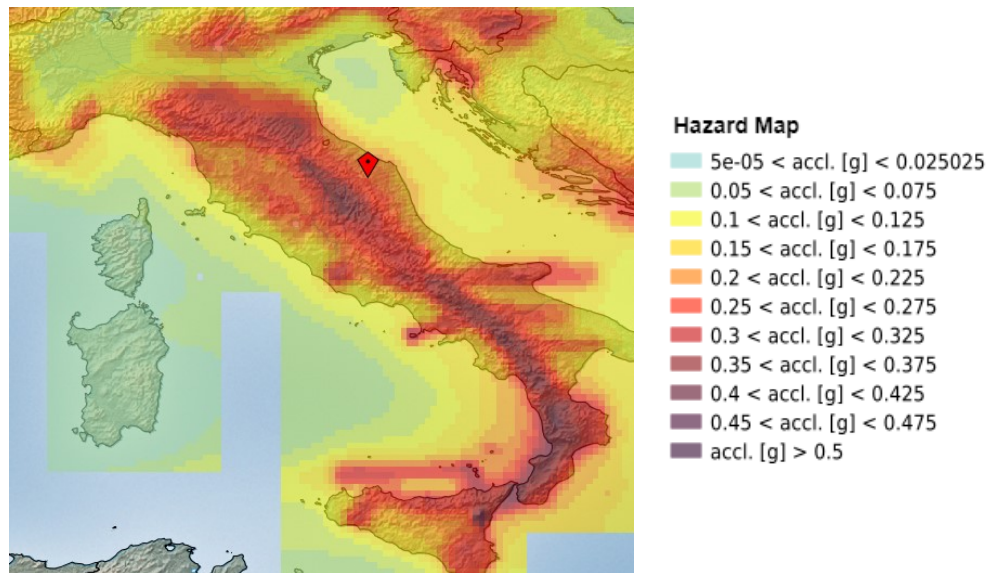


Figure 7.2. Location of the Cingoli site on the Italian hazard map of median PGA with 475 years return period on rock soil conditions. [European Facilities for Earthquake Hazard and Risk (EFEHR), 2017]

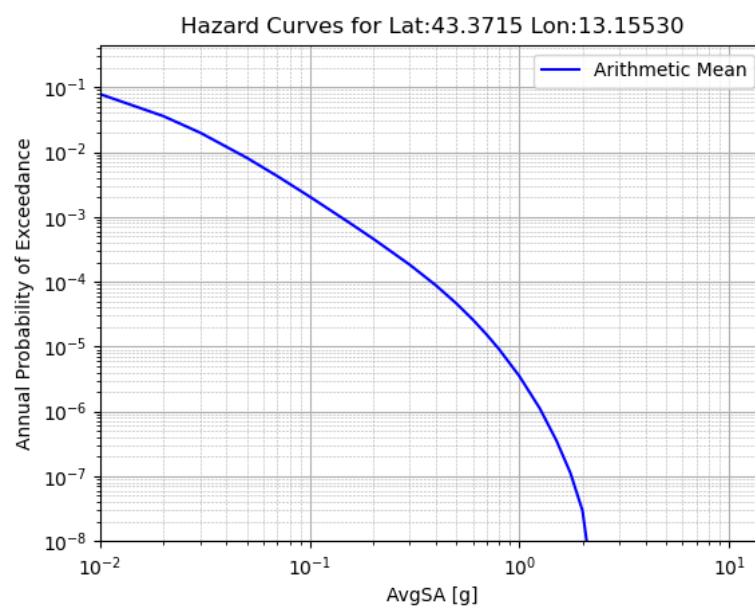
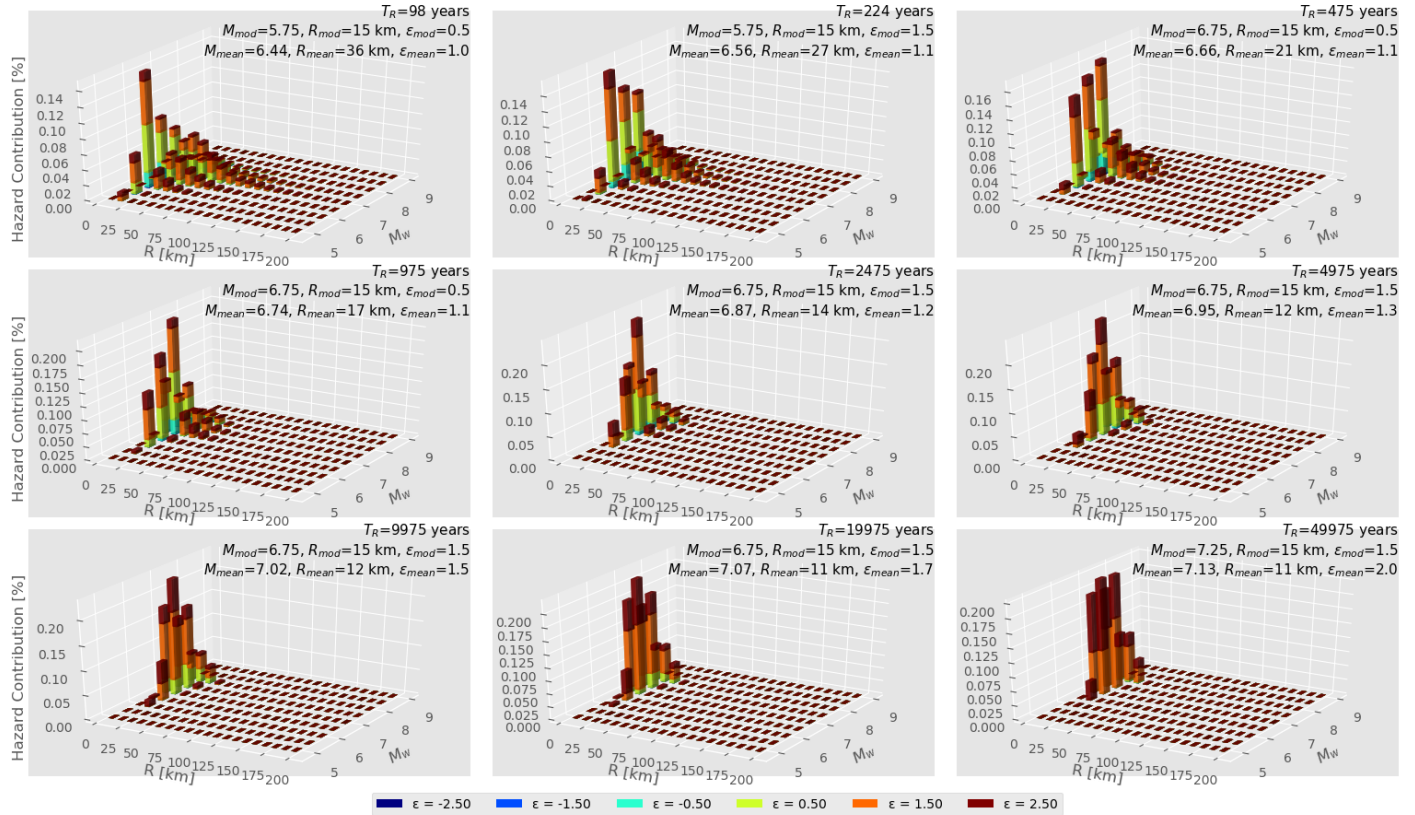


Figure 7.3. Hazard Curve for Cingoli site

Table 7.4. Nine chosen intensity levels. Probability of exceedance in 50 years and corresponding Intensity Measure level. Cingoli site

PoE in 50yrs	Return Period [yrs]	AvgSa [g]
0.4	98	0.044
0.2	225	0.068
0.1	475	0.099
0.05	975	0.139
0.02	2475	0.212
0.01	4975	0.288
0.005	9975	0.381
0.0025	19975	0.487
0.001	49975	0.647

The causal rupture characteristics (i.e. magnitude and distance) contributing most to each IM level were identified via Hazard Disaggregation, given in the Figure 7.4.

Disaggregation of Seismic Hazard
Intensity Measure: AvgSA
Latitude: 43.3715, Longitude: 13.1553

Figure 7.4. Seismic Hazard Disaggregation – Cingoli site.

It can be observed from above (Figure 7.2, Figure 7.3, Table 7.4 and Figure 7.4) that the bridge is located in an area with relatively low seismicity. Hence the site was virtually moved to the more hazardous site of L'Aquila. The similar hazard results for L'Aquila are given in the following. The hazard maps, hazard curves and the nine intensity levels are given in Figure 7.5, Figure 7.6 and Table 7.5, respectively.

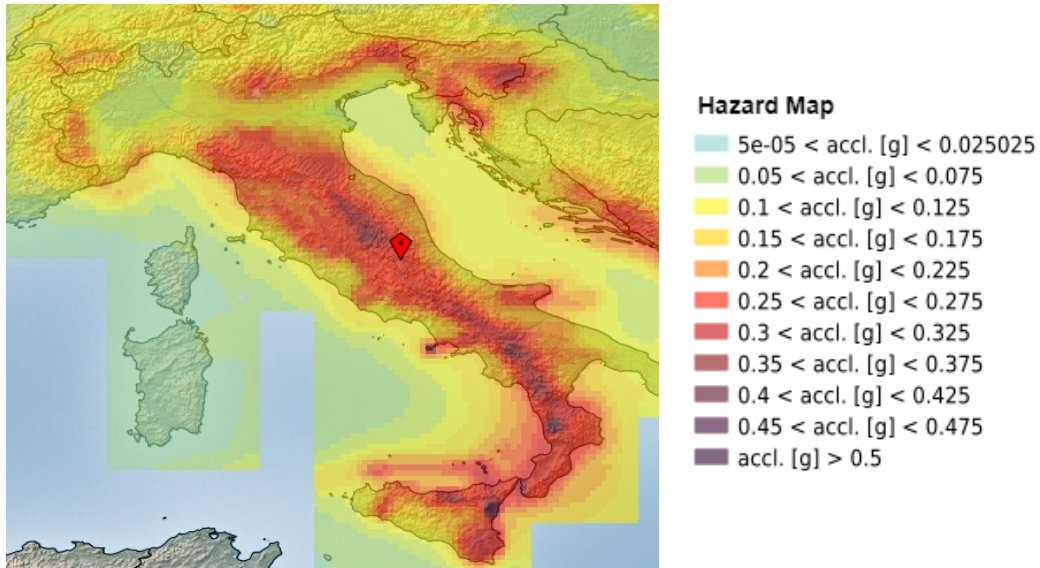


Figure 7.5. Location of the L'Aquila site on the Italian hazard map of median PGA with 475 years return period on rock soil conditions. [European Facilities for Earthquake Hazard and Risk (EFEHR), 2017]

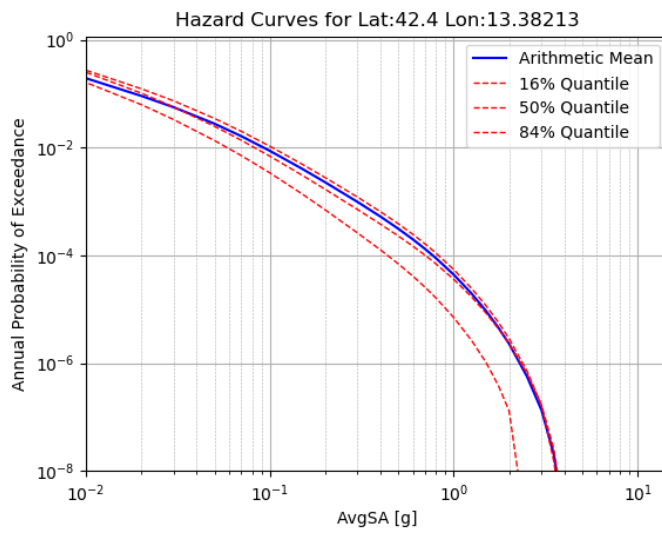


Figure 7.6. Hazard Curves for L'Aquila site

Table 7.5. Nine chosen intensity levels. Probability of exceedance in 50 years and corresponding Intensity Measure level. L'Aquila site

PoE in 50yrs	Return Period [yrs]	AvgSa [g]
0.4	98	0.092
0.2	225	0.142
0.1	475	0.207
0.05	975	0.293
0.02	2475	0.447
0.01	4975	0.596
0.005	9975	0.768
0.0025	19975	0.961
0.001	49975	1.243

The causal rupture characteristics (i.e. magnitude and distance) contributing most to each IM level were identified via hazard disaggregation, given in the Figure 7.7.

Disaggregation of Seismic Hazard
Intensity Measure: AvgSA
Latitude: 42.4000, Longitude: 13.3821

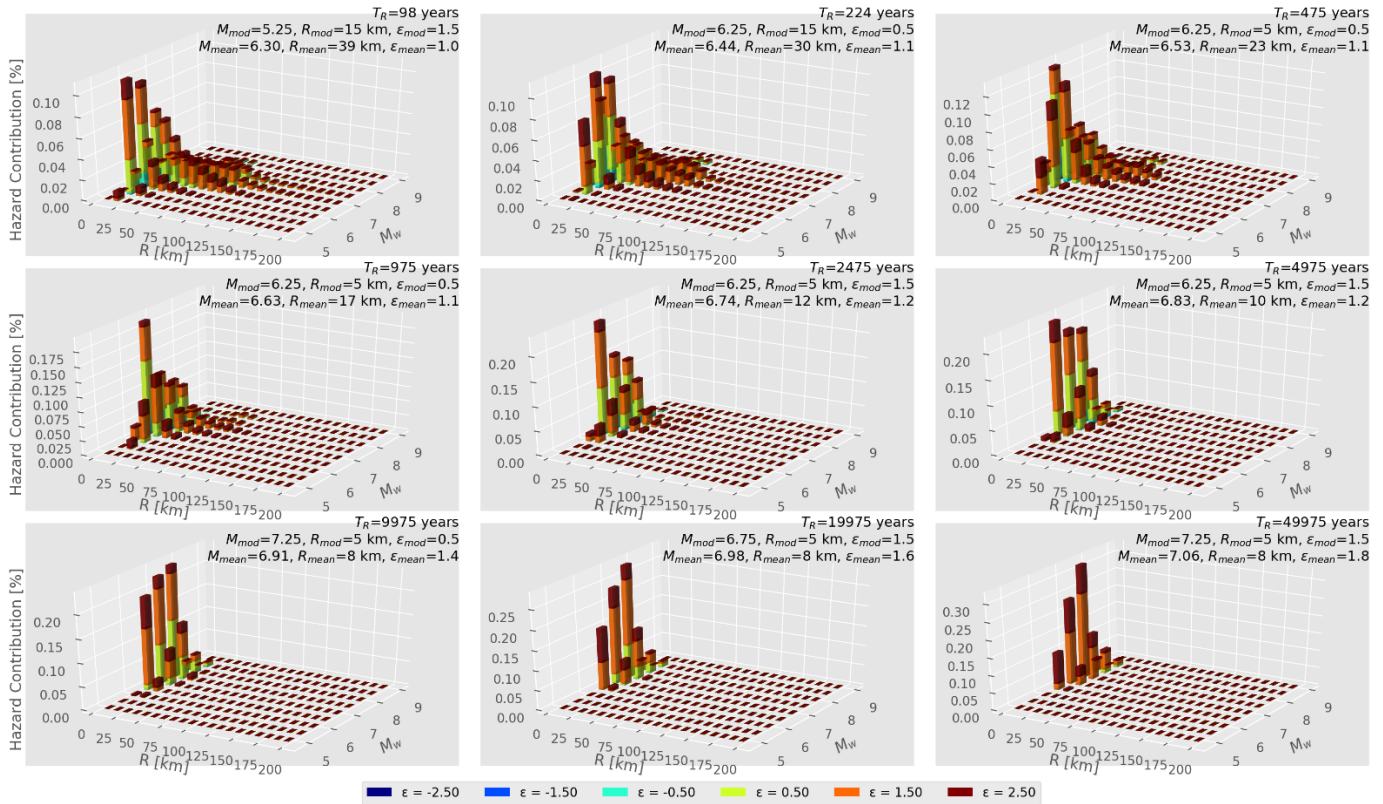


Figure 7.7. Seismic Hazard Disaggregation – L'Aquila site.

The increase in the seismic hazard is evident and in this way the analyses and results will be much accentuated.

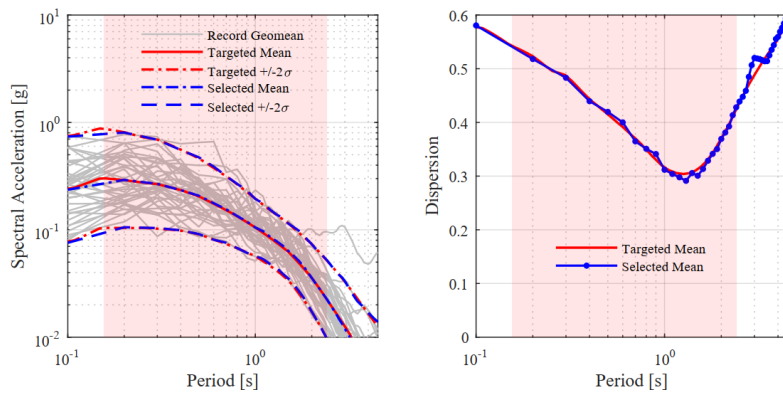
7.2 GROUND MOTION RECORD SELECTION

In order to perform structural NLTH Analyses, to obtain the EDPs of interest, 40 ground motion record pairs were selected per intensity level. The PEER NGA-West1 database, with 3527 available records, was used from which the records were selected. Each ground motion record had 2 horizontal components, but no vertical component. A total of 9 intensity levels were investigated, corresponding to probabilities of exceedance ranging from 40% to 0.1% in 50 years, in order to cover a wide range of event return periods. For the AvgSa-based selection, the conditional spectrum (CS) approach, outlined by [Baker J.

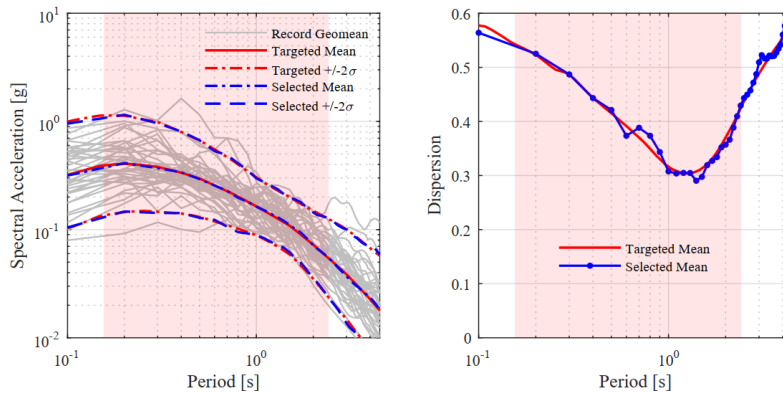
W., 2011] was followed, with the extension to AvgSa as the IM described in [Kohrangi, Bazzuro, Vamvatsikos, & Spillatura, 2017].

The following plots show the conditional spectrum with its dispersion to be matched and the corresponding spectrum and dispersion obtained from the geometric mean of selected GMs [Baker & Cornell, 2006], in each intensity measure level, sorted from the lowest intensity to the highest.

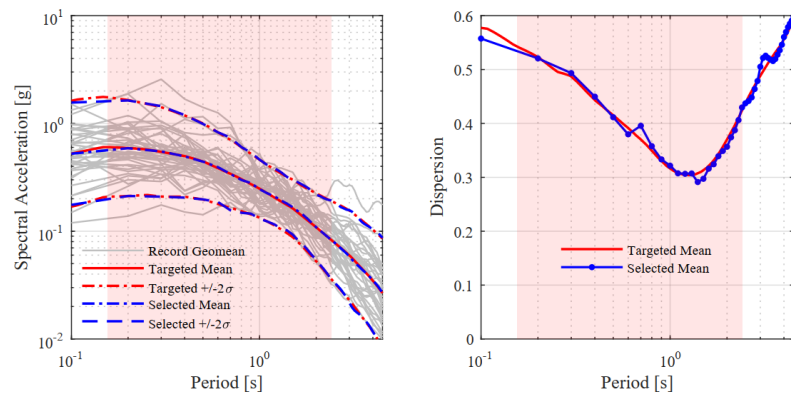
AvgSa=0.092g:



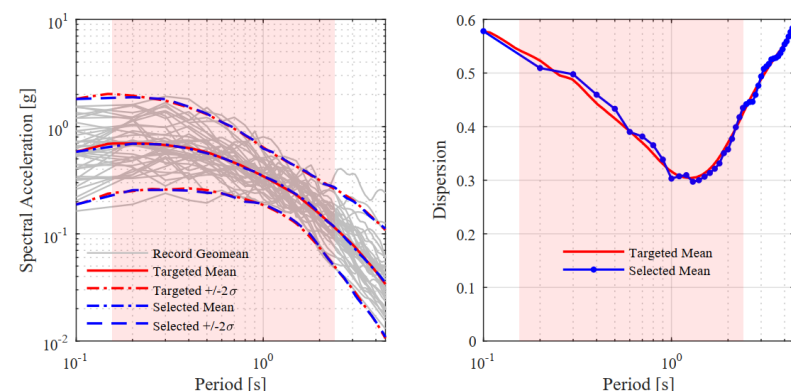
AvgSa=0.142g:



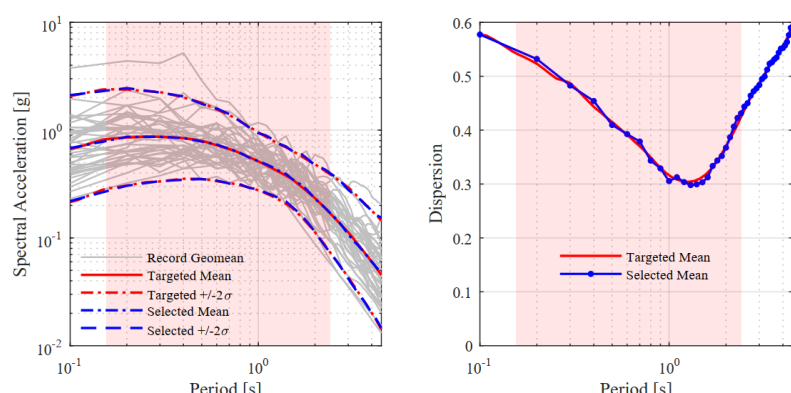
AvgSa=0.207g:



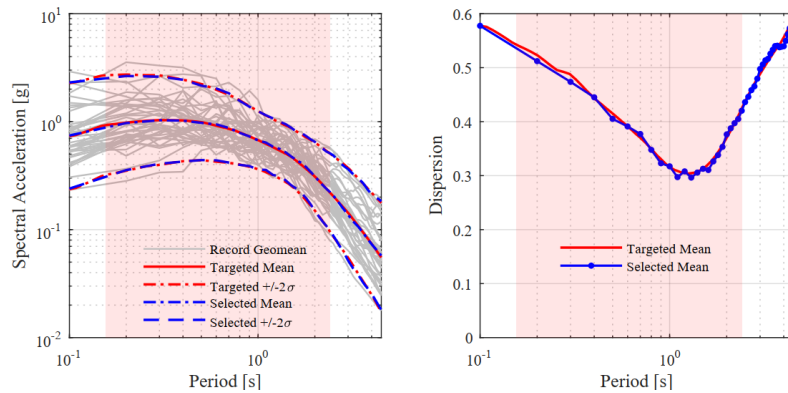
AvgSa=0.293g:



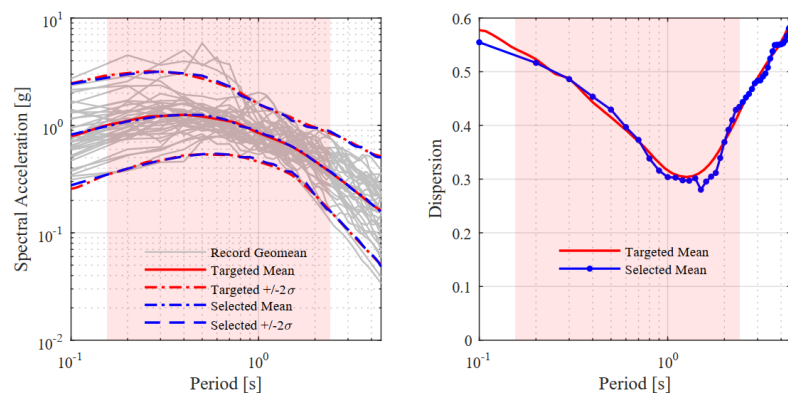
AvgSa=0.447g:



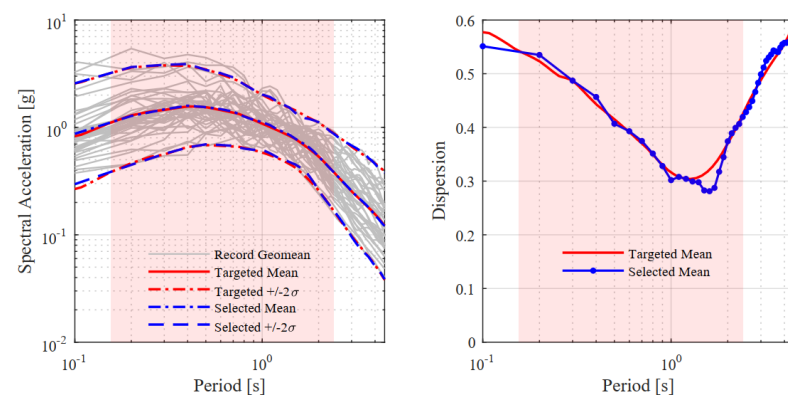
AvgSa=0.596g:



AvgSa=0.768g:



AvgSa=0.961g:



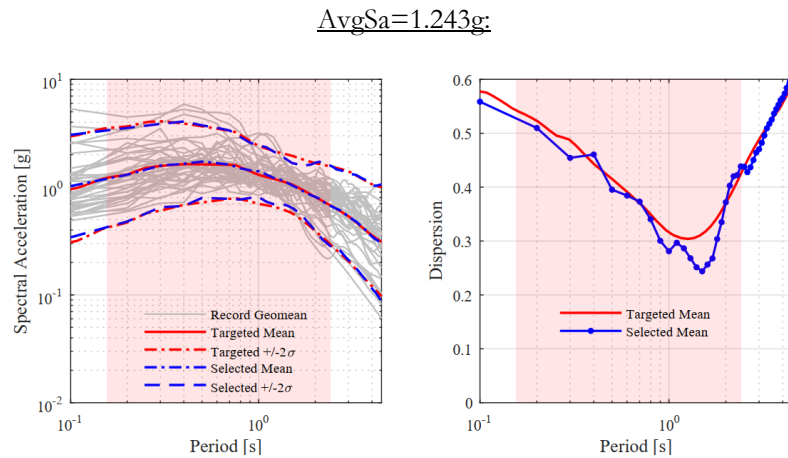


Figure 7.8. Target Conditional Spectra, Geomean Spectra of Selected Ground Motion Pairs and their corresponding dispersion for each intensity.

From a visual evaluation of the above figures, the matching to the conditional mean spectrum (CMS) and to the mean spectrum $\pm 2\sigma$ appears to be satisfactory for the scope of the study.

7.3 STRUCTURAL ANALYSIS – MSA RESULTS

7.3.1 Piers

The structure was analysed in each intensity level with the selected record sets. A multi-stripe analysis (MSA) was performed, capturing the peak drift ratio in each pier element at each intensity level, shown indicatively for two pier elements in Figure 7.9.

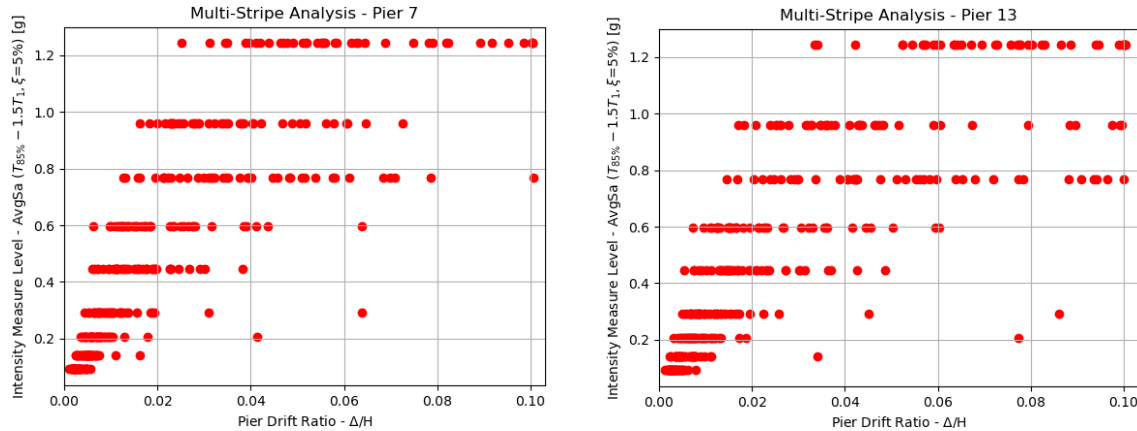


Figure 7.9. MSA Results for Drift Ratio of Pier elements 7&13

7.3.2 Bearings

An MSA of the results was also performed for the bearings of the bridge, with some indicative results shown in the graphs below. As expected, the bearings lock when they reach a displacement of 0.05m in the Y direction and 0.065m in the X direction. However, many records do not bring the bearings to their ultimate displacement. This is mainly observed in bearings supporting spans with high curvature (with respect to the previous and/or next one).

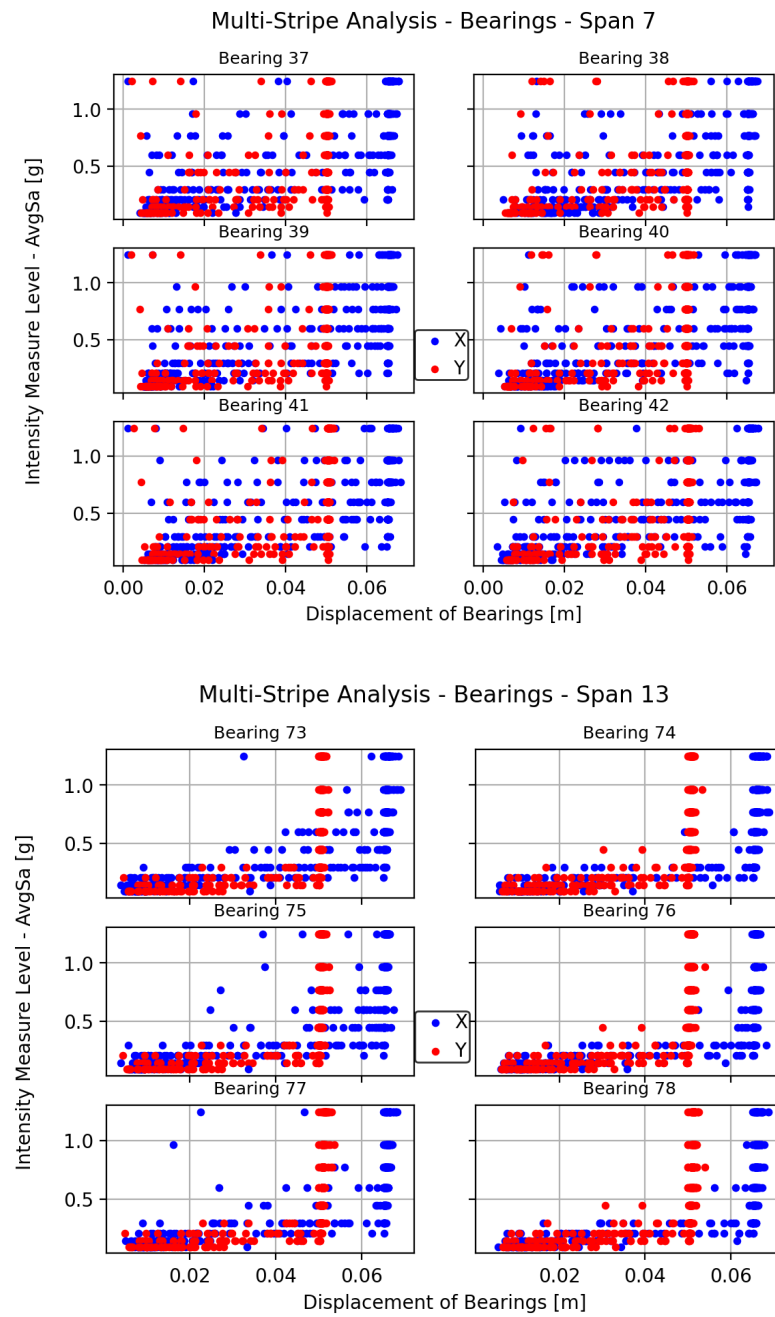


Figure 7.10. Maximum displacement observed in the bearings during each record in each local direction.

7.4 DAMAGE MODELS

Damage models are fundamental elements within a probabilistic loss-assessment framework, such as PBEE, for the seismic assessment of structures. They can express the probability of exceeding a certain predefined damage limit, given the EDP (maximum response of an element in a local sense or structure in a global sense) obtained from the structural analysis. In other words, they can express the probability of being in a certain damage state, given the member or structure EDP.

To define a damage model of a component, a statistical distribution needs to be first fitted that best describes the model, which in this case is probably the lognormal CDF, in agreement with the PEER-PBEE framework. Then the main parameters of this distribution (median value, θ and logarithmic standard deviation, β) need to be determined.

7.4.1 Abutments

Until today there is still a large uncertainty in the performance of bridge abutments and their respective consequences (i.e. expected damage, repairing costs and disruption time). A detailed analysis would be required to define the damage models of each particular abutment, depending on the abutment type (e.g. seat, integral), wing walls geometry, foundation type, foundation soil and backfill material characteristics, sacrificial elements (if present) and on many other characteristics. Due to these inherent complications, some average values could be adopted for the abutment damage models from the literature, given in Table 7.6.

Table 7.6. Damage limits for abutments found in literature

Source	Damage Limit States for Abutments in the Transverse Direction							
	DL-1		DL-2		DL-3		DL-4	
	θ [mm]	β	θ [mm]	β	θ [mm]	β	θ [mm]	β
Nielson and DesRoches [2007a]	9.8	0.7	37.9	0.9	77.2	0.85	--	--
Ramanthan <i>et al.</i> [2012]	9.75	0.25	37.9	0.25	77.2	0.47	1000	0.47
Ramanthan <i>et al.</i> [2015]	25.4	0.35	101.6	0.35	--	--	--	--
Ghosh and Padgett [2011]	18.1	0.25	108	0.2	218	0.47	--	--
Nielson and DesRoches [2007b]	9.8	0.7	37.9	0.9	77.2	0.85	--	--
Bisadi and Padgett [2015]	12.34	0.17	56.54	0.1	110.59	0.06	--	--
Kameshwar and Padgett [2017]	9.25	0.25	37.9	0.25	77.2	0.47	1000	0.47

Table 7.7. Assigned damage model values for abutments in the transverse direction

DL	θ [mm]	β
DL-1	15	0.45
DL-2	70	0.5
DL-3	120	0.5
DL-4	--	--

The values in Table 7.7 correspond, roughly, to the average values of those presented in Table 7.6. The state of collapse in the bridge (exceedance of DL-4) is not reached from the damage in the abutments in the transverse direction.

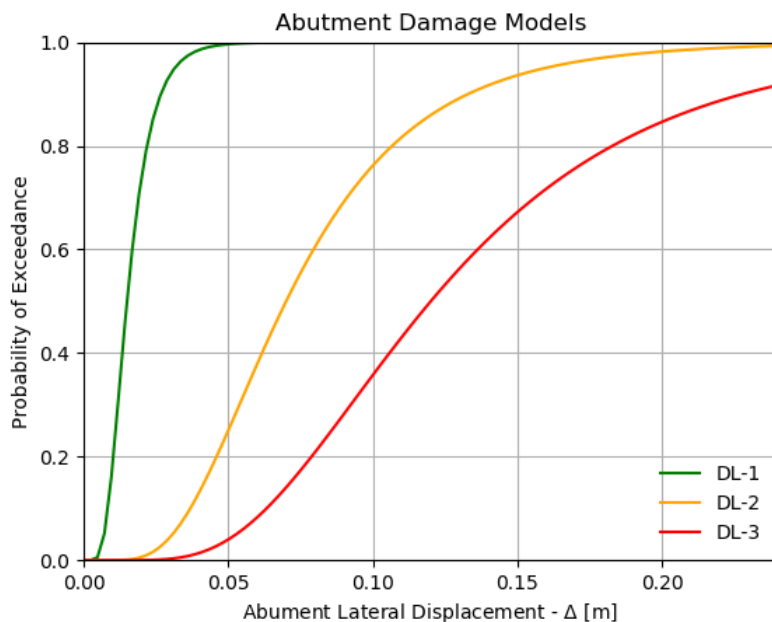


Figure 7.11. Indicative damage models for abutments

The damage states DS-1, DS-2 and DS-3 correspond to qualitative descriptions of slight, moderate and extensive damage.

In this study, the damages to the abutments are not considered neither in structure level or in component-based loss calculations, as firstly their definition is too broad and inaccurate and secondly, their contribution to overall losses was deemed negligible.

7.4.2 Piers

For bridges, there are not many available experimental results for the characterization of damage in the RC columns hence the numerical simulation acquired particular relevance. Perdomo *et al.* [2020] have proposed approximate, yet accurate, damage models for cantilever circular section RC bridge columns. Damage models consisting of a library of median and logarithmic dispersion values for curvature ductility, displacement ductility and drift, describing the probability of reaching a particular damage limit were generated as a function of key parameters of circular RC bridge columns, such as diameter, length, axial load etc. The range of these parameters used to generate the database is given in Table 7.8. It should be noted that some parameters of the piers of Cingoli bridge fall slightly outside the boundaries of the database. Hence, wherever the pier parameters are lower than the lower boundary of the database, the lowest value of the database is considered to generate the pier damage models. Although the piers have varying section in Cingoli bridge the boundary conditions for pier elements especially the ones with smaller sections (where most of the damages are concentrated) are very close to a cantilever behaviour.

The seismic loss calculations were performed using the damage models mentioned here and discussed in Perdomo *et al.* [2020], using the individual pier drift ratios as the EDP. By choosing the appropriate combination of parameters listed in Table 7.8, the damage models of the piers were generated.

Table 7.8. Column parameters used to generate the database. [Perdomo & Monteiro, 2020]

D [m]	f'_c [MPa]	f_y [MPa]	ρ_l [%]	$\rho_v/\rho_{v,conf}$	ALR	H/D
0.8	21	400	0.5	1.0	0.1	1.5
1.0	28	420	1.0	0.8	0.2	3.0
1.5	35	450	1.5	0.6	0.3	5.0
2.0	42	500	2.0	0.5	0.4	7.0
2.5	48		2.5	0.4		9.0
3.0			3.0	0.2		
3.5			3.5			
4.0			4.0			

where,

D = section diameter;

f'_c = unconfined concrete compressive strength based on standard cylinder test;

f_y = longitudinal reinforcement yield strength;

ρ_l = longitudinal reinforcement ratio;

ρ_v = transverse reinforcement ratio;

$\rho_{v,conf} = \max \left\{ 0.45 \left(\frac{A_g}{A_c} - 1 \right) \frac{f'_c}{f_y}, 0.12 \frac{f'_c}{f_y} \right\}$ transverse reinforcement ratio corresponding to code confinement requirements. In this study, confinement requirements were computed according to the AASHTO LRFD bridge design specifications (2007);

ALR = column axial load ratio;

H = column length;

Table 7.9. Pier parameters of Cingoli Bridge

Pier	D	f'_c	f_y	$q_t [\%]$	$q_v/q_{v,conf}$	ALR	H/D
1	2.6	25	430	0.43	0.13	0.06	5.23
2	4.0	25	430	0.30	0.08	0.03	1.10
3	2.6	25	430	0.43	0.13	0.05	6.33
4	4.0	25	430	0.30	0.08	0.03	1.59
5	2.6	25	430	0.43	0.13	0.05	6.33
6	4.0	25	430	0.30	0.08	0.03	1.78
7	2.6	25	430	0.43	0.13	0.05	6.33
8	4.0	25	430	0.30	0.08	0.04	2.93
9	2.6	25	430	0.43	0.13	0.05	6.33
10	4.0	25	430	0.30	0.08	0.04	2.91
11	2.6	25	430	0.43	0.13	0.05	6.33
12	4.0	25	430	0.30	0.08	0.04	3.16
13	2.6	25	430	0.43	0.13	0.05	6.33
14	4.0	25	430	0.30	0.08	0.04	3.72
15	2.6	25	430	0.43	0.13	0.05	6.33
16	4.0	25	430	0.30	0.08	0.04	3.75
17	2.6	25	430	0.43	0.13	0.05	6.33
18	4.0	25	430	0.30	0.08	0.04	2.41
19	2.6	25	430	0.43	0.13	0.05	5.35
20	4.0	25	430	0.30	0.08	0.03	1.25

21	2.6	25	430	0.43	0.13	0.05	6.33
22	2.6	25	430	0.43	0.13	0.06	4.47
23	2.6	25	430	0.43	0.13	0.05	2.74

As it can be seen from Table 7.9, the parameters q_l , $q_v/q_{v,conf}$ and ALR fall outside the parameters of the database, but this was judged to be a small acceptable error, given also the empirical nature of the damage models and the comparative scope of this study.

Qualitatively, the 4 predefined damage limits are associated with the onset of the following physical conditions in the columns:

- **Slight (DL-1):** onset of yielding of the column, minor damage is expected, however repair actions might be necessary in order to prevent further deterioration due to other effects (e.g. corrosion).
- **Moderate (DL-2):** onset of cover concrete spalling, repair actions are necessary in order to replace the affected concrete volume and prevent further deterioration.
- **Extensive (DL-3):** onset of buckling of the longitudinal reinforcement or the fracture of the transverse reinforcement (whichever happens first), repair actions might involve the replacement of concrete and reinforcement or the reconstruction of the column.
- **Complete (DL-4):** crushing of concrete core or fracture of the longitudinal reinforcement, the column might still be able to carry gravity loads, but resistance to lateral deformations cannot be guaranteed, exceedance of this damage limit is associated with a condition of collapse.

The indicative damage models of pier elements 7 and 12 (small and big section pier elements, respectively) are shown in Figure 7.12, where DL-4-S is the shear failure damage limit. It was observed that the shear failure limit is not reached before the flexural collapse in any of the pier elements, ergo it has almost zero probability of exceedance in the plotting window.

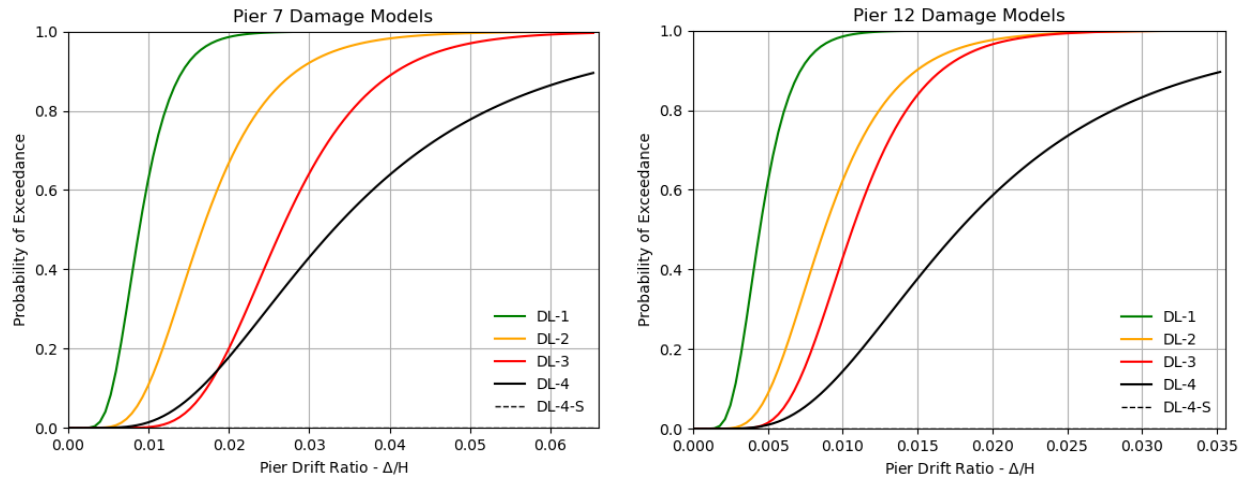


Figure 7.12. Damage Models of pier elements 7 & 12^d

7.5 FRAGILITY CURVES GENERATION

Fragility curves relate the damage state of the system with the ground motion intensity measure level and can be generated at structure level or at component level.

For the component level, fragility curves were generated for each pier element using maximum likelihood estimation. For the global structure level approach, the fragilities of the most vulnerable pier, were taken as representatives of the system fragilities. In other words, the structure fragilities were obtained by considering the maximum probability of exceedance value of each DL, from all the piers. Equation (7.3) describes the aforementioned, where $\max[P(F_{piers})]$ is the fragility function of the most vulnerable pier element and $P(F_{system})$ is the fragility function of the system.

$$\max[P(F_{piers})] = P(F_{system}) \quad (7.3)$$

The component (piers) fragility curves and the structure fragility curves are given in the following graphs. A description of how uncertainty was handled in the generation of these fragilities is given in section 2.3.

^d Wherever the probability of exceedance of DL-4 is higher than that of DL-3, the DL-3 was ignored and was assumed that DL-4 comes after DL-2. This happens for example in the lower drift ratios in the damage models, and it's a product of the higher standard deviation of DL-4.

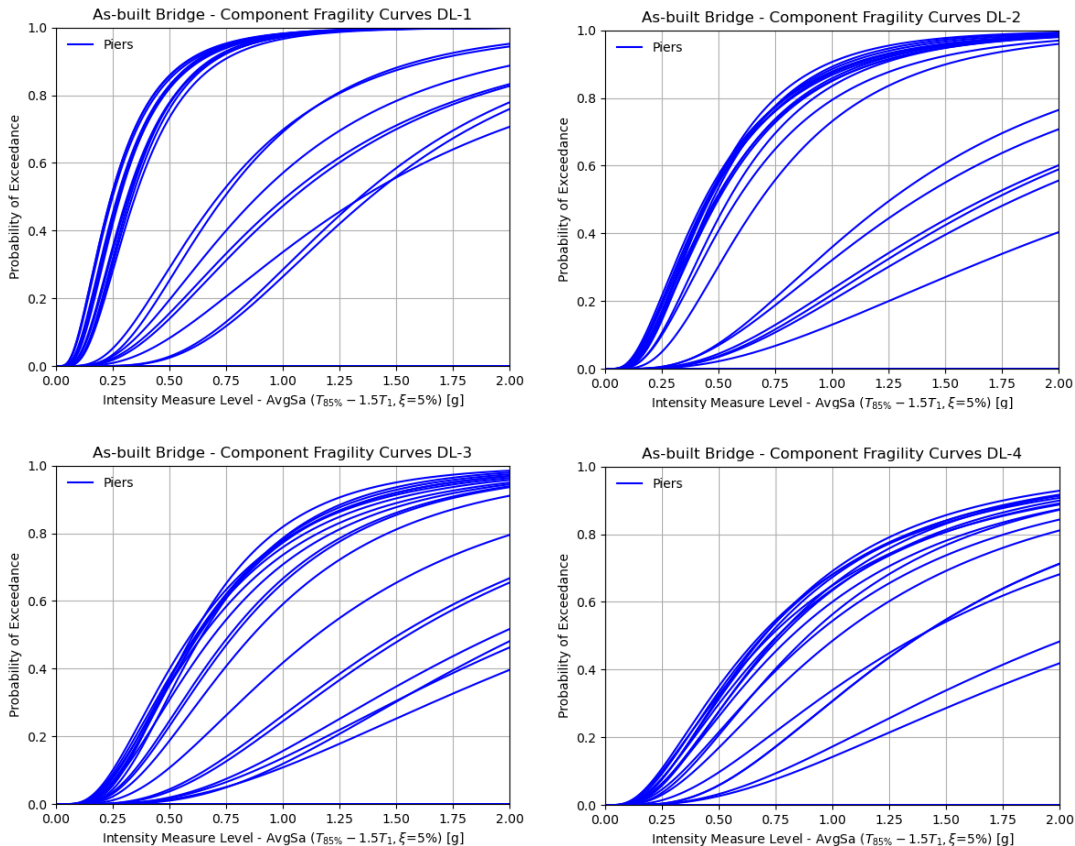


Figure 7.13. Fragility curves of pier components for different damage limits

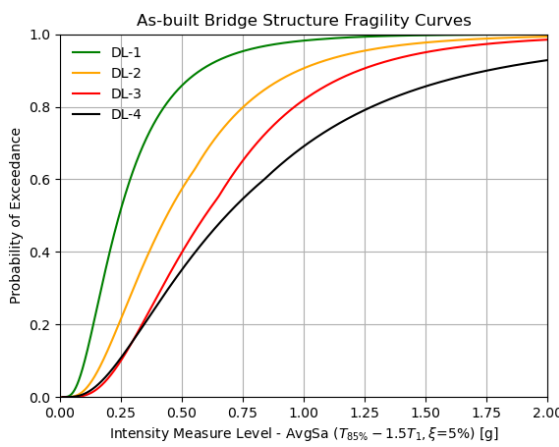


Figure 7.14. Structure fragility curves for different damage limits

7.6 STRUCTURE LEVEL DIRECT SEISMIC LOSS ASSESSMENT

The next step was to calculate the corresponding seismic losses, using a structure level approach, utilizing also the consequence functions, as explained in Section 2.5.

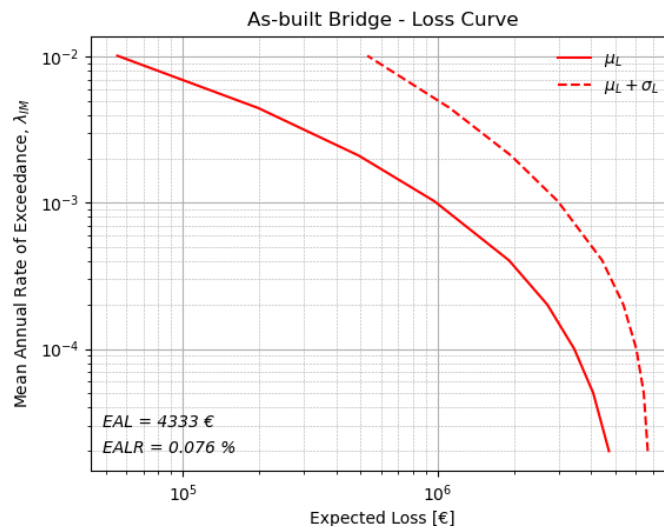


Figure 7.15. Resultant loss curve using simplified approach (HAZUS)

It can be observed that the expected annual loss ratio estimated with the simplified approach (0.076%) is very low, when compared to values typically observed for building structures in Italy [O'Reilly, Monteiro, Nafeh, Sullivan, & Calvi, 2020]. It should be noted that this EAL ratio comprises contributions arising solely from direct economic losses and does not consider the impacts of potential indirect losses.

7.7 COMPONENT LEVEL DIRECT SEISMIC LOSS ASSESSMENT

With the procedure outlined in Section 2.6, the direct seismic losses at a component level were calculated and shown as follows.

For each IM level investigated, it was possible to obtain the distribution of the repair cost given 'collapse' cases, given 'no-collapse' cases, and all cases together. Sample results of these calculations applied to the bridge structure are shown below in Figure 7.16. The distribution of loss given no-collapse was disaggregated and mean losses per component were estimated, as shown in Figure 7.17. Note that the repair costs were estimated separately for the 23 pier elements and not globally for the 13 piers with varying section. Moreover, for each IM level, cumulative distribution function (CDF) and complementary CDF (CCDF=1-CDF) for the repair costs were obtained (Figure 7.18). CCDFs obtained for each IM level is depicted in Figure 7.19a. Moreover, by putting together the CCDFs

from all IM levels investigated, Equation (2.8) can be solved and the mean loss versus annual rates of exceedance are illustrated in Figure 7.19b. Likewise, the loss versus IM level and the annual rate of exceedance versus expected loss graphs were computed and depicted in Figure 7.20, for both the expected value and the expected value + a standard deviation of the repair cost.

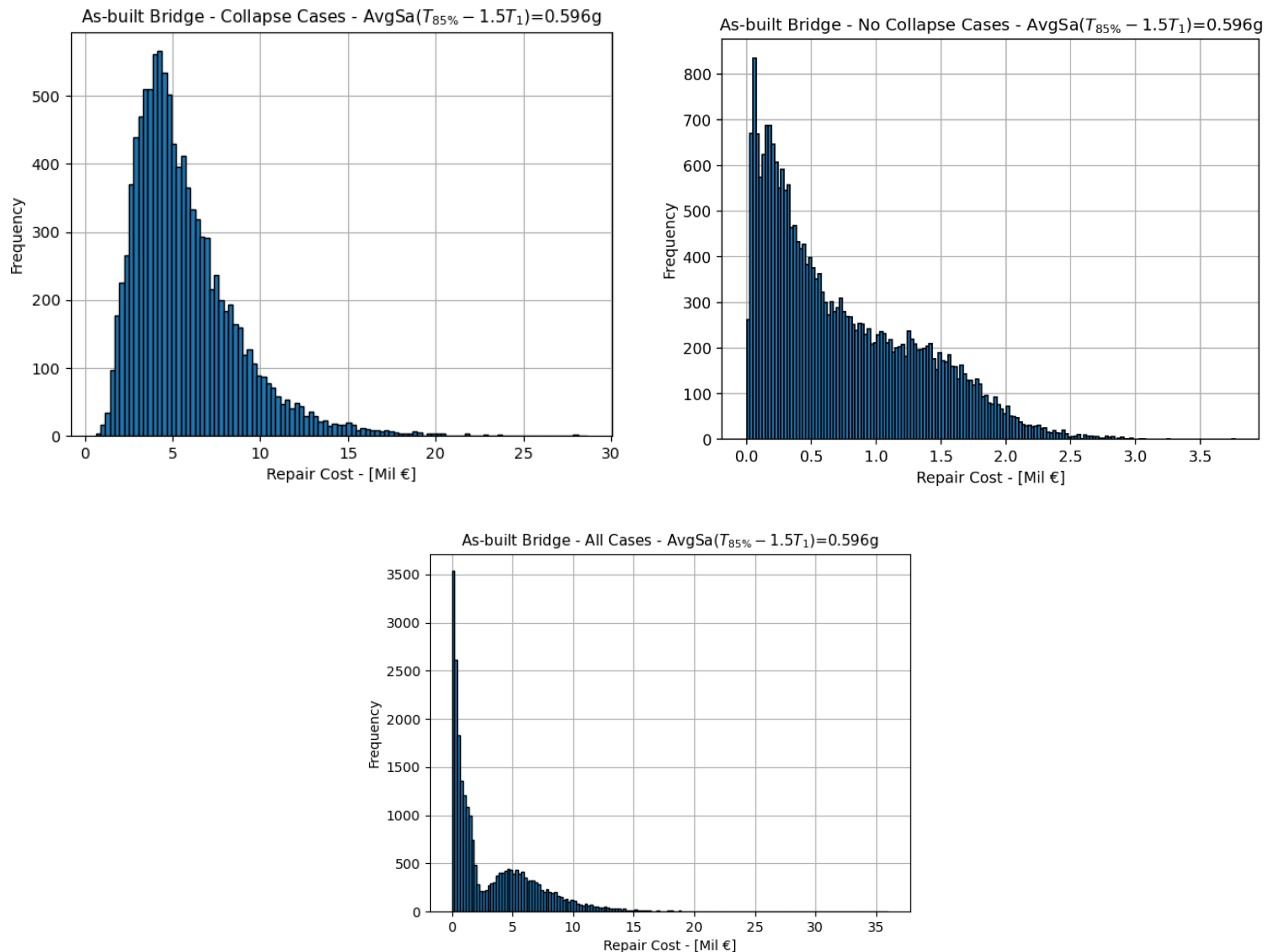


Figure 7.16. Sample loss distribution (a) Collapse cases (b) No Collapse Cases (c) All cases (for $Tr = 4975$ years events)

It can be seen from Figure 7.16 that the ‘collapse’ cases are less frequent, but have increased repair cost, with respect to the ‘no-collapse’ cases. When all the cases are put together, two peaks can be noticed, one at low repair cost with high frequency of occurring and one at higher repair cost but much lower frequencies.

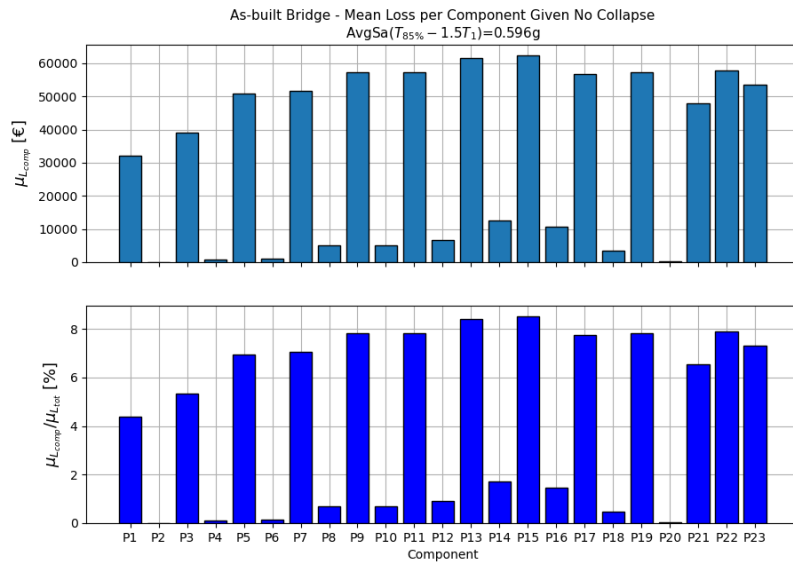


Figure 7.17. Mean loss per component given no collapse (for $Tr = 4975$ years events).

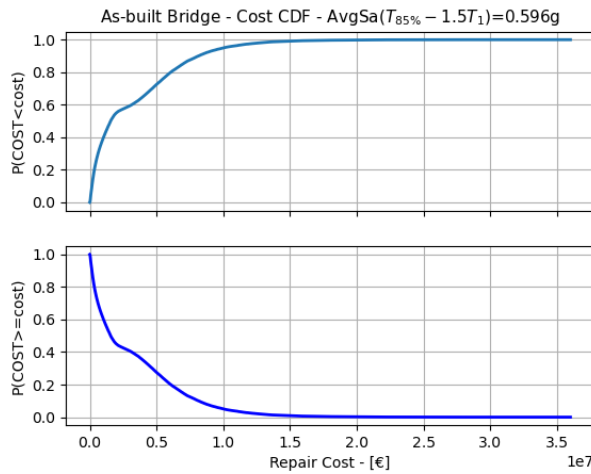


Figure 7.18. Cost CDF and CCDF (for $Tr = 4975$ years events).

From Figure 7.17, it can be observed that the pier element 15 is the component with the highest mean loss in that intensity level. Generally, all the upper elements of the piers present similar mean losses, while the lower elements have much lower losses, as expected.

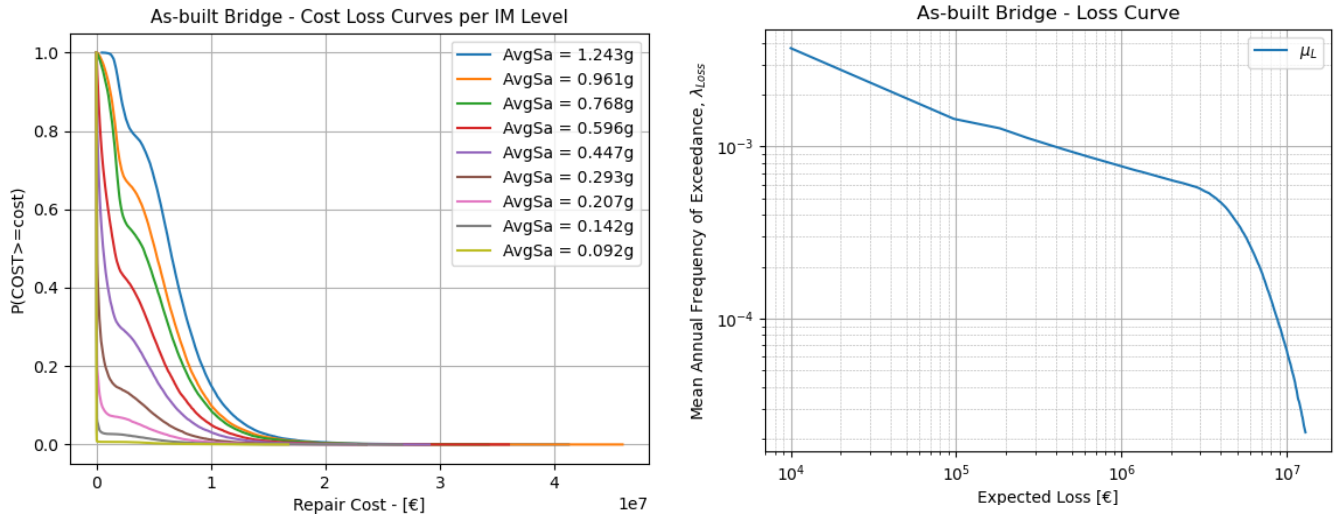


Figure 7.19. Loss curves per IM level and mean loss curve.

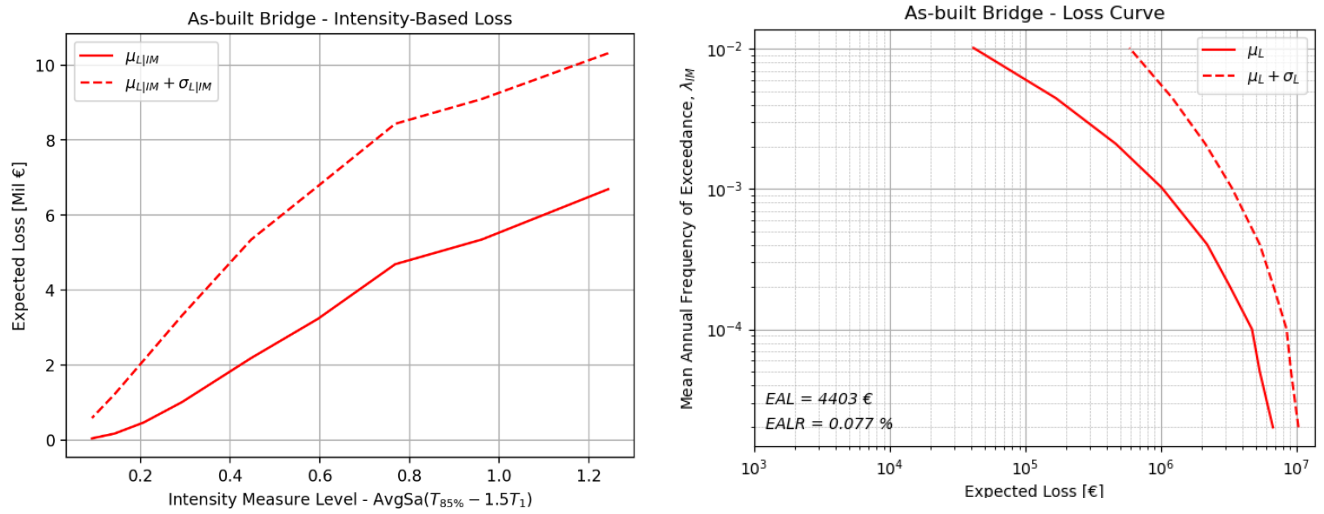


Figure 7.20. Expected intensity-based and time-based losses using the comprehensive approach (FEMA-P58-1, 2018). (a) Loss vs IM level (b) loss curve

7.8 COMPARISON OF SIMPLIFIED AND COMPREHENSIVE LOSS ASSESSMENT APPROACHES

A comparison has been made between simplified (structure-level) and comprehensive (component-based) loss assessment, comparing the intensity-based and time-based loss curves of each approach as shown in Figure 7.21.

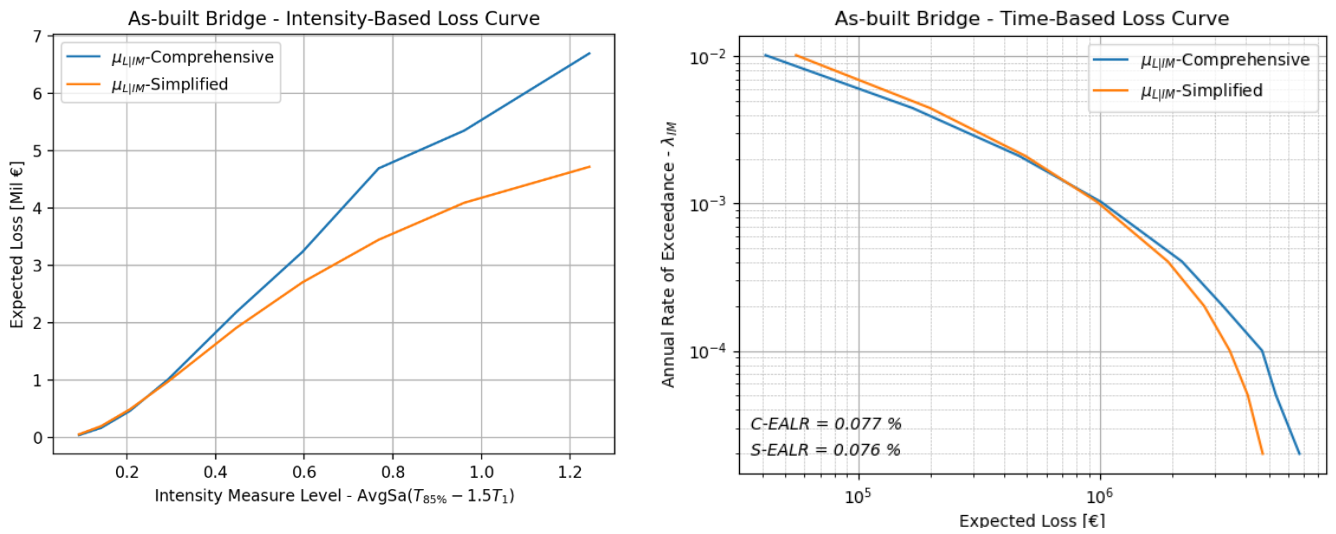


Figure 7.21. Comparison of simplified and comprehensive loss assessment approaches through the intensity-based and time-based loss curves.

It can be firstly observed that the EAL ratio (EALR) that the two approaches predict is almost identical (0.077% from the comprehensive approach and 0.076% from the simplified approach), with just small discrepancies. From a first glimpse in the intensity-based curves, one might say that the comprehensive approach predicts way higher overall losses than the simplified approach. However, looking at the time-based loss curve it can be seen that the simplified approach predicts higher losses in the higher annual rates of exceedance (lower IM levels) and lower losses in the lower annual rates of exceedance. These small heterogeneities are balancing out when calculating the EALR, to give a similar value.

8. Direct Seismic Loss Assessment of the Retrofitted Bridge

The loss assessment of the retrofitted bridge is estimated, in the same manner as for the as-built bridge, and presented in the following.

Even though the predominant period range is different for the isolated (retrofitted) structure, as it can be seen in Figure 8.1 and Table 7.1, compared with Figure 7.1 and Table 8.1, the same ground motion records that were used for the as-built structure, were also used for the retrofitted structure. Since time-based assessments were performed to assess the performance of the bridge and the conditional spectrum was used to carefully select and scale the ground motions, the eventual results will be similar, no matter the conditioning period [Lin, Haselton, & Baker, 2013]. The reproducibility of the time-based assessment results, for varying conditioning periods, results from the fact that the intensity measure is merely a virtual link between the ground motion hazard and structural response. If this link is maintained carefully, then the time-based assessment prediction will be consistent, given always that the exact conditional spectrum is used. This is a property of the conditional spectrum called hazard consistency.

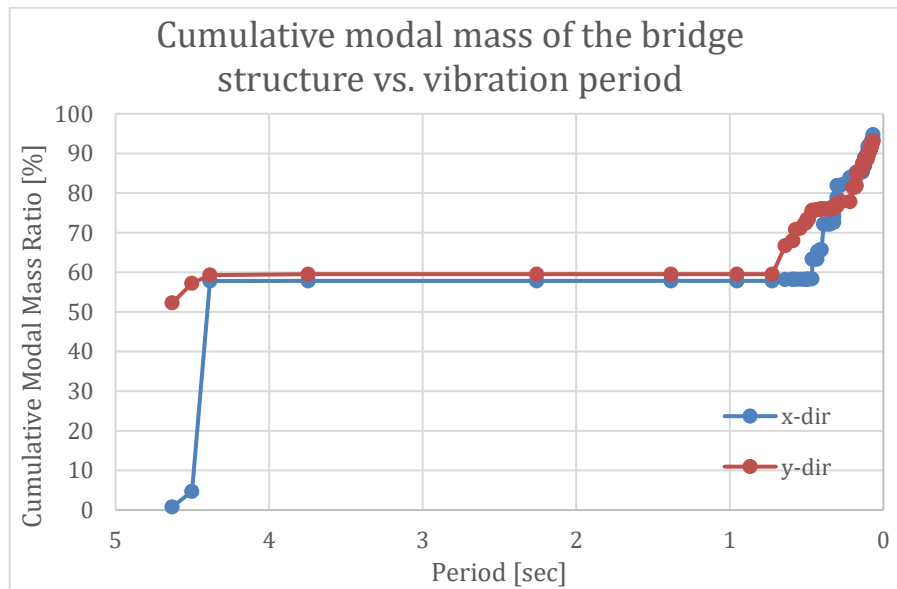


Figure 8.1. Cumulative modal mass of the bridge versus vibration period

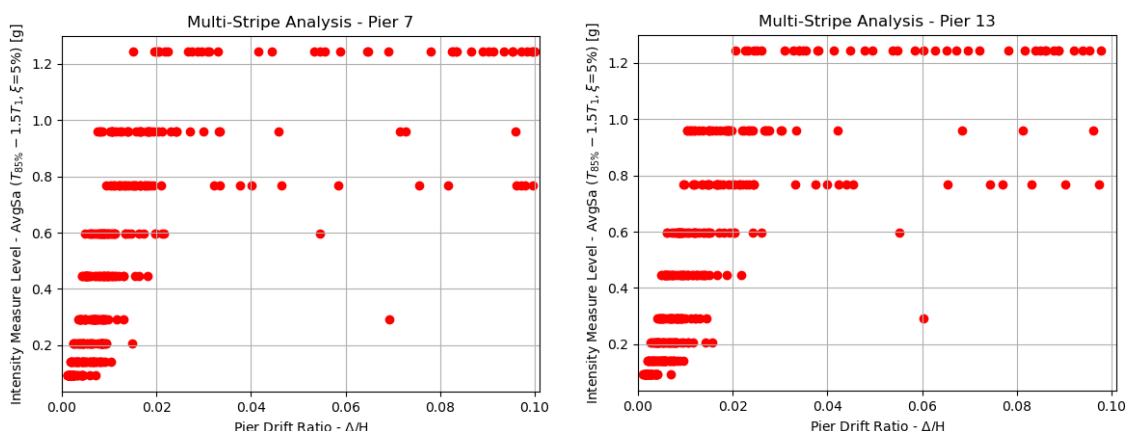
Table 8.1. Predominant period range of retrofitted structure

$[T_{85\%} - T_1]$	
T_{lower} [sec]	0.20
T_{upper} [sec]	4.63

The seismic hazard, local soil conditions and selected ground motions were kept the same also for the loss estimations of the retrofitted model.

8.1 STRUCTURAL ANALYSIS – MSA RESULTS

The retrofitted structure was analysed with the previously defined ground motions record sets. The peak drift ratio of each pier at each IM level was recorded and depicted below in an MSA fashion.

**Figure 8.2. MSA Results for Drift Ratio of Pier elements 7&13 of retrofitted model**

It can be observed from Figure 8.2 that the majority of the peak drift ratios were below 2% drift at every intensity, except for the three highest ones. Also, it can be observed that the dispersion in the highest intensity is drastically higher compared to the other intensity levels.

An MSA was performed also for the new bearings (friction pendulum isolators) with their maximum displacements recorded at each intensity level. The displacements were distinguished between their local X direction (parallel to the supported deck) and their local Y direction (perpendicular to the supported deck).

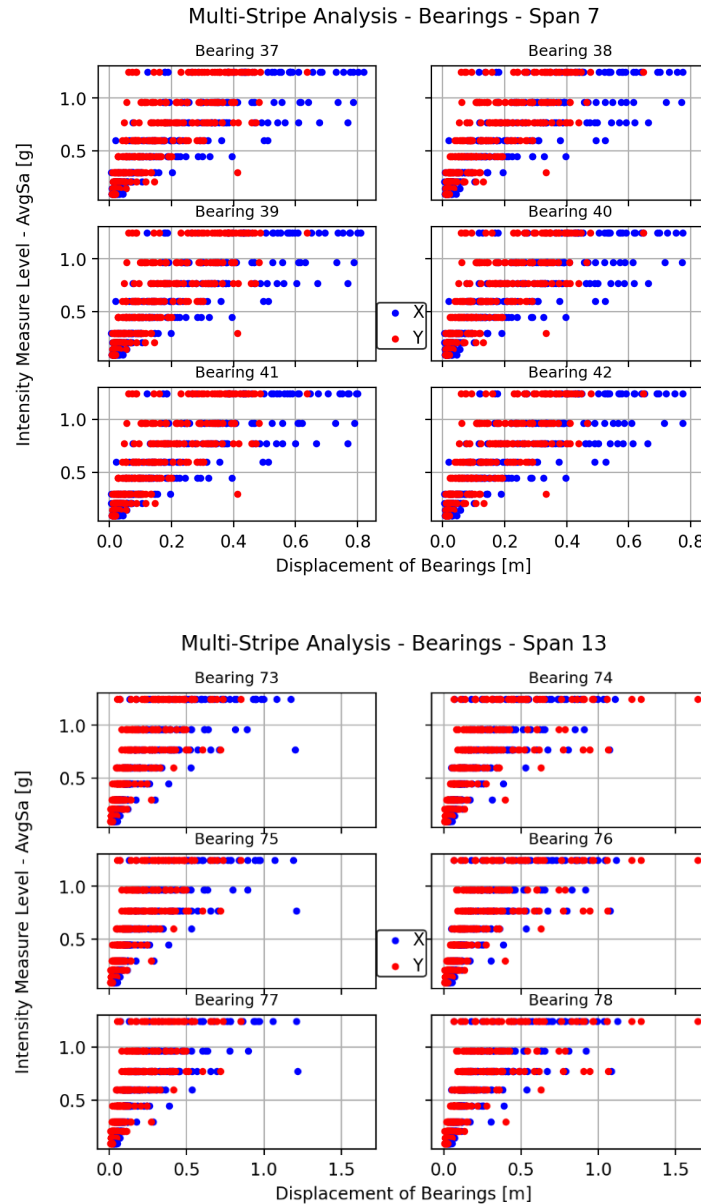


Figure 8.3. Maximum displacement observed in the Inverted Friction Pendulum isolators (bearings) during each record in each local direction.

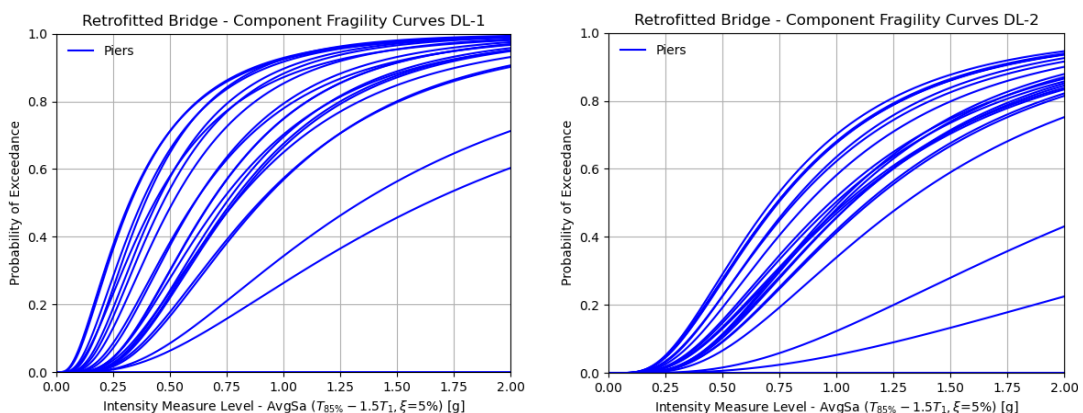
From Figure 8.3, it can be inferred that the displacements of the isolators in the X direction is higher than the one in Y direction and this is evident in all spans except the last two, which have the biggest inclination from the initial and main longitudinal axis of the bridge. The reason for the higher displacement in X direction is that the bridge is stiffer in that direction, hence the isolators are called in to dissipate the earthquake energy by having greater displacement, while in the Y direction the piers are also contributing with their deformation in order to dissipate the earthquake energy. Additionally, there is a gradual (somewhat linear) increase of the average maximum displacement of the isolators with the increase of seismic intensity.

8.2 DAMAGE MODELS

Even though different damage models ought to be adopted for the retrofitted pier with steel, concrete and carbon-fibre jackets, because of the lack of numerical simulation and experimental results regarding this kind of retrofitted piers, it was decided to keep the same damage models as in the as-built piers. The pier parameters are the same, but in reality, the pier jackets will force the piers to be damaged much later. This was a simplifying assumption, but in reality, there will be a slight improvement of the damage functions, hence the results here may be slightly conservative because of this choice.

8.3 FRAGILITY CURVES

The fragility curves were generated in the same way as in the as-built model. The component (piers) fragility curves for each DL are given in the following graph.



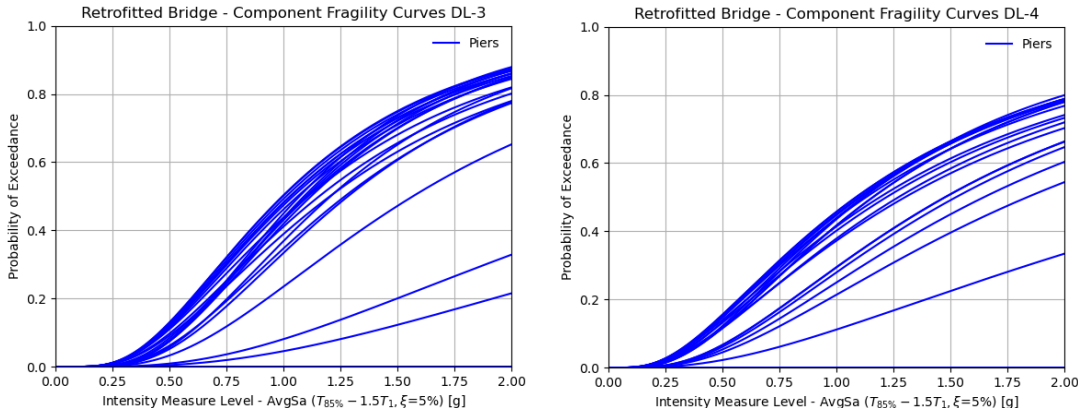


Figure 8.4. Fragility curves of pier components for different damage limits

The global fragility curve of the structure is given in the graph below.

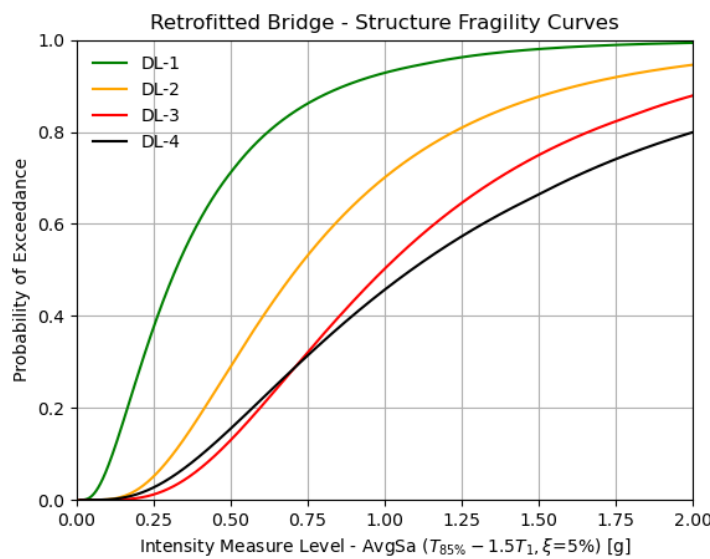


Figure 8.5. Structure fragility curves for different damage limits

Even though the structure fragilities were sensibly decreased with respect to the as-built model, there are still high probabilities of collapse for these intensity levels.

8.4 STRUCTURE LEVEL SEISMIC LOSS ASSESSMENT (DIRECT LOSSES)

The loss curve of the retrofitted structure, calculated with the simplified approach, for the retrofitted structure is shown below.

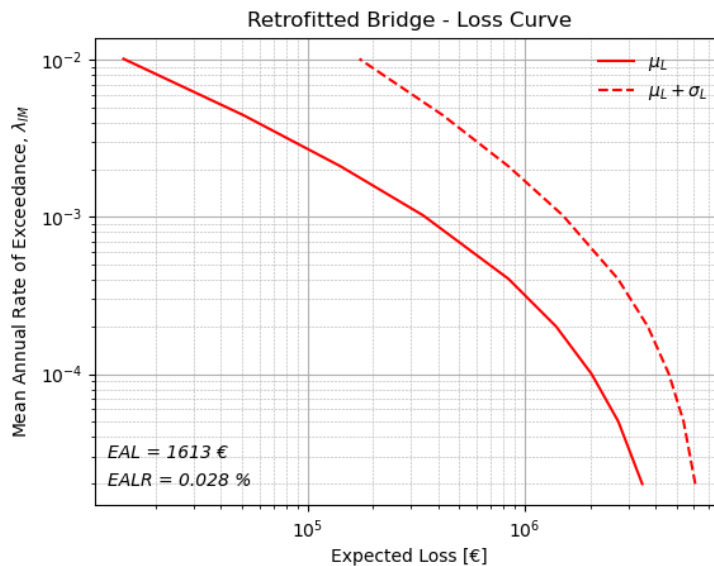


Figure 8.6. Resultant loss curve using simplified approach (HAZUS)

8.5 COMPONENT LEVEL SEISMIC LOSS ASSESSMENT (DIRECT LOSSES)

For each IM level, the distributions of the repair costs were obtained given ‘collapse’ cases, ‘no-collapse’ cases and all cases together. Indicative results for an IM level are shown in Figure 8.7. The distribution of losses (given ‘no-collapse’ cases) between the pier elements is given in Figure 8.8. CDF and CCDF for the repair costs were obtained and given in Figure 8.9. CCDFs obtained for each IM level are depicted in Figure 8.10a. Mean loss versus annual rates of exceedance is illustrated in Figure 8.10b. The loss versus IM level and the annual rate of exceedance versus expected loss graphs were computed and depicted in Figure 8.11.

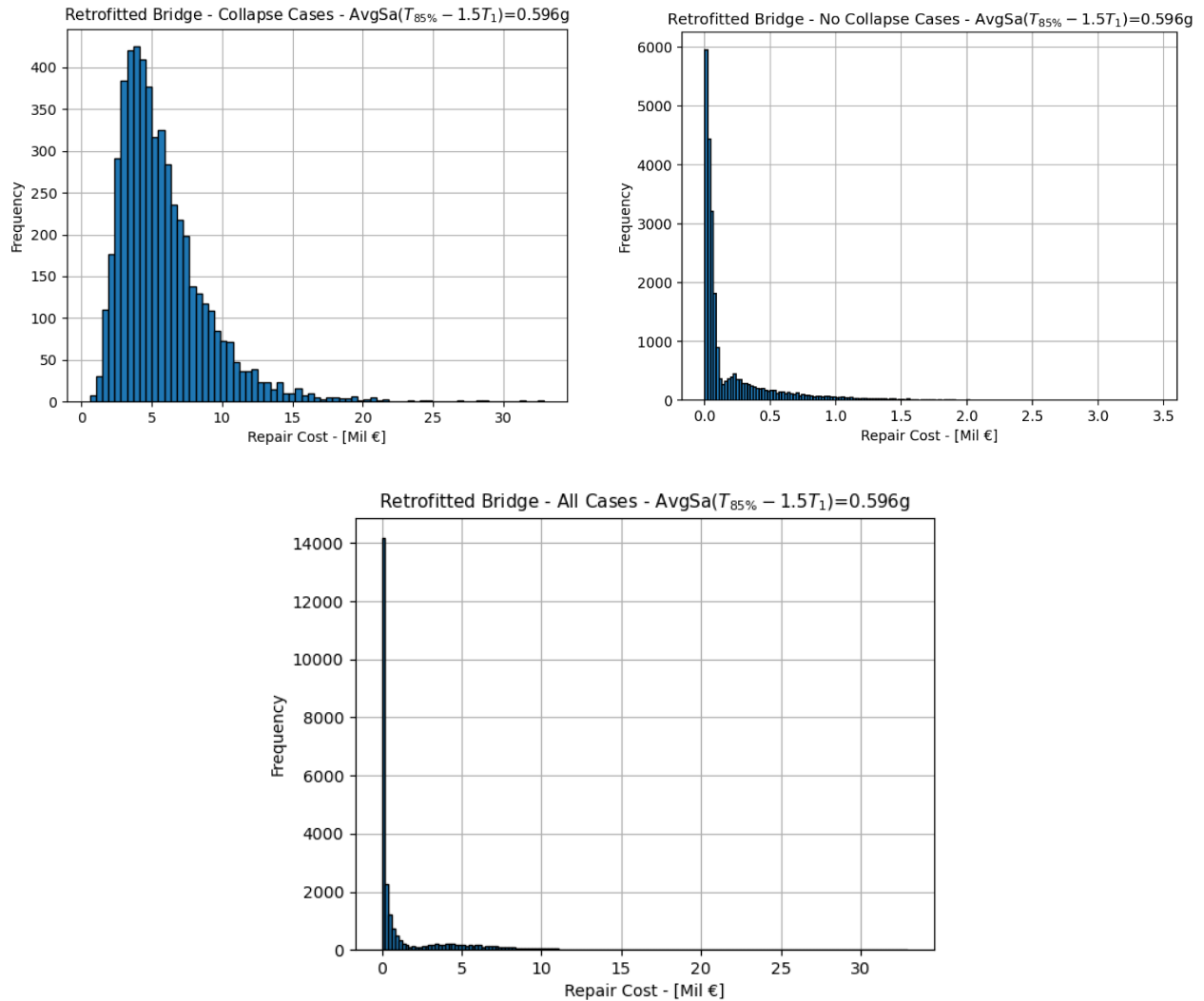


Figure 8.7. Sample loss distribution (a) Collapse cases (b) No Collapse Cases (c) All cases (for $Tr = 4975$ years events)

Figure 8.7 shows that the small repair cost (below 0.5 million €) has the highest occurring frequency. In the ‘collapse’ cases there are higher costs but their frequency is much smaller.

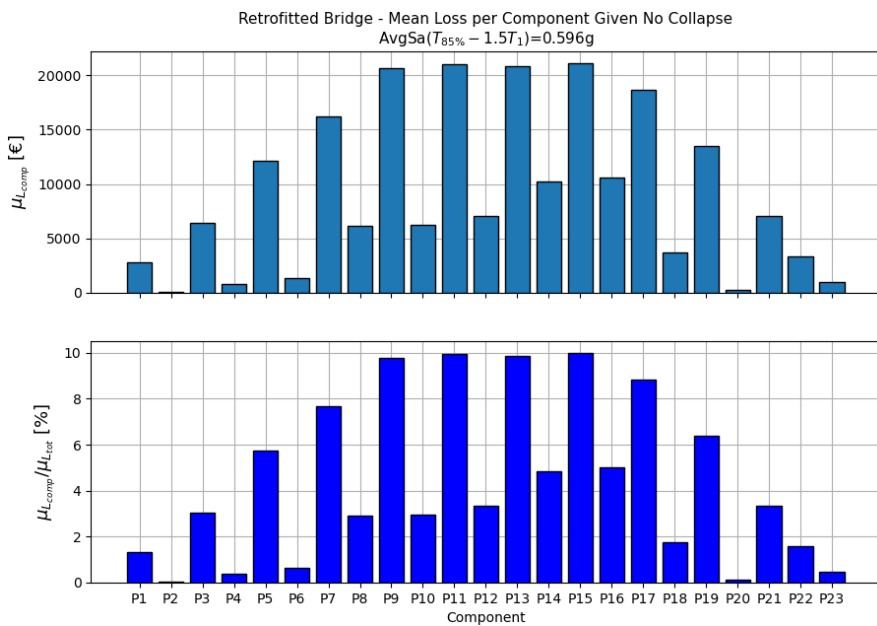


Figure 8.8. Mean loss per component given no collapse (for $Tr = 4975$ years events)

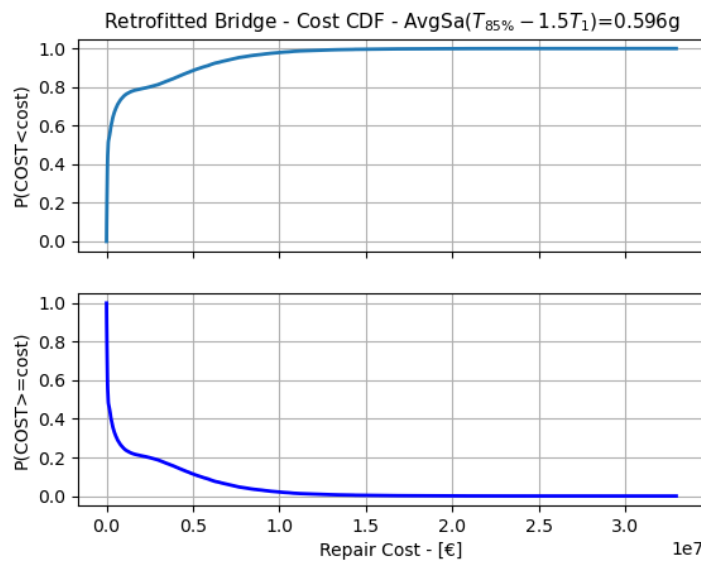


Figure 8.9. Cost CDF and CCDF (for $Tr = 4975$ years events)

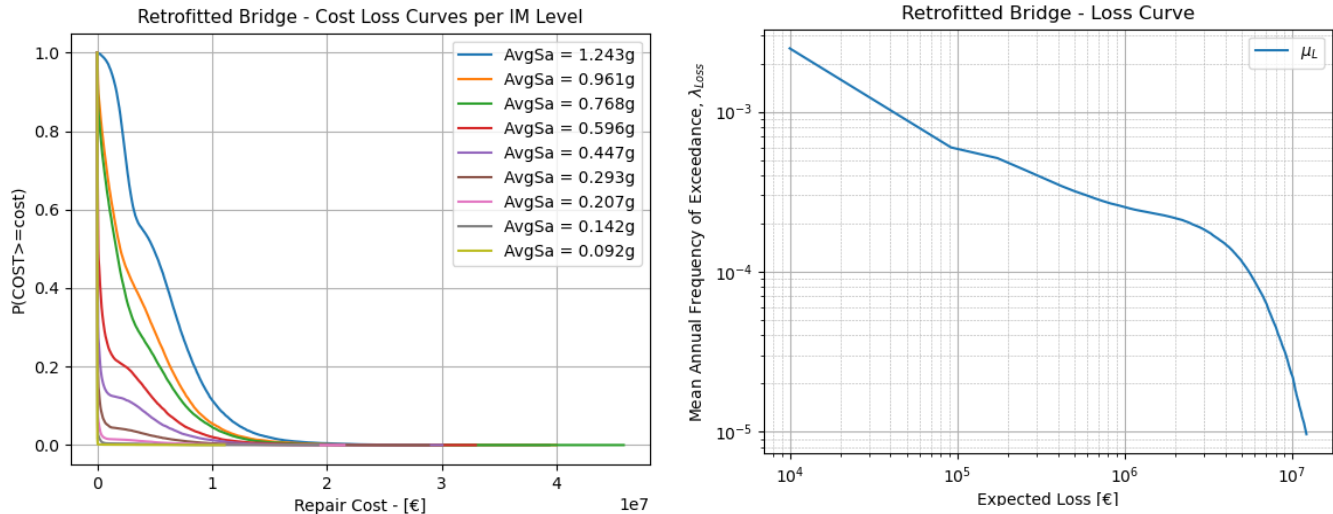


Figure 8.10. Loss curves per IM level and mean loss curve.

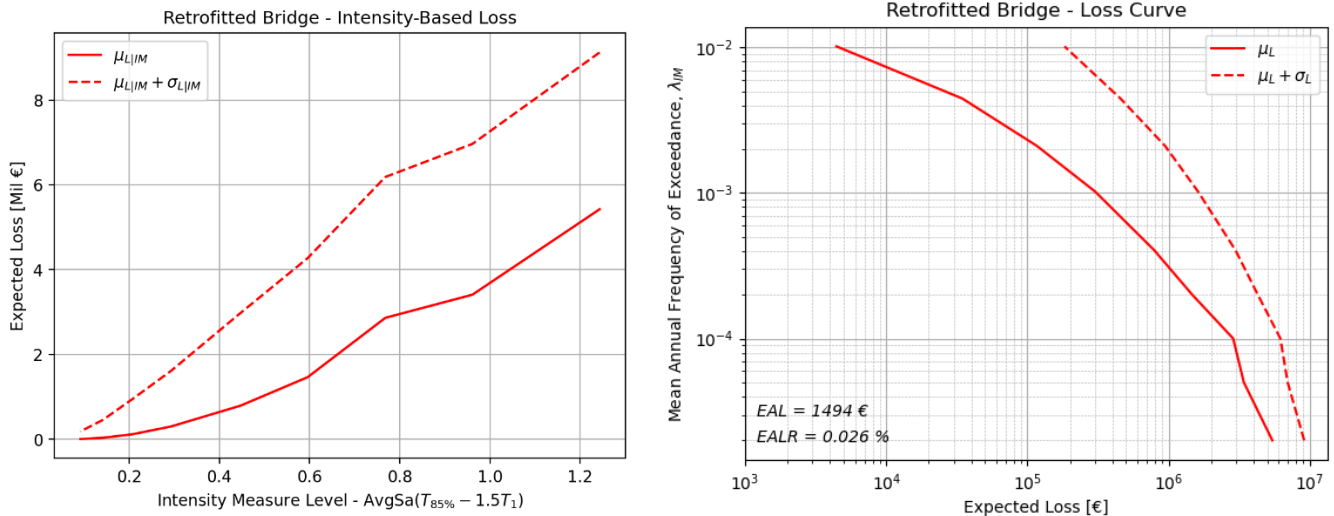


Figure 8.11. Expected intensity-based and time-based losses using the comprehensive approach (FEMA-P58-1, 2018). (a) Loss vs IM level (b) loss curve

8.6 COMPARISON OF SIMPLIFIED AND COMPREHENSIVE LOSS ASSESSMENT APPROACHES

A comparison has been made between simplified (structure-level) and comprehensive (component-based) loss assessment, comparing the intensity-based and time-based loss curves of each approach as shown in Figure 8.12.

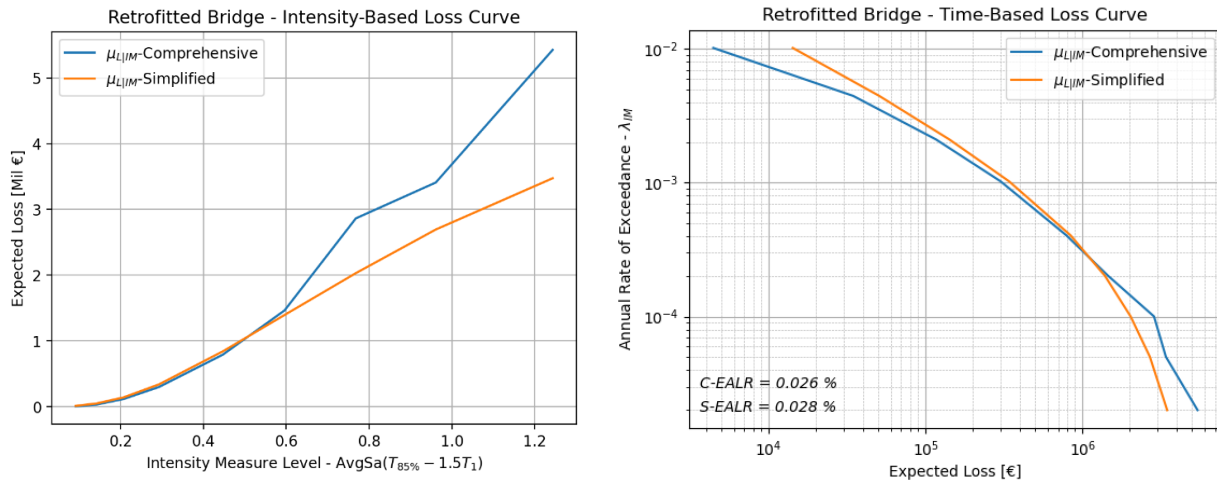


Figure 8.12. Comparison of simplified and comprehensive loss assessment approaches through the intensity-based and time-based loss curves.

The same observations and trends mentioned for the corresponding comparison for the as-built structure (Chapter 7.8), apply also here, with the comprehensive approach estimating more losses in the rare events and less in the more frequent events. Nevertheless, the EALRs obtain from the two approaches are again almost identical.

9. Comparison between as-built and retrofitted model

An indicative comparison of how the structure behaves before and after the retrofit was made for pier element 15, as illustrated in Figure 9.1.

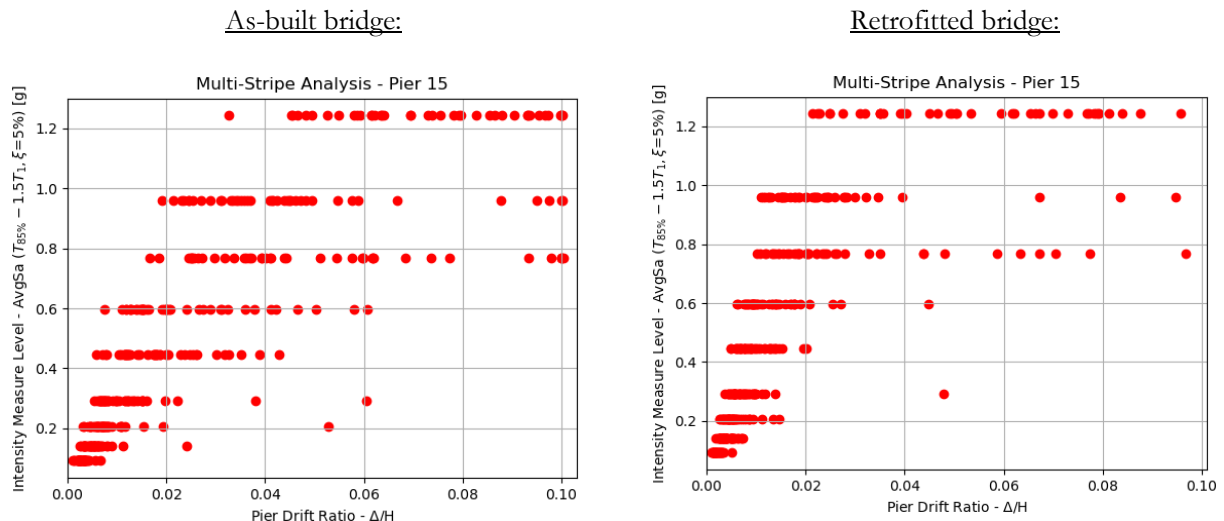


Figure 9.1. Comparison of Pier element 15 peak drift ratios between the as-built and retrofitted model

The drastic change in pier element response is evident. The dispersion in the pier response, among the different ground motion sets of certain intensity and was more contained.

The comparison between the EALR for the as-built and retrofitted models is given in Table 9.1.

Table 9.1. Comparison of Expected Annual Loss Ratio between the As-Built and Retrofitted model.

	Bridge Model	As-built	Retrofitted
Approach	Comprehensive	0.077%	0.026%
	Simplified	0.076%	0.028%

The ratio of expected annual losses of retrofitted motel to as-built model is 0.34 with the comprehensive approach and 0.37 with the simplified approach. That means that with all the interventions that were considered, the initial losses were reduced by about 1/3.

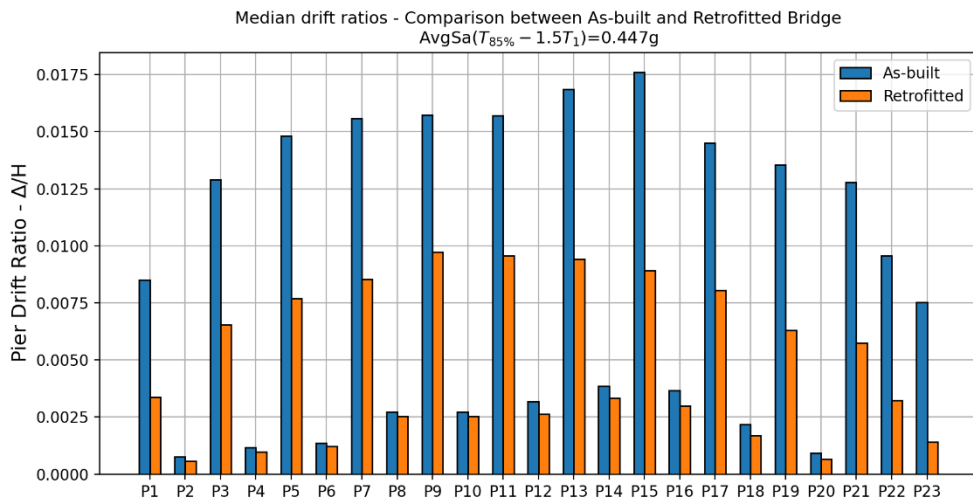


Figure 9.2 Comparison of the median drift ratios of each pier between the retrofitted and as-built structure for an IM level.

From Figure 9.2 it can be seen that the median drift ratios in the critical piers were almost halved with the introduction of the retrofitting schemes. In the lower (non-crucial) pier elements. This is for an indicative IM level, the rest of the IM levels are located in the end of Appendix C.

Figure 9.3 depicts the lower loss curves of the retrofitted model. Additionally, the trend of the loss curve obtained from the simplified compared to the comprehensive approach seems to coincide for both models.

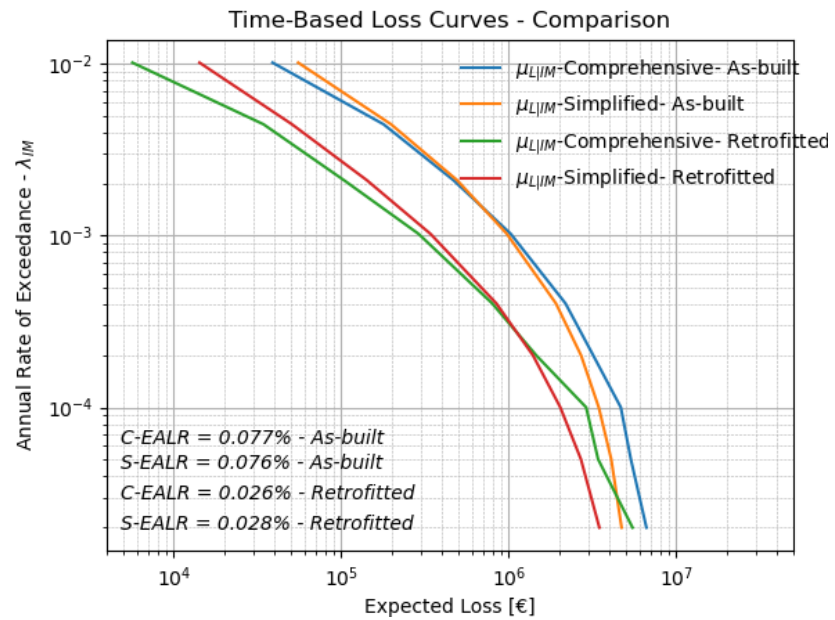


Figure 9.3 Loss curves from comprehensive and simplified approach crossed with the as-built and retrofitted model.

10. Discussion and Conclusions

Two different frameworks (HAZUS and FEMA P-58-1) to estimate the direct seismic losses for bridge structures were explored. It was generally observed that the FEMA P-58-1 (comprehensive) approach estimates slightly lower losses in the lower intensity levels, as compared with the HAZUS (simplified) approach. The inverse is happening for the higher intensity levels. It should be noted that with the inclusion of different damageable components (abutments, bearings etc.), the above statement might change.

A detailed model was generated in OpenSeesPy software for the RC bridge, with in-plane and out-of-plane curvature. It is worth mentioning that the estimated losses are influenced by the modelling approach used. Although not explored in this study, the influence of soil-foundation-structure Interaction and more detailed modelling of other structural components might play a significant role. A set of scripts, written in the Python programming language, were used to model, analyse and estimate the bridge's replacement costs, along with the mean repair costs of the piers and abutments. The assumptions made to estimate the bridge and its components costs can be further refined by various inputs from practitioners.

It was of extreme importance to achieve hazard consistency in order to analyse properly the time-based loss assessment of the irregular bridge at hand, therefore the conditional spectrum (CS) approach for the bidirectional ground motion selection was used. The orientation independent geometric mean of the two ground motion components was used as a criterion for the spectrum matching. The average spectral acceleration (AvgSa) over a period range was chosen as the intensity measure, due to the sparse distribution of the modal mass participation factor throughout the modes of the model (bridge irregularity).

The seismic loss assessment framework presented herein can be used as a benchmark for simplified assessment procedures or potential design frameworks. More details can be integrated into the procedure and models, in order to have an even more accurate depiction of the performance of the bridge.

Three main interventions were performed in the bridge structure: (a) deck made continuous, (b) the metallic bearings were replaced with friction pendulum isolators and (c) the piers were strengthened with concrete, steel and carbon-fibre jacketing. All the interventions have improved the bridge's performance, but the one with the most impact was the isolators, which dissipated the seismic energy with their big displacements and unburdened the piers from heavy non-linear deformations. Also, the lateral force resisting behaviour of the bridge became more simple, clear and homogeneous. Nevertheless, it should be stated again that the inclusions of the bearings in the component-based loss

assessment method, might further increase the difference in EALR between the pre- and post-retrofitting conditions. The initial metallic bearings, are more prone to damage, due to the locking that they might undergo, and also the high amount of hysteresis cycles induced to the pins can weaken them and cause their fracture. Whereas, the inverted friction pendulums will not be significantly damaged, since they also possess recentering capabilities, as long as they don't exceed their prescribed maximum displacement.

The piers strengthening interventions practiced in the bridge (i.e. concrete, steel and carbon-fibre jacketing) had the benefits of: (1) improvement of the post-peak behaviour in the moment-curvature ($M-\varphi$) analyses and subsequently in the pushover analyses of the piers and (2) increase of shear strength of the piers. The only downside of these interventions was the slight decrease of curvature (and thus displacement) ductility, since it's the steel fracture that governs the ultimate curvature (displacement) of the piers and by increasing the concrete strength, ultimate stress and ultimate strain doesn't help the overall flexural ductility of the column.

Observing the expected annual losses and the losses in general, which were very low in value, one may conclude that the retrofit of the bridge was excessive from a seismic resilience perspective. Nonetheless, to have a well-rounded understanding whether the retrofit was necessary or not, the losses associated with the loss of functionality of the bridge (indirect losses) need to be addressed. The indirect losses could easily overshadow the direct ones in this kind of bridges. Hence, since the bridges are designed, so that they can withstand very high demands with little or no damage, throughout their life span, possibly the EALR solely for direct losses is not a good metric of the performance of bridges, because it gives such a low and insignificant value compared to other parameters.

11. Possible Future Developments

A list with some possible future developments of the current work is given as follows.

- EALR values for bridge structures are relatively low when only direct seismic losses are considered. Indirect losses most probably will have much higher contribution to the losses (especially for crucial transportation links), so this is important to be considered in future studies. They can be implemented by firstly assuming some simplified parameters for the transportation network and the time required to complete each repair activity and to reconstruct the bridge.
- Damages in other components of the structure. In the literature, no suitable damage models for the bearings were found. In the future something simplified can be adopted. Damage models proposed for some kinds of bearing elements and abutments are available in the literature and can be used for loss assessment purposes. In this study, damage models for the expansion joints and shear keys were not explored, and thus considered as non-damageable components, but their contribution to the overall losses could be significant.
- Time-dependent effects and deterioration of the bridge through time could be studied to investigate their impacts on the seismic vulnerability of the bridge.
- It should be noted that the same damage models and consequence functions, with the as-built piers, were also used for the retrofitted piers, which is not correct because the retrofitted piers will enter into different damage states for different levels of EDPs. Also, the repair actions and costs of each damage state will differ. Several studies have been conducted for the damages and capacities of this kind of retrofitted columns in the literature [Ozcan & Binici, 2020]. However, this is a simplification adopted for the current study and going into these details will derail the work from its scope.
- After some more polishing of the loss estimation process defined here, its application to a portfolio of bridges could be made possible, in order identify key parameters that contribute more significantly to the losses.

REFERENCES

- ANAS S.p.A. (2018). *Nuove Costruzioni – Manutenzione Straordinaria*. (Direzione Ingegneria e Verifiche) Retrieved from ELENCO PREZZI 2020 (in Italian): <https://www.stradeanas.it/it/elenco-prezzi>
- ASCE/SEI 7-10. (2010). *Minimum Design Loads for Buildings and Other Structures*. American Society of Civil Engineers.
- Baker, J. W. (2011). Conditional Mean Spectrum: Tool for ground motion selection. *Journal of Structural Engineering*, 137(3), 322-331. doi:10.1061/(ASCE)ST.1943-541X.0000215
- Baker, J. W., & Cornell, A. C. (2006, May). Which Spectral Acceleration Are You Using? *Earthquake Spectra*, 22(2), 293-312.
- Baker, J., & Jayaram, N. (2008, February). Correlation of Spectral Acceleration Values from NGA Ground Motion Models. *Earthquake Spectra*, 24(1), 299-317. doi:10.1193/1.2857544
- Boore, D., & Atkinson, G. (2008, February). Ground-Motion Prediction Equations for the Average Horizontal Component of PGA, PGV, and 5%-Damped PSA at Spectral Periods between 0.01s and 10.0s. *Earthquake Spectra*, 24(1), 99-138. doi:10.1193/1.2830434
- Caltrans. (2019). *Seismic Design Criteria, version 2.0*. State of California, Department of Transportation.
- Chiou, B., Darragh, R., Gregor, N., & Silva, W. (2008). NGA Project Strong-Motion Database. *Earthquake Spectra*, 24(1), 23-44.
- ETH Zurich/Swiss Seismological Service. (2017). *European Facilities for Earthquake Hazard and Risk (EFEHR)*. Retrieved from Hazard Maps: <http://www.efehr.org/en/hazard-data-access/hazard-maps/>

- European Committee for Standardization CEN. (2004, December). Eurocode 8: Design of structures for earthquake resistance - Part 1: General rules, seismic actions and rules for buildings. *EN 1998-1:2004*. Brussels.
- Federal Emergency Management Agency (FEMA). (2003). *Multi-hazard loss estimation methodology - Earthquake Model*. Washington, D.C., USA: HAZUS.
- Federal Emergency Management Agency (FEMA). (2018). *Seismic Performance Assessment of Buildings, Volume 1 - Methodology*. Washington, D.C.
- GEM. (2020). *The OpenQuake-engine User Manual*. Global Earthquake Model (GEM) OpenQuake Manual for Engine version 3.9.0. doi:10.13117/GEM.OPENQUAKE.MAN.ENGINE.3.9.0
- Kameshwar, S., & Padgett, J. E. (2017). Characterizing and Predicting Seismic Repair Costs for Bridges. *Journal of Bridge Engineering*, 22(11).
- Kohrangi, M., Bazzuro, P., Vamvatsikos, D., & Spillatura, A. (2017). Conditional spectrum-based ground motion record selection using average spectral acceleration. *Earthquake Engineering & Structural Dynamics*. doi:10.1002/eqe.2876
- Kowalsky, M. J., & Priestley, M. N. (2000, June). Improved Analytical Model for Shear Strength of Circular Reinforced Concrete Columns in Seismic Regions. *ACI Structural Journal*, 97(3), 388-396.
- Krawinkler, H., Zareian, F., Medina, R. A., & Ibarra, L. F. (2006). Decision support for conceptual performance-based design. *Earthquake Engineering and Structural Dynamics*, 35, 115-133.
- Lin, T., Haselton, C. B., & Baker, J. W. (2013). Conditional spectrum-based ground motion selection. Part I: Hazard consistency for risk-based assessments. *Earthquake Engineering & Structural Dynamics*, 42, 1847-1865. doi:10.1002/eqe.2301
- Lin, T., Haselton, C. B., & Baker, J. W. (2013). Conditional-Spectrum-based ground motion selection. Part II: Intensity-based assessments and evaluation of alternative target spectra. *Earthquake Engineering & Structural Dynamics*. doi:10.1002/eqe.2303
- Mackie, K. R., & Stojadinovic, B. (2005). Comparison of Incremental Dynamic, Cloud, and Stripe Methods for Computing Probabilistic Seismic Demand Models. *Structures Congress*. New York, United States: American Society of Civil Engineers.

- Mander, J. B., Priestley, M. J., & Park, R. (1988). Theoretical Stress-Strain Model for Confined Concrete. *Journal of Structural Engineering*, 114, 1804-1826.
- MAPEI S.p.A. (2019). *MAPEWRAP C UNI-AX SYSTEM*. Retrieved from CERTIFICATO DI VALUTAZIONE TECNICA: <https://www.mapei.com/it/en/mapewrap-c-uni-ax-system>
- Nielson, B. G., & DesRoches, R. (2007). Analytical Seismic Fragility Curves for Typical Bridges in the Central and Southeastern United States. *Earthquake Spectra*, 23(3), 615-633.
- Olmos, B., Jara, J. M., Gómez, G., & Martínez, G. (2019). Influence of steel jacket thickness on the RC bridges' seismic vulnerability. *Journal of Traffic and Transportation Engineering*, 15-34.
- O'Reilly, G. J. (2020). Seismic Intensity Measures for the Risk Assessment of Bridges. *Engineering Structures (Accepted with Revisions)*.
- O'Reilly, G. J., & Calvi, G. M. (2018). Conceptual seismic design in performance-based earthquake engineering. *Earthquake Engineering Structural Dynamics*, 1-23.
- O'Reilly, G. J., Monteiro, R., Nafeh, A. B., Sullivan, T. J., & Calvi, G. M. (2020). Displacement-Based Framework for Simplified Seismic Loss Assessment. *Journal of Earthquake Engineering*, 24, 1-22.
- Ozcan, O., & Binici, B. (2020). A Drift Capacity Prediction Model for Retrofitted Reinforced Concrete Columns. *Magazine of Concrete Research*, 1-41.
- Perdomo, C., & Monteiro, R. (2020). Simplified damage models for circular section reinforced concrete bridge columns. *Engineering Structures*, 217, 1-20.
- Priestley, N., Seible, F., & Calvi, G. M. (1996). *Seismic Design and Retrofit of Bridges*. USA: John Wiley & Sons, Inc.
- Seible, F., Priestley, M. N., Hegemier, G. A., & Innamorato, D. (1997). Seismic Retrofit of RC Columns with Continuous Carbon Fiber Jackets. *Journal of Composites for Construction*, 1(2), 52-62.
- University of California, Berkeley. (2006). *OpenSees*. Retrieved from OpenSeesWiki: <https://opensees.berkeley.edu/index.php>

Yang, T., Moehle, J. P., Stojadinovic, B., & Kiureghian, A. D. (2006). An application of the PEER performance-based earthquake engineering methodology. *Proceedings of the 8th U.S. National Conference on Earthquake Engineering*. San Francisco, California, USA.

Yang, T., Moehle, J. P., Stojadinovic, B., & Kiureghian, A. D. (2009). Seismic Performance Evaluation of Facilities: Methodology and Implementation. *Journal of Structural Engineering*, 135(10), 1146-1154.

Zanini, M. A., Faleschini, F., & Pellegrino, C. (2016). Cost analysis for maintenance and seismic retrofit of existing bridges. *Structure and Infrastructure Engineering*, 12(11), 1411-1427. doi:10.1080/15732479.2015.1133661

APPENDIX A. Miscellaneous bridge characteristics

Table A.1. Modal Periods, Damping and Modal Mass Participating Factors

Mode	T [sec]	ξ [%]	MPx [%]	MPy [%]	MPz [%]	Σ MPx [%]	Σ MPy [%]	Σ MPz [%]
1	1.56	2	0.5	29.67	0	0.5	29.67	0
2	1.465	1.98	4.01	5.1	0	4.51	34.77	0
3	1.427	1.98	4.21	1.33	0	8.72	36.1	0
4	1.42	1.98	9.26	0.03	0	17.98	36.13	0
5	1.381	1.98	0.87	6.16	0	18.85	42.28	0
6	1.319	1.98	1.98	2.74	0	20.84	45.02	0
7	1.295	1.98	4.65	0.02	0	25.49	45.04	0
8	1.279	1.98	0.04	3.08	0	25.53	48.12	0
9	1.276	1.98	8.01	1.34	0	33.54	49.46	0
10	1.236	1.98	6.14	0.01	0	39.67	49.47	0
11	1.229	1.98	4.95	0.67	0	44.62	50.14	0
12	1.222	1.99	0.07	5.43	0	44.69	55.57	0
13	1.207	1.99	10.96	3.32	0	55.65	58.89	0
14	1.169	2	0	0.61	0	55.65	59.5	0
15	1.15	2	3.71	1.06	0	59.37	60.56	0
16	1.105	2.01	0	0.57	0	59.37	61.13	0
17	1.087	2.02	0	0.32	0	59.37	61.46	0
18	1.002	2.06	3.95	0.38	0	63.33	61.84	0
19	0.964	2.09	5.22	0.08	0	68.54	61.92	0
20	0.943	2.1	0.11	2.94	0	68.66	64.86	0
21	0.865	2.17	0.46	3.94	0	69.12	68.79	0
22	0.809	2.23	1.15	0.29	0	70.26	69.08	0
23	0.803	2.24	0.22	0	0	70.48	69.08	0
24	0.708	2.39	1.47	1.79	0	71.95	70.87	0
25	0.701	2.41	0.86	1.69	0	72.81	72.56	0
26	0.67	2.47	4.36	0	0	77.18	72.56	0
27	0.636	2.55	0.89	0.05	0	78.06	72.61	0
28	0.615	2.61	0	0	0	78.06	72.61	0
29	0.614	2.61	0	0	0	78.06	72.61	0
30	0.614	2.61	0	0	0	78.06	72.61	0
31	0.613	2.61	0.54	1.35	0	78.6	73.96	0

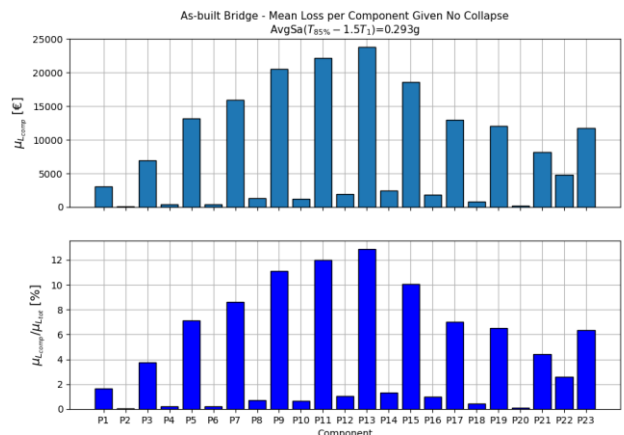
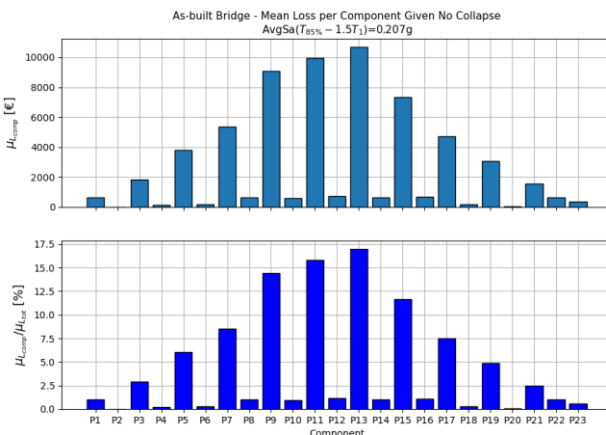
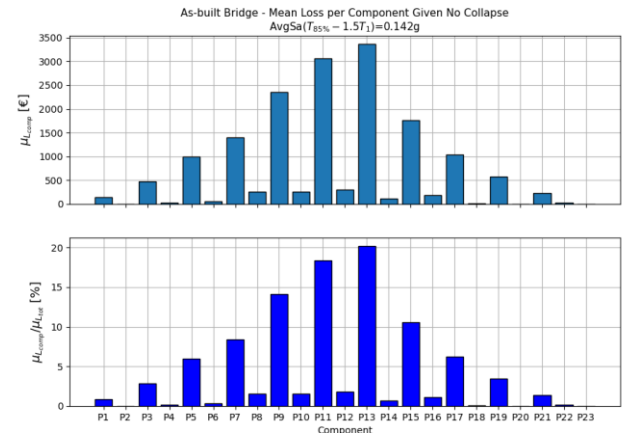
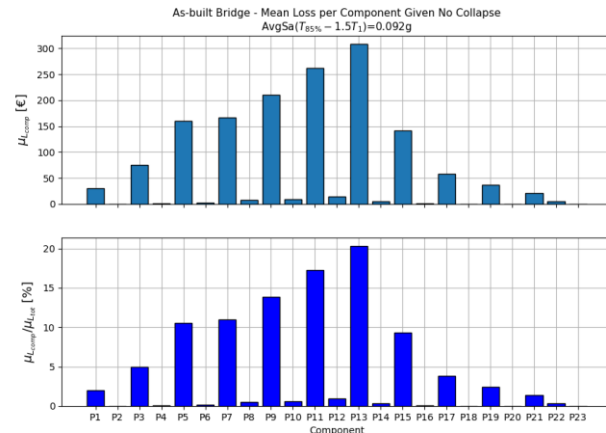
32	0.613	2.61	0.03	0.02	0	78.62	73.98	0
33	0.611	2.62	0	0.15	0	78.62	74.13	0
34	0.611	2.62	0	1.79	0	78.62	75.92	0
35	0.61	2.62	0	0	0	78.63	75.92	0
36	0.61	2.62	0	0.07	0	78.63	75.99	0
37	0.609	2.62	0	0.06	0	78.63	76.04	0
38	0.609	2.62	0	0	0	78.63	76.05	0
39	0.609	2.63	0	0	0	78.63	76.05	0
40	0.607	2.63	0.01	0.14	0	78.64	76.19	0
41	0.606	2.63	0	0	0	78.64	76.19	0
42	0.605	2.64	0.01	0	0	78.64	76.19	0
43	0.361	3.93	0.18	0.02	0	78.83	76.21	0
44	0.293	4.73	0.24	0.93	0	79.06	77.14	0
45	0.292	4.75	0.01	0.02	0	79.07	77.17	0
46	0.285	4.86	0.38	0.28	0	79.46	77.45	0
47	0.282	4.91	0.09	0.53	0	79.54	77.97	0
48	0.281	4.92	0.03	0	0	79.57	77.98	0
49	0.279	4.96	0.1	0.04	0	79.66	78.02	0
50	0.277	4.98	0.17	0.17	0	79.83	78.18	0
51	0.274	5.04	0.01	0.01	0	79.84	78.19	0
52	0.273	5.04	0.03	0.01	0	79.87	78.2	0
53	0.269	5.12	0	0.22	0	79.87	78.42	0
54	0.268	5.14	0.19	0	0	80.06	78.42	0
55	0.267	5.16	0.13	0	0	80.19	78.42	0
56	0.264	5.2	0	0.02	0	80.19	78.44	0
57	0.264	5.21	0.01	0.16	0	80.2	78.6	0
58	0.264	5.22	0.13	0	0	80.34	78.6	0
59	0.26	5.28	0	0.02	0	80.34	78.62	0
60	0.258	5.33	0.44	0.04	0	80.78	78.66	0
61	0.257	5.34	0.42	0.02	0	81.2	78.68	0
62	0.252	5.44	0.01	0.06	0	81.22	78.74	0
63	0.23	5.92	0	0.11	0	81.22	78.84	0
64	0.227	6	0.26	0	0	81.48	78.84	0
65	0.212	6.41	0.03	0.08	0.01	81.51	78.92	0.01
66	0.202	6.69	0.29	0.09	0	81.8	79.02	0.01
67	0.191	7.09	0.24	3.46	0.06	82.04	82.47	0.07
68	0.18	7.48	0	0.05	0	82.04	82.52	0.07
69	0.166	8.08	1.48	0.13	0	83.51	82.65	0.07
70	0.163	8.24	1.56	0.16	0	85.08	82.81	0.08
71	0.162	8.27	0.01	0.05	0.04	85.09	82.86	0.12
72	0.161	8.33	0.05	2.28	0.2	85.14	85.14	0.31
73	0.154	8.7	0	1.03	0.13	85.14	86.17	0.45

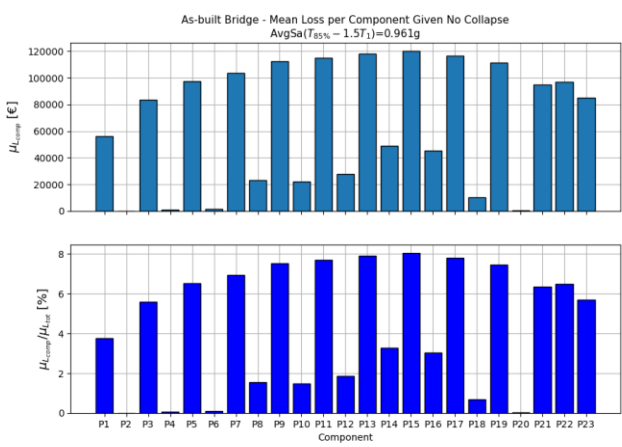
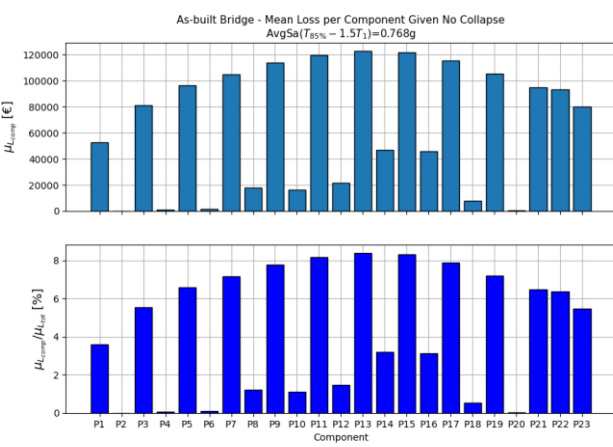
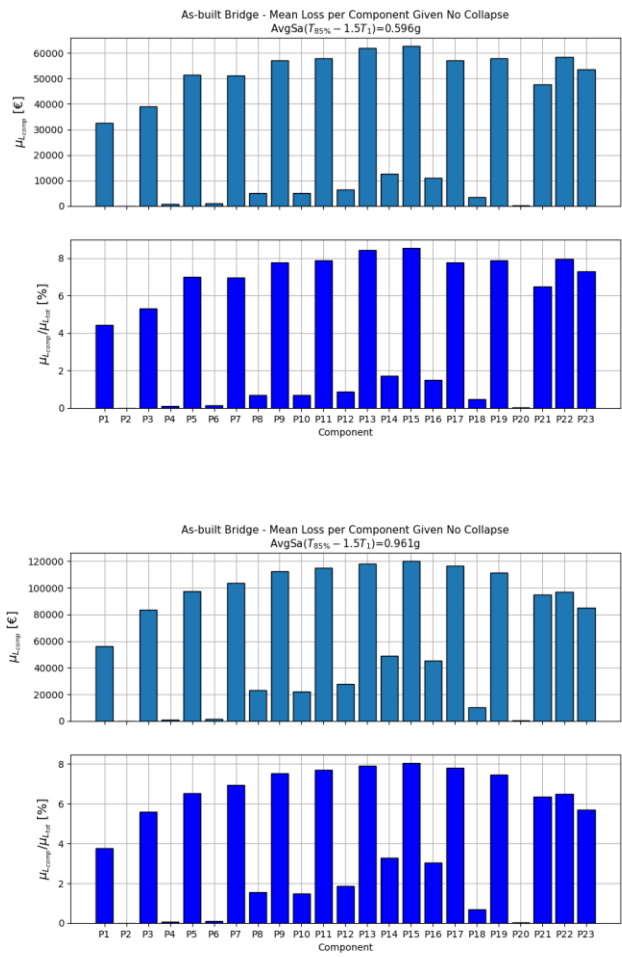
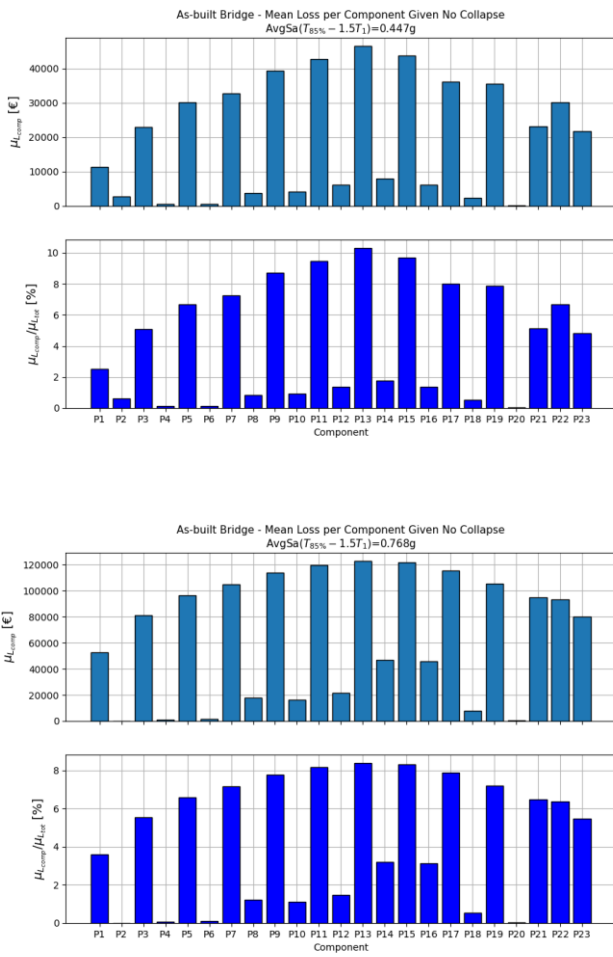
74	0.146	9.17	0	0.01	0	85.14	86.18	0.45
75	0.131	10.17	0.14	0.8	0.67	85.28	86.98	1.12
76	0.131	10.23	1.65	0.03	0	86.93	87.01	1.12
77	0.13	10.27	0	0.79	1.19	86.93	87.8	2.31
78	0.13	10.3	0.44	0.14	0	87.36	87.93	2.31
79	0.125	10.69	0	0.09	0.13	87.36	88.02	2.44
80	0.122	10.93	0.02	0.07	0.3	87.38	88.09	2.73
81	0.122	10.96	0.44	0.14	0	87.83	88.23	2.73
82	0.121	11.08	0	0.07	0.21	87.83	88.29	2.94
83	0.12	11.17	0	0	0	87.83	88.3	2.94
84	0.119	11.18	0.72	0	0	88.55	88.3	2.94
85	0.119	11.19	0	0	0	88.55	88.3	2.94
86	0.119	11.21	0.22	0	0	88.77	88.3	2.94
87	0.117	11.41	0.81	0	0	89.59	88.3	2.94
88	0.117	11.41	0.27	0	0	89.86	88.3	2.94
89	0.117	11.43	0	0	0	89.86	88.3	2.94
90	0.116	11.5	0	0	0	89.86	88.3	2.94
91	0.116	11.52	0	0	0	89.86	88.3	2.94
92	0.116	11.54	1.44	0	0	91.3	88.3	2.94
93	0.114	11.72	0.03	0	0	91.34	88.3	2.94
94	0.113	11.82	0	0	0	91.34	88.3	2.94
95	0.109	12.25	0.04	0.55	3.91	91.38	88.86	6.85
96	0.109	12.26	0	0	0	91.38	88.86	6.85
97	0.107	12.44	0	0.01	0.03	91.38	88.86	6.88
98	0.107	12.47	0	0.23	0.89	91.38	89.09	7.78
99	0.106	12.55	0.33	0	0	91.71	89.09	7.78
100	0.104	12.82	0	0	0	91.72	89.09	7.78

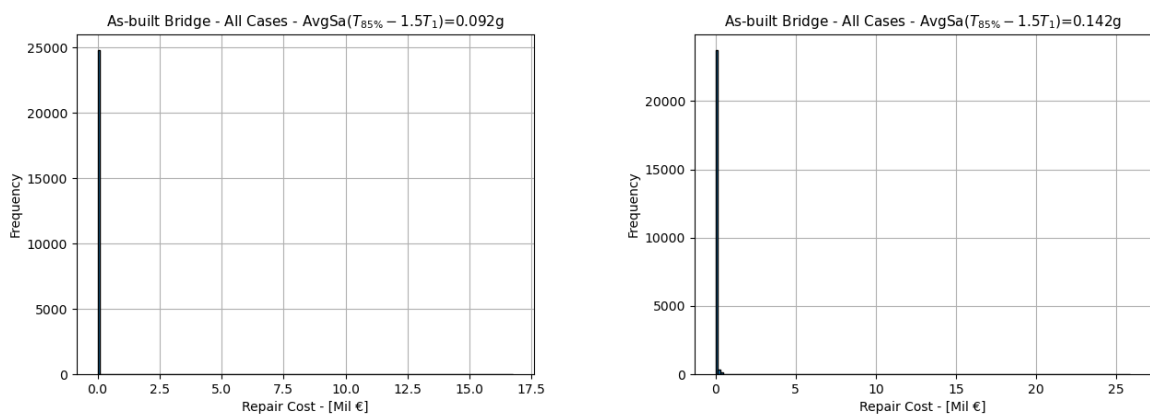
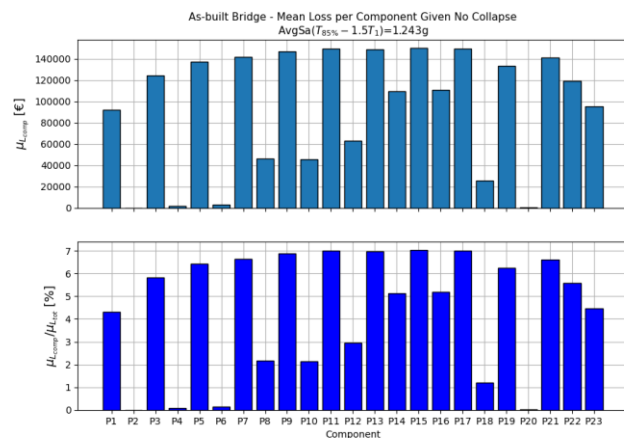
Table A.2. Mean repair cost of pier components at each damage state

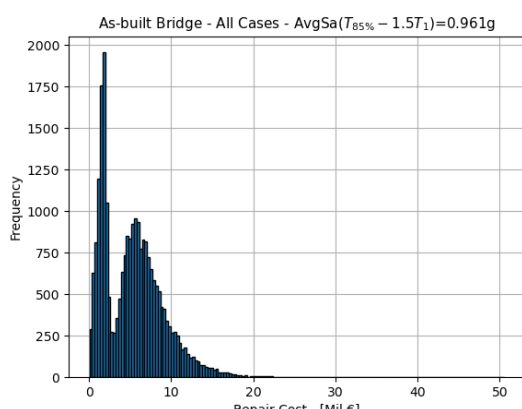
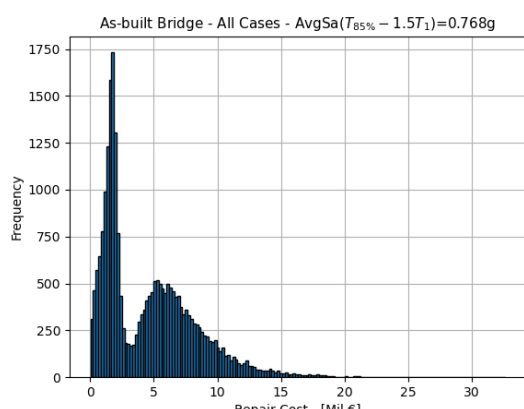
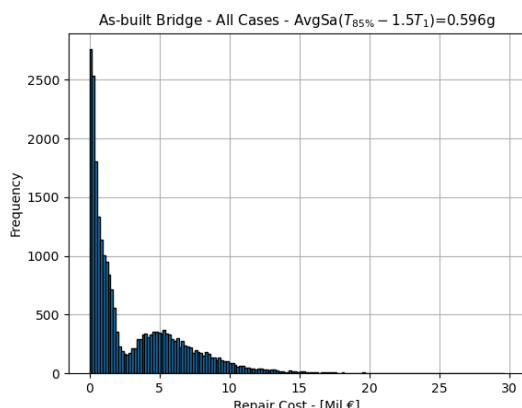
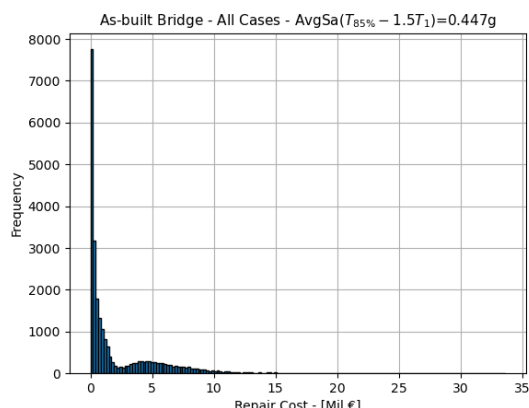
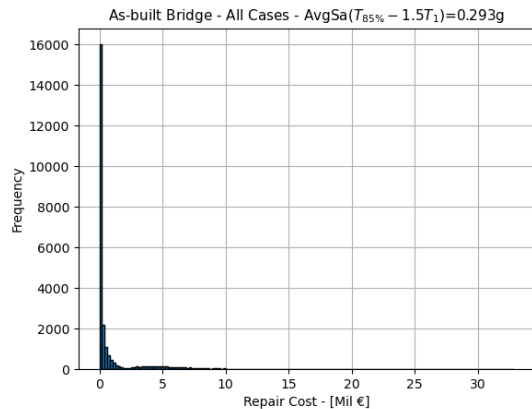
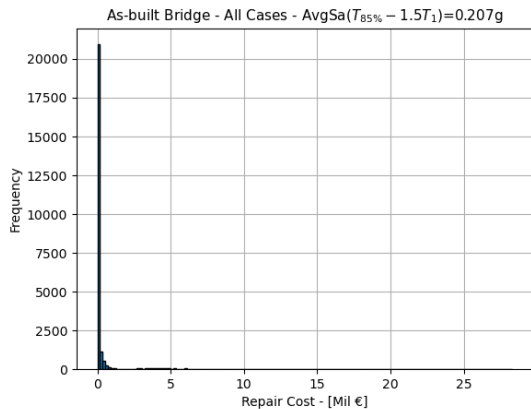
Pier Element No	Mean Repair Costs (€)		
	DS-1	DS-2	DS-3
1	3588	10772	140819
2	5520	8079	124958
3	3588	11514	156959
4	5520	11686	149956
5	3588	11514	156959
6	5520	13084	159652
7	3588	11514	156959
8	5520	21586	218562
9	3588	11514	156959
10	5520	21402	217271
11	3588	11514	156956
12	5520	22331	229890
13	3588	11514	156950
14	5520	23233	260444
15	3588	11514	157683
16	5520	23285	262107
17	3588	11514	157680
18	5520	17758	192007
19	3588	10853	142505
20	5520	9201	132721
21	3588	11514	156945
22	3588	10264	129668
23	3588	8474	104246

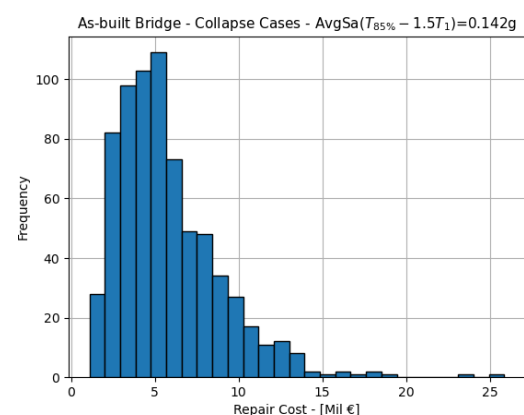
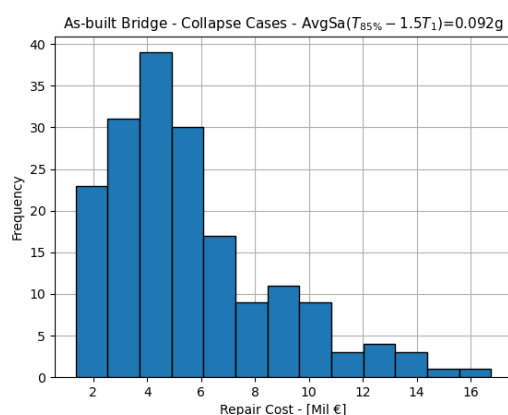
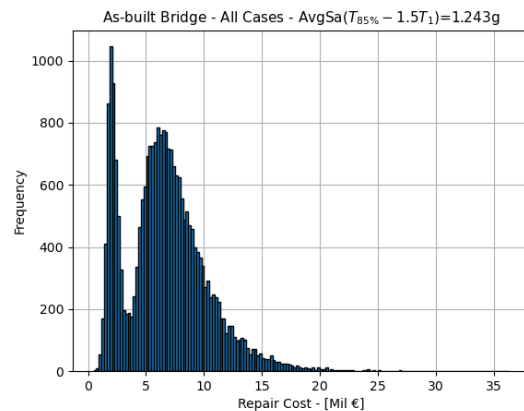
APPENDIX B. Direct Loss Assessment and Structural Analysis Results of the As-Built Bridge

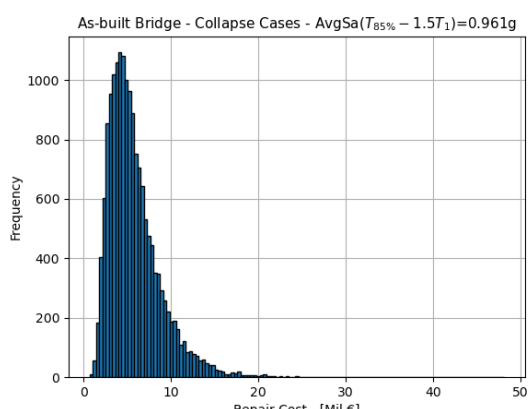
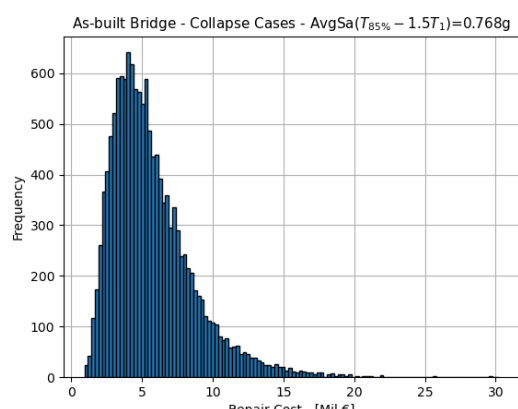
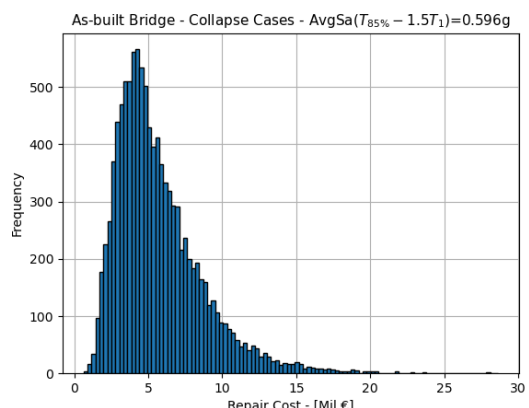
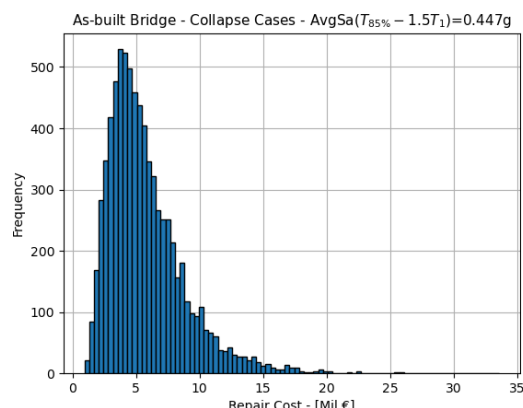
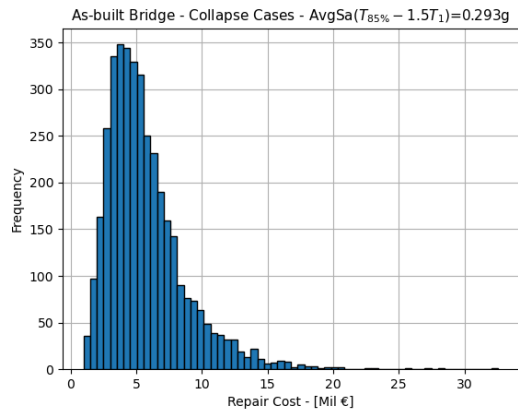
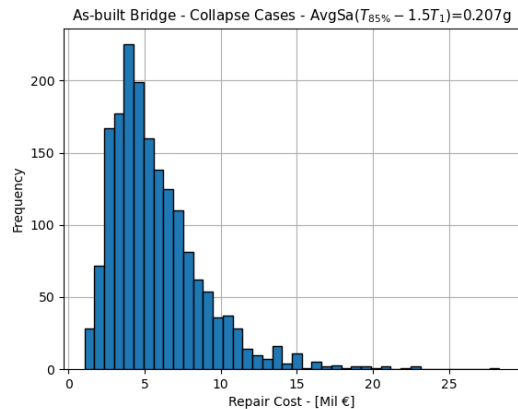


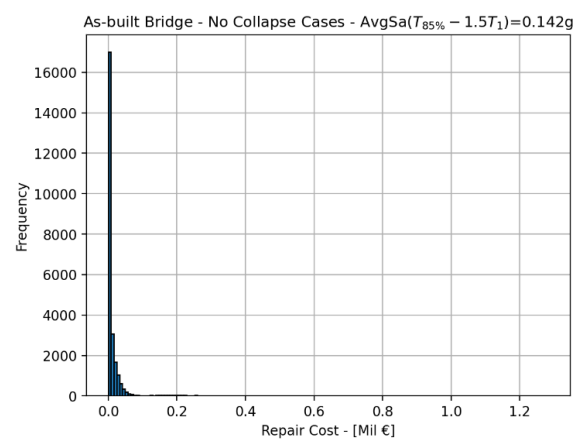
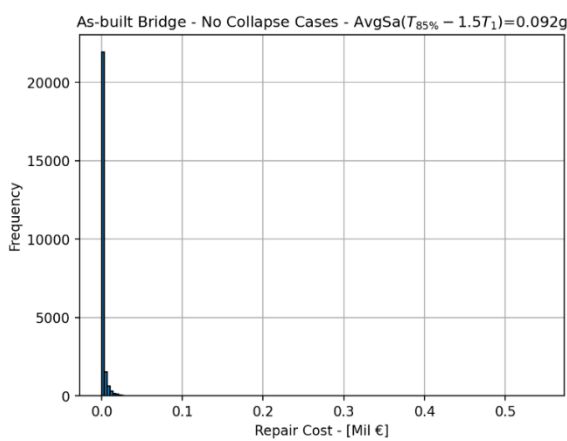
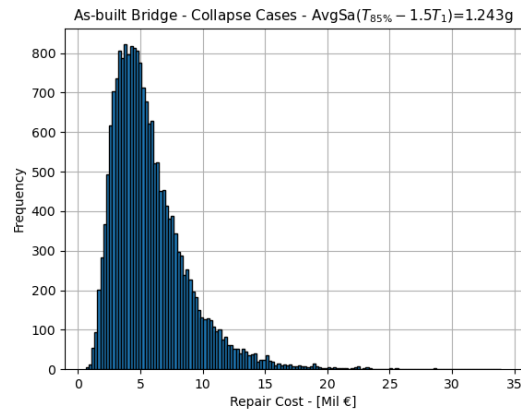


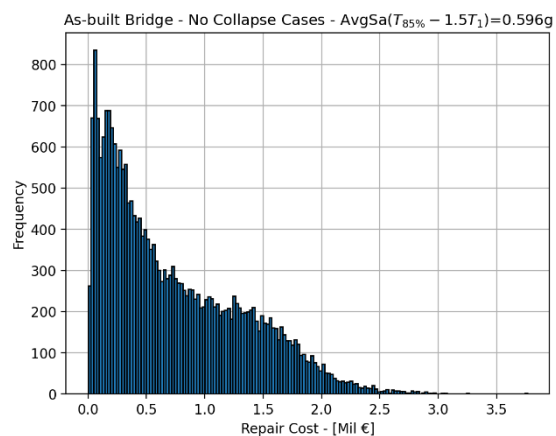
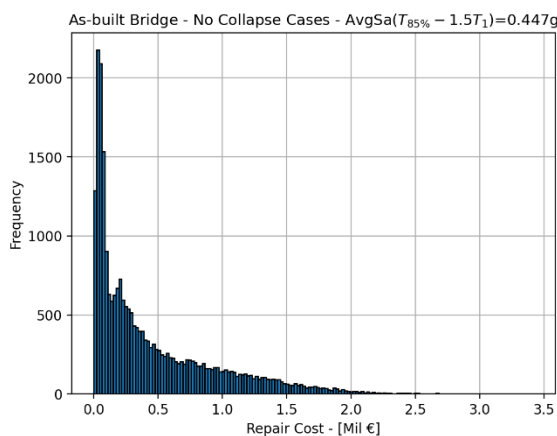
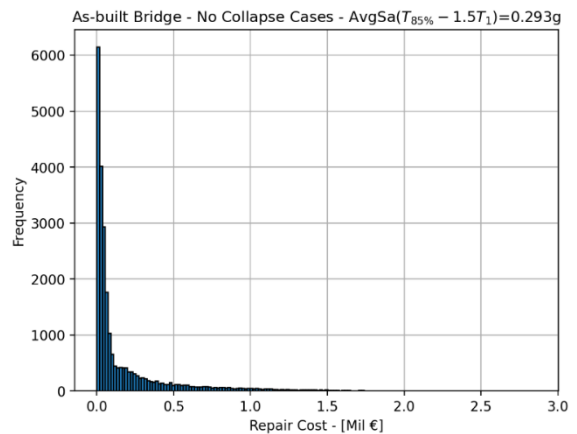
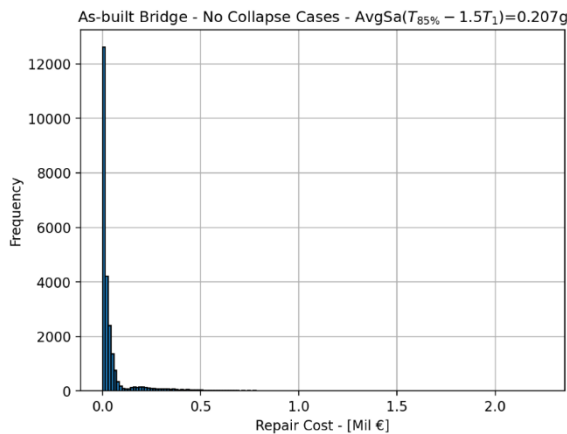


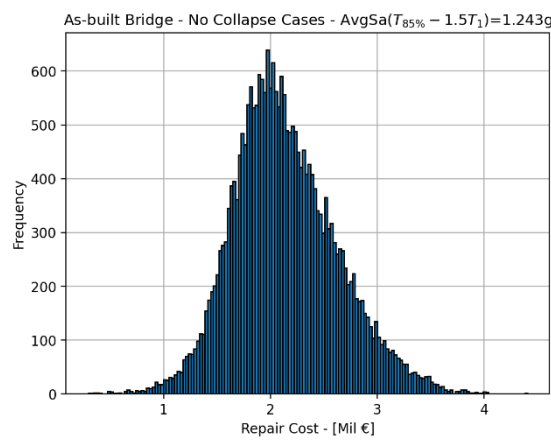
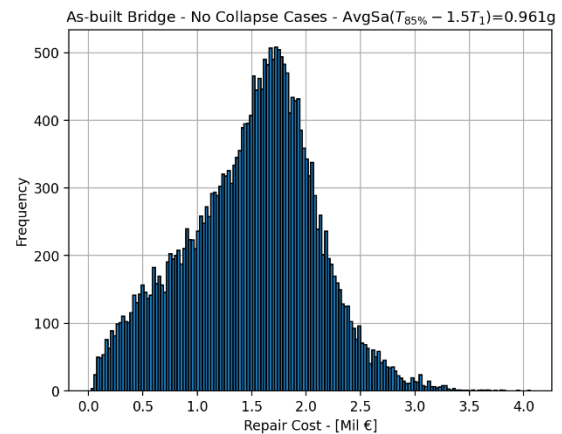
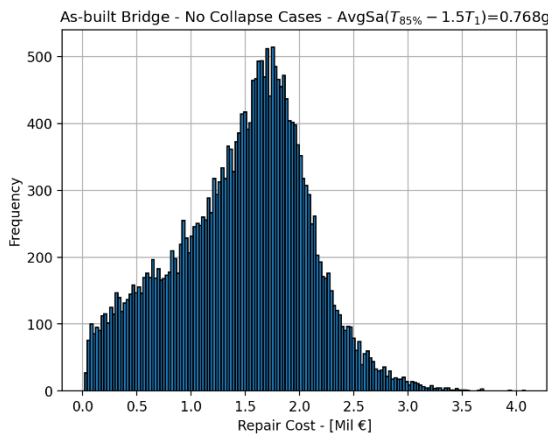


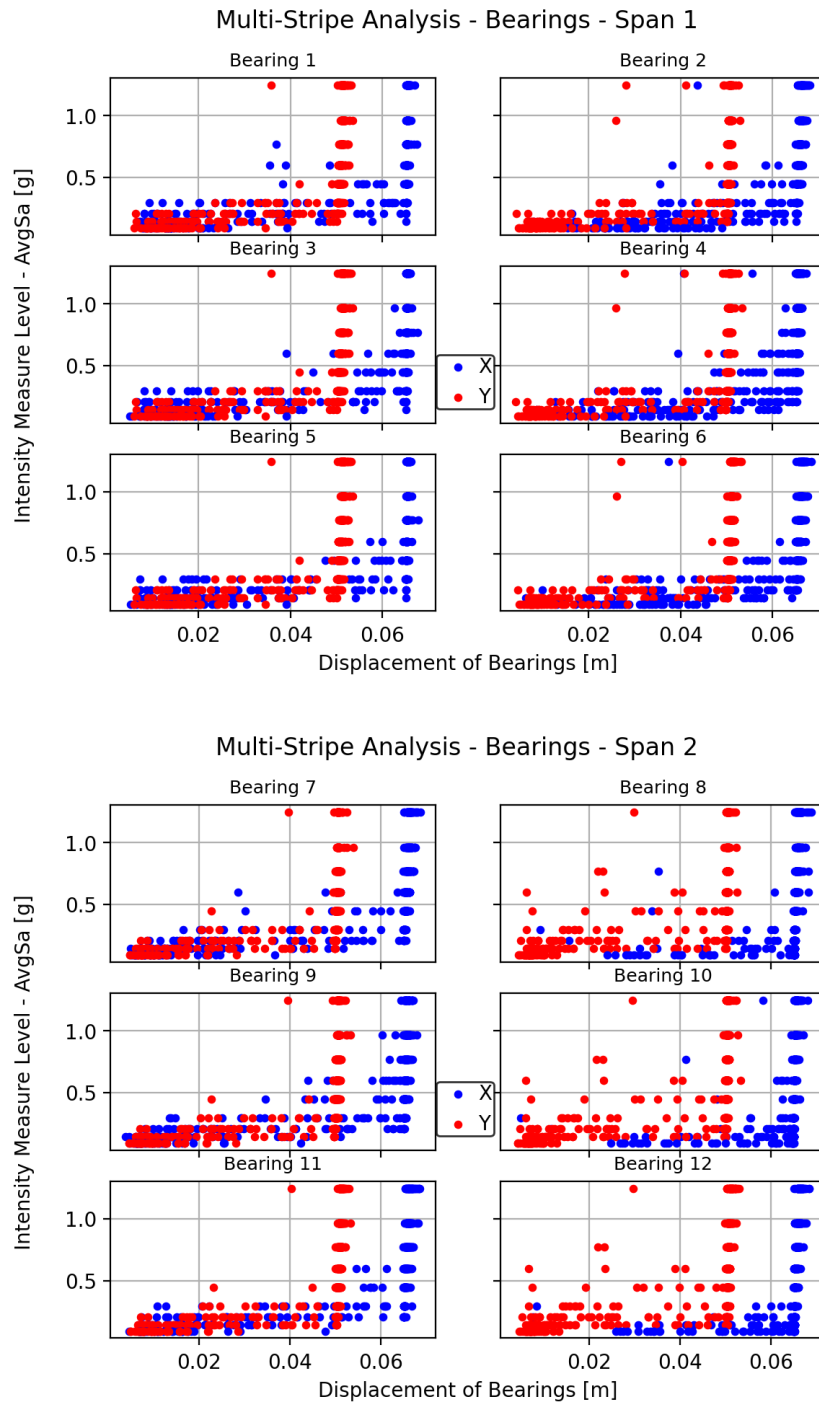


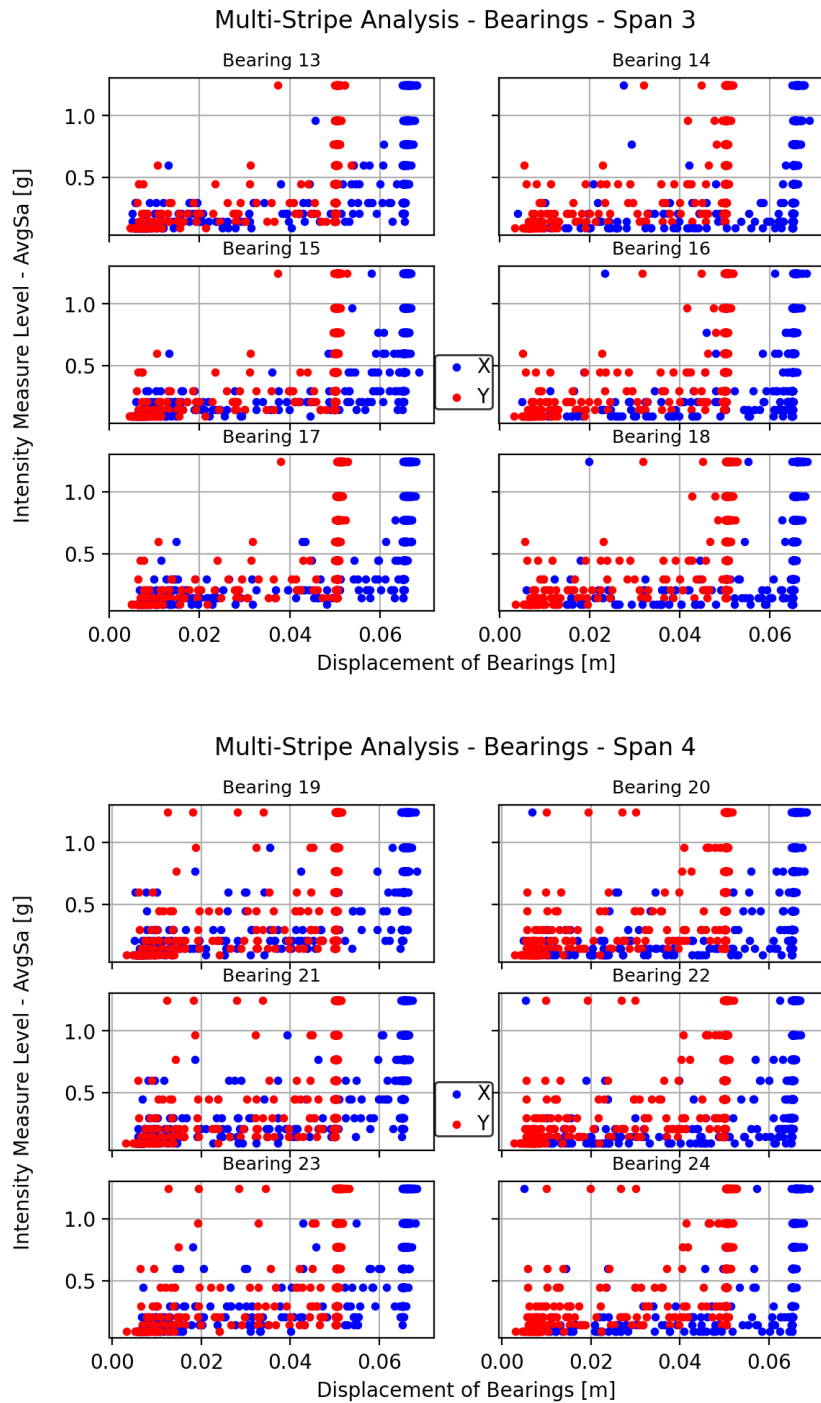


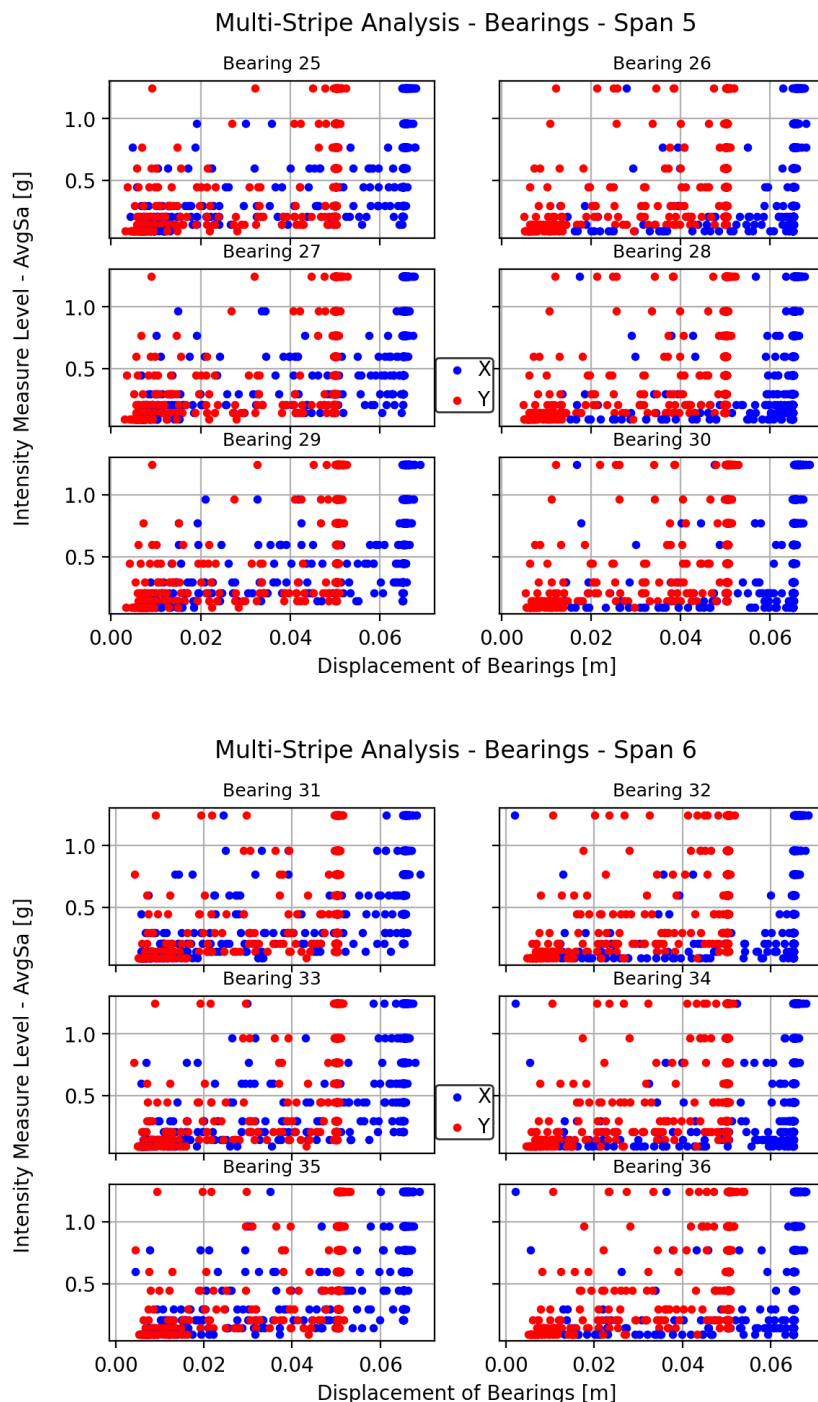


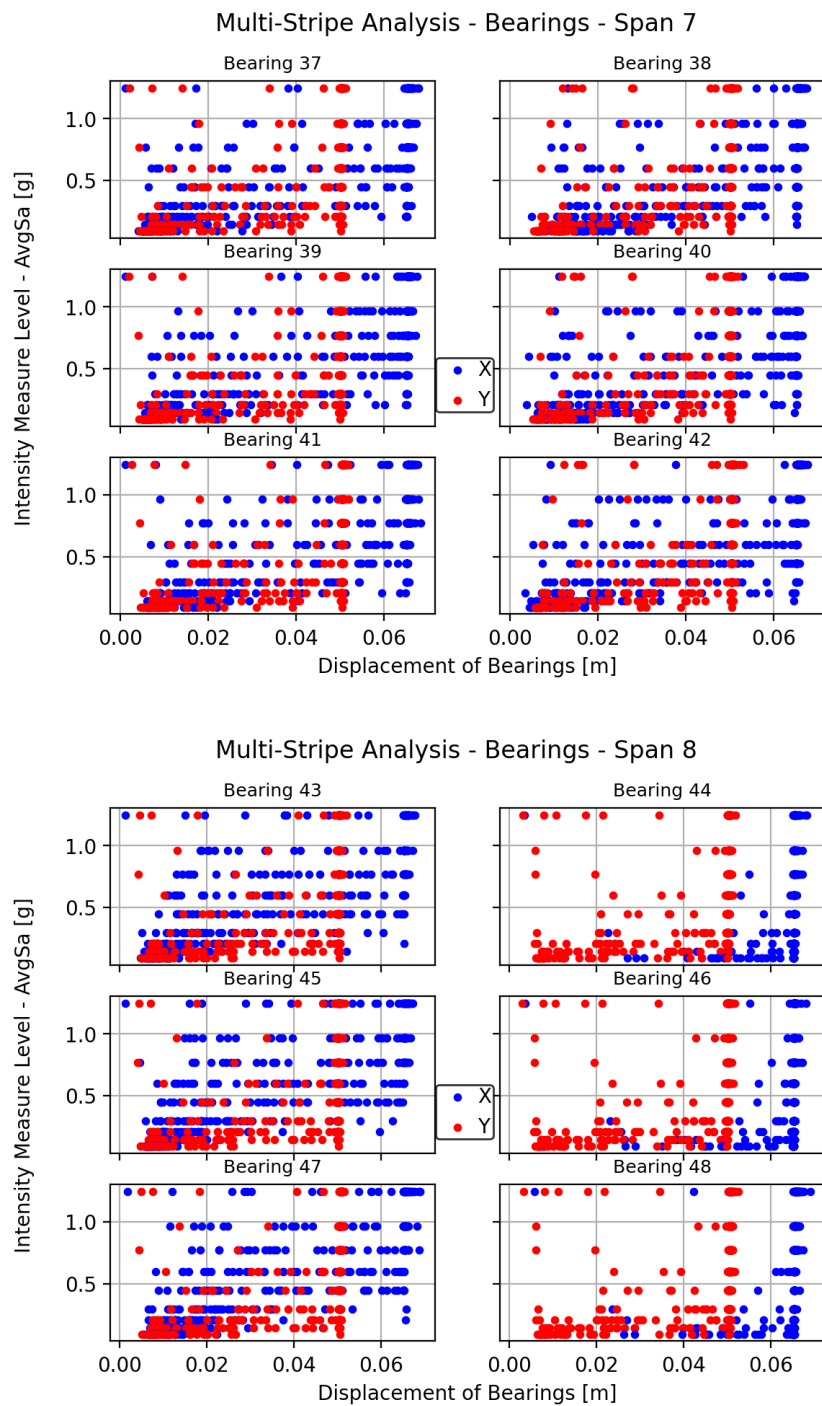


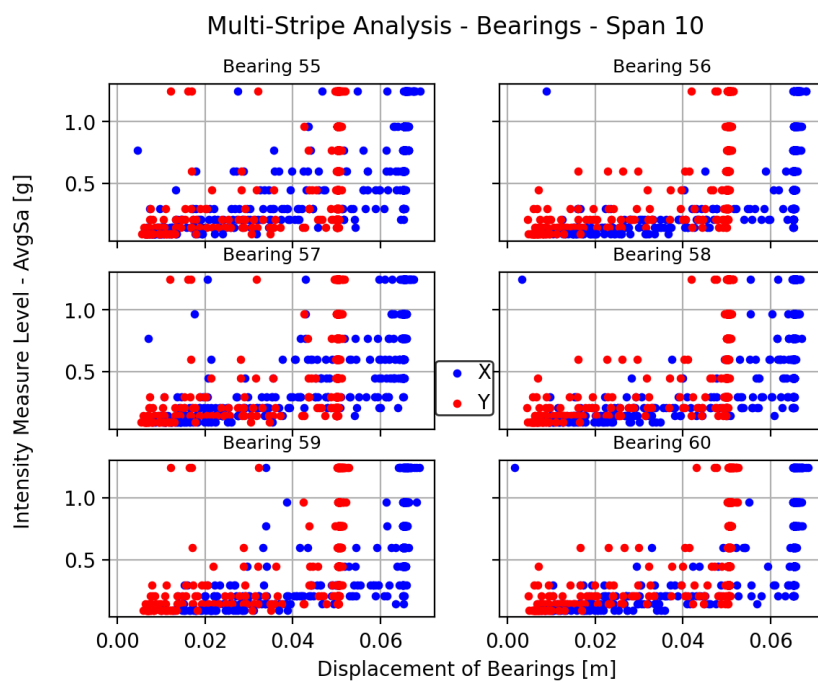
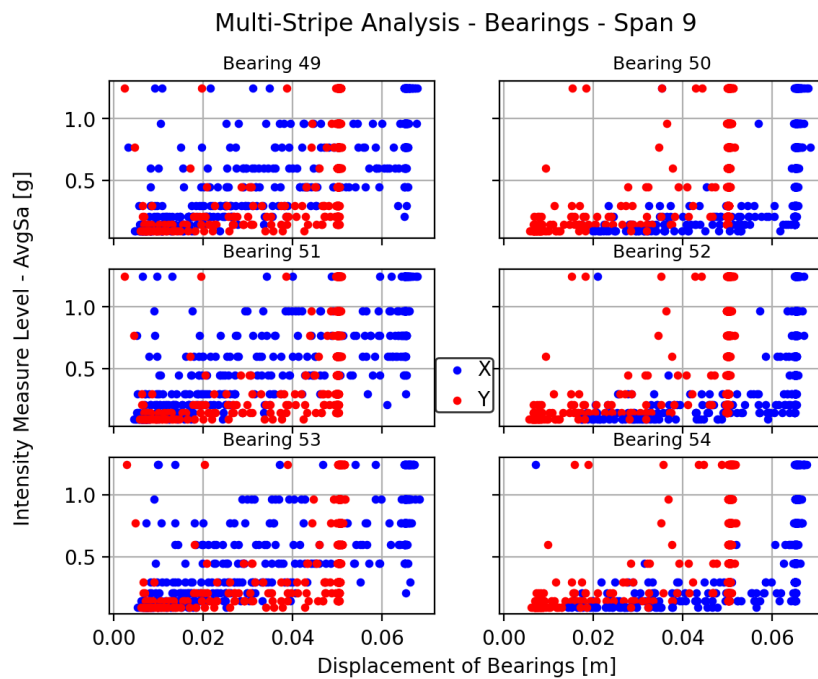


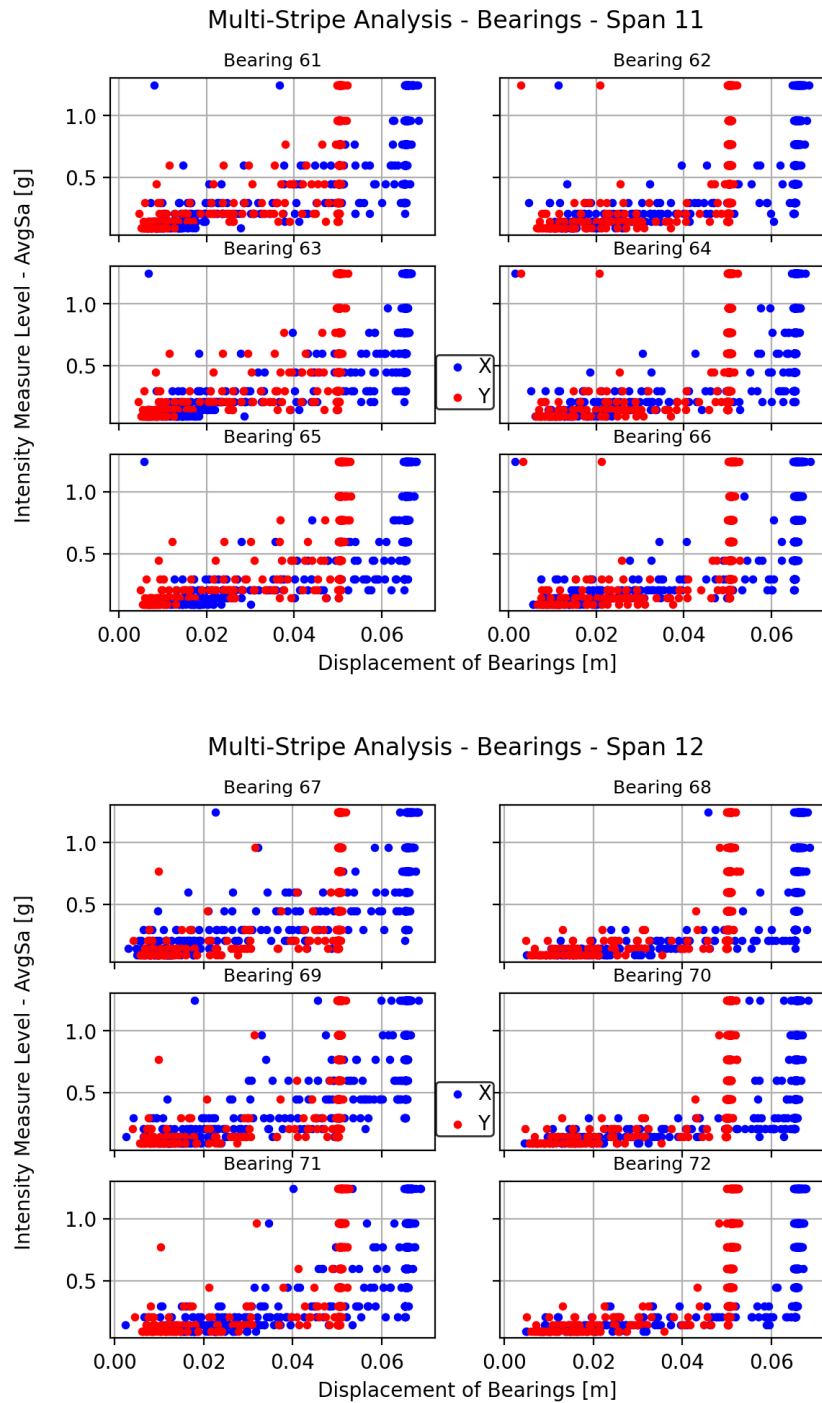


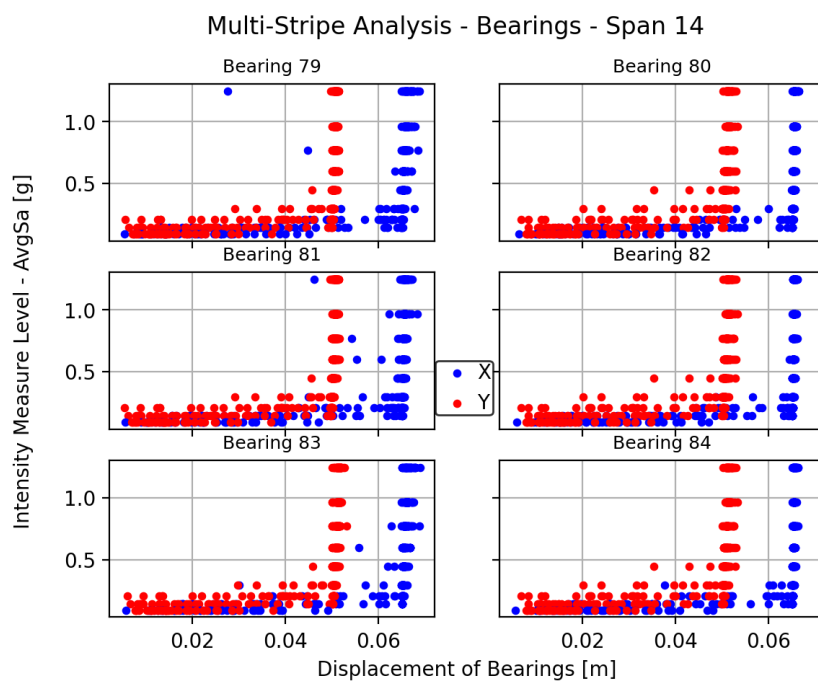
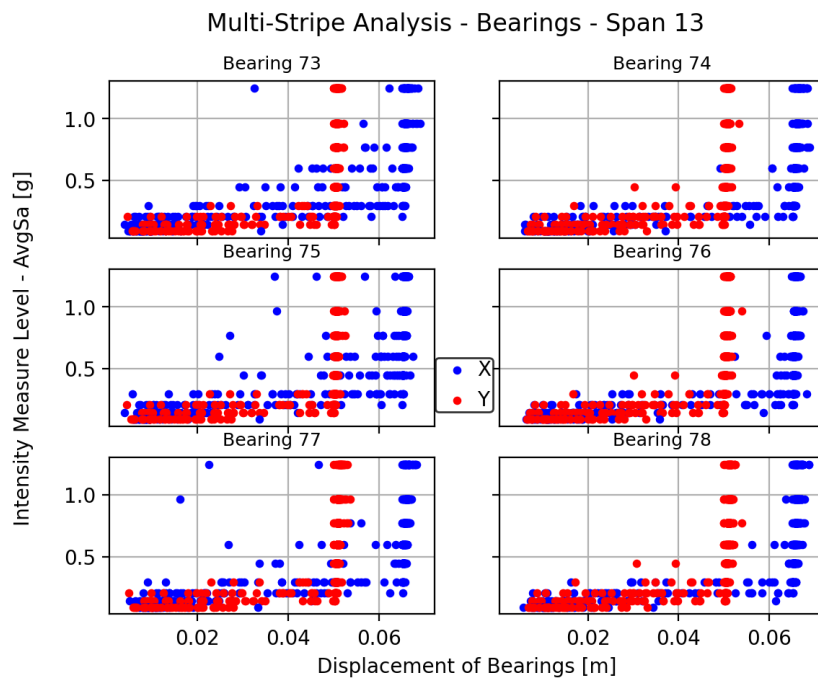


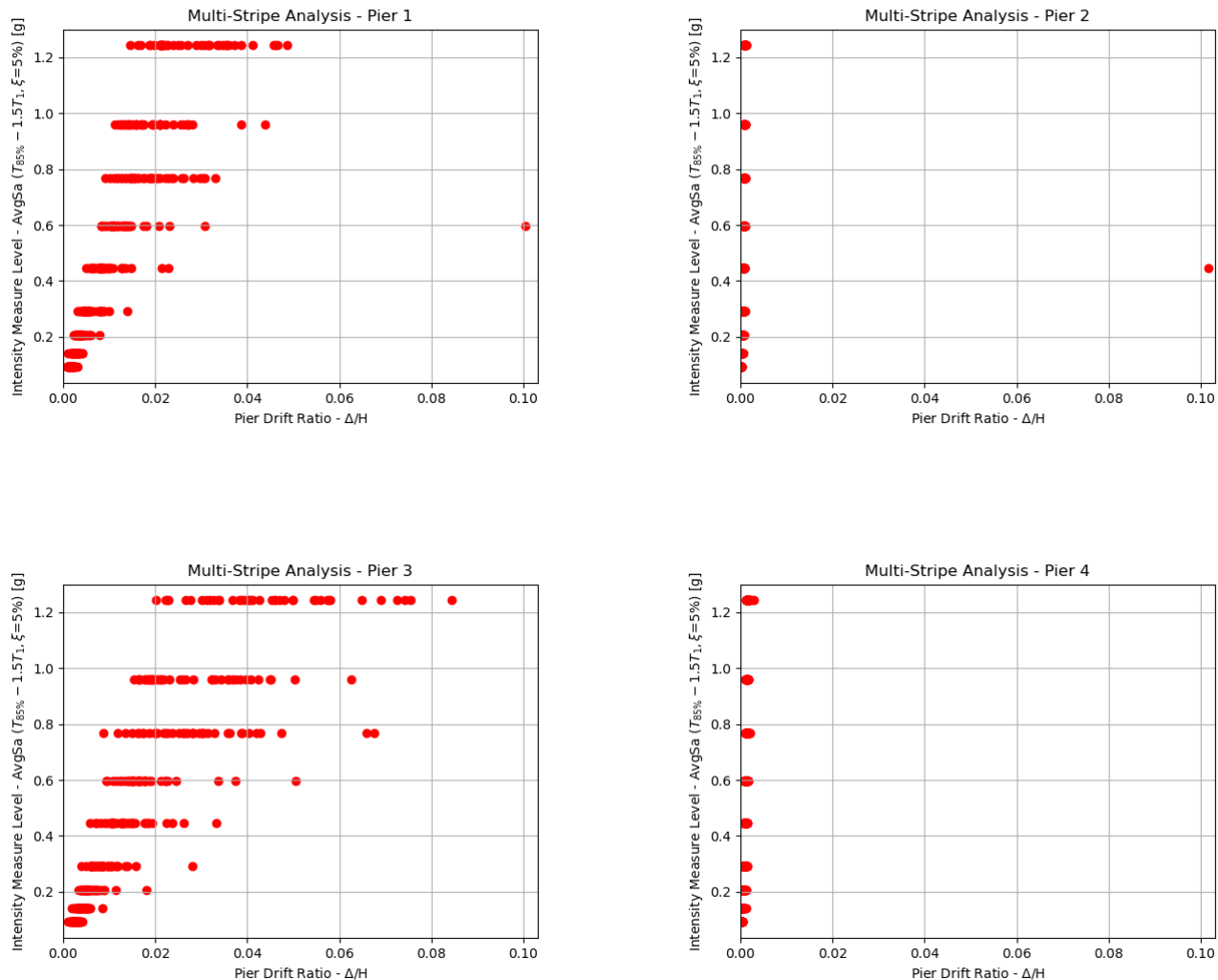


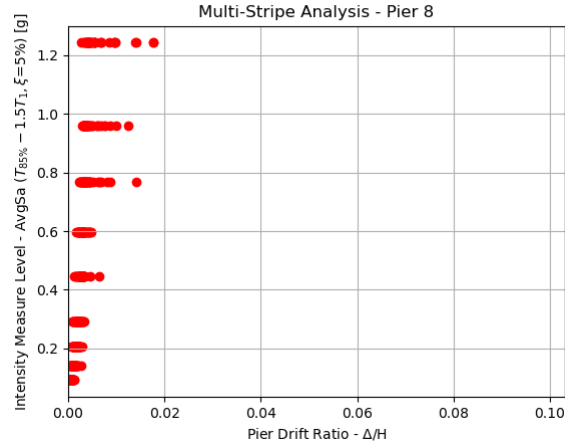
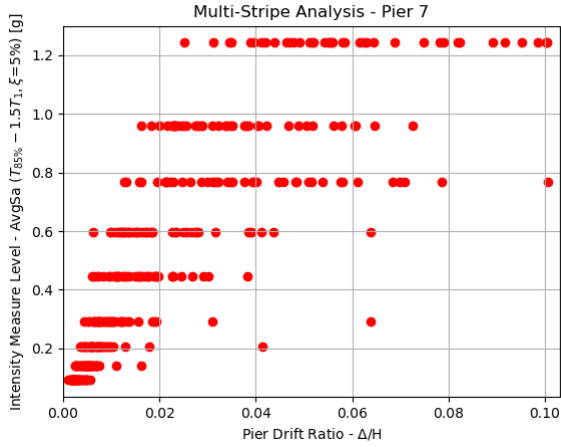
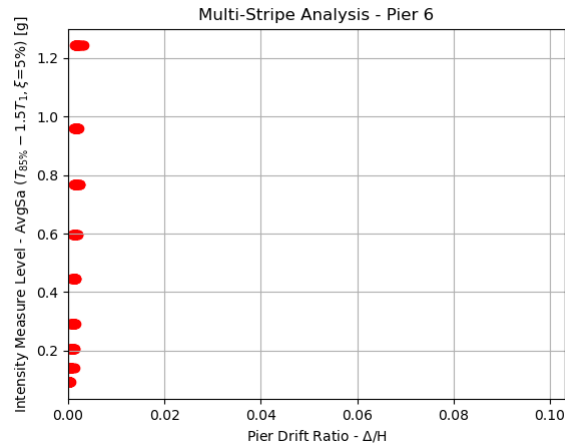
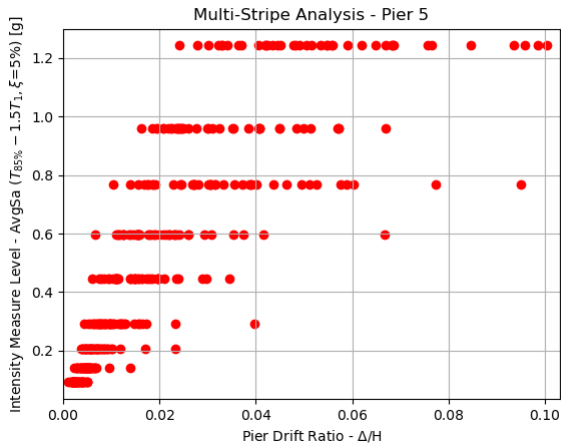


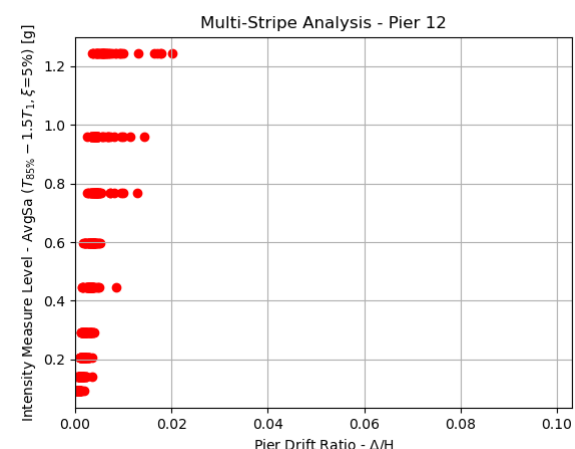
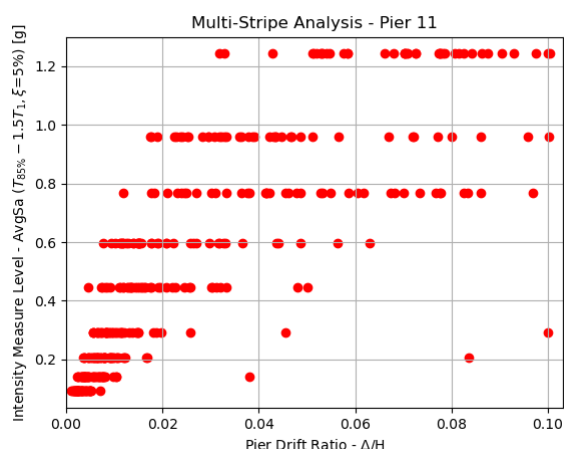
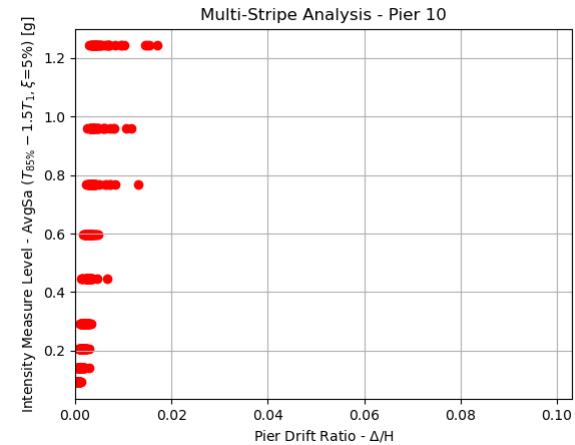
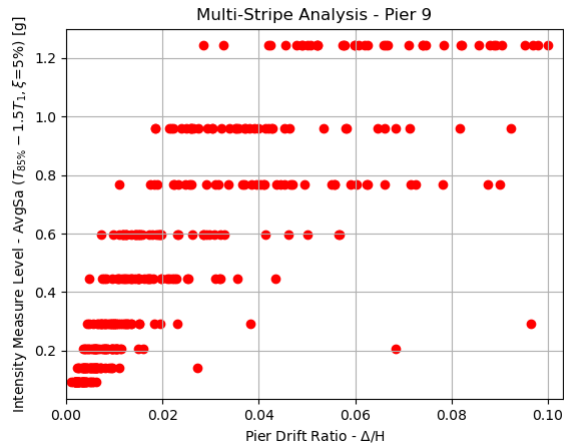


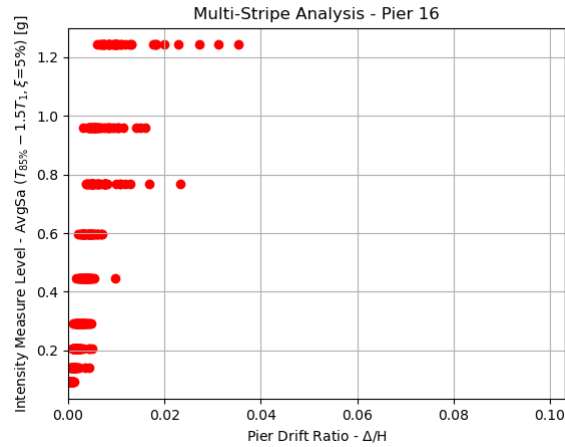
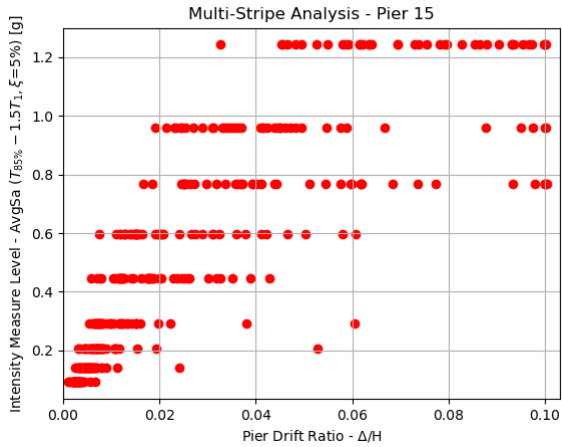
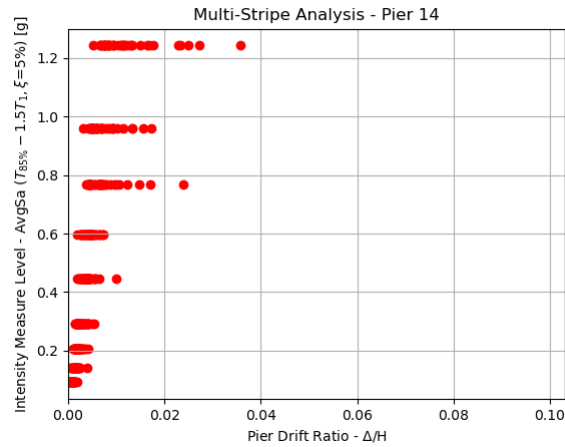
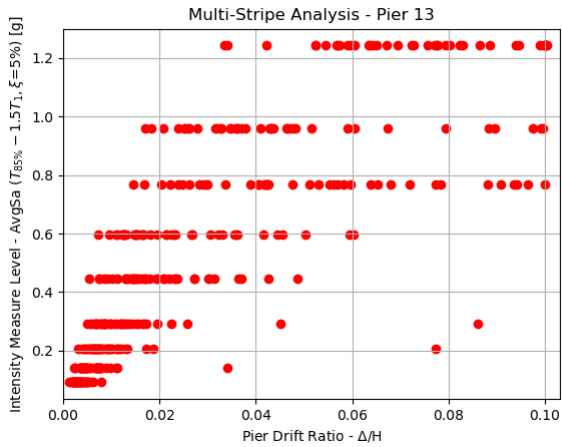


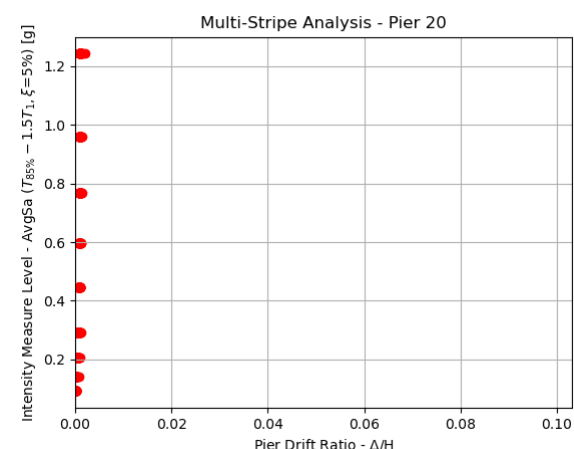
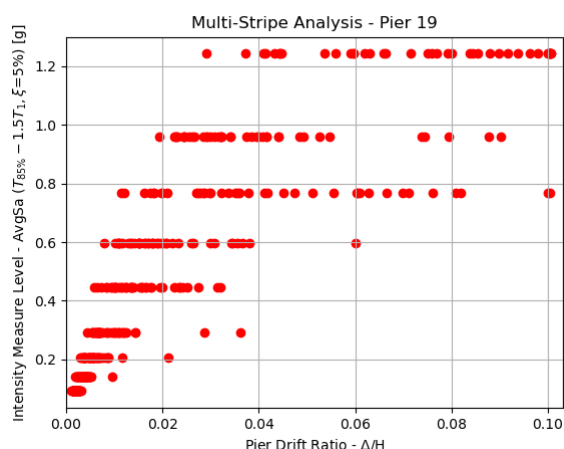
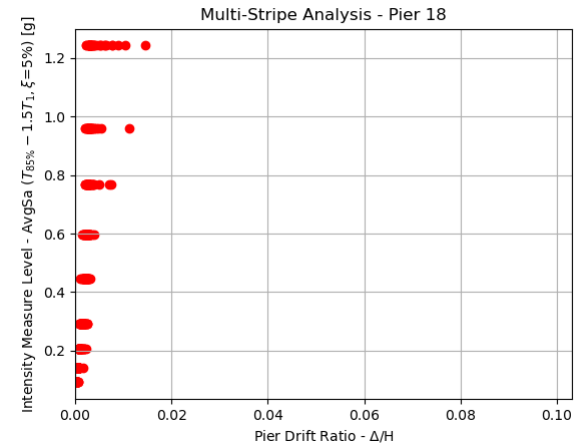
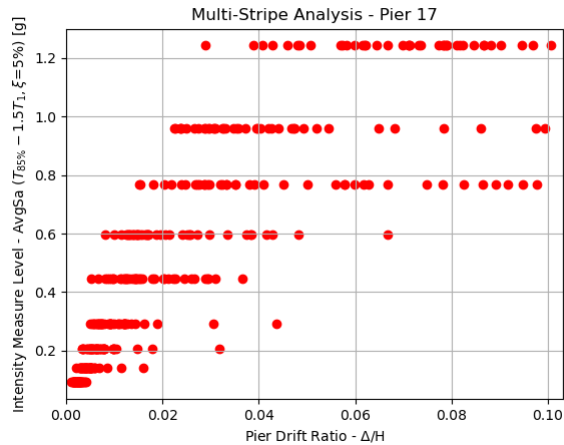


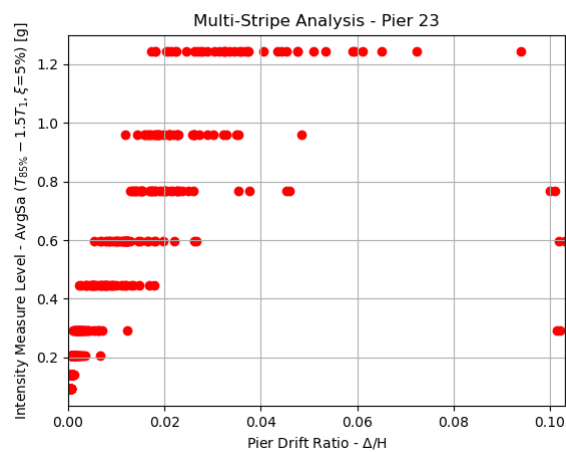
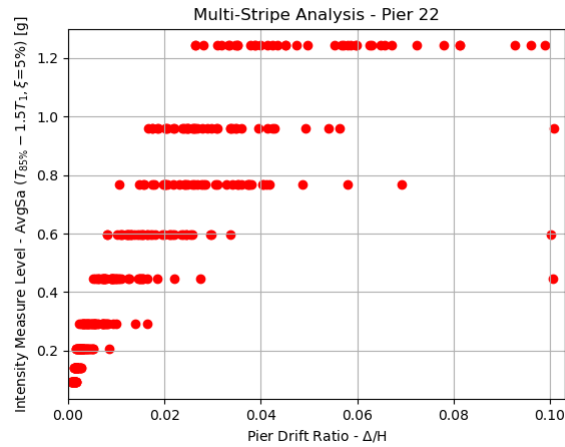
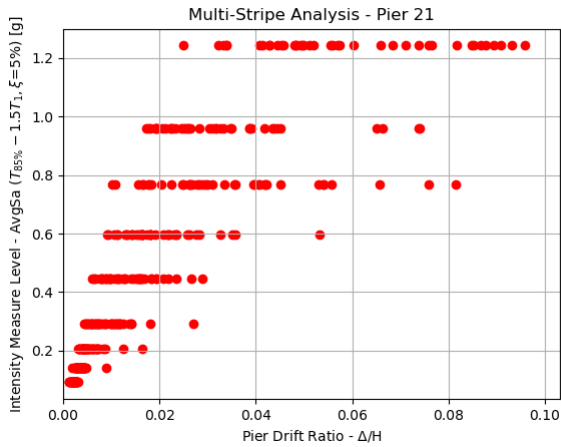












APPENDIX C. Direct Loss Assessment and Structural Analysis Results of the Retrofitted Bridge

